

Diploma thesis

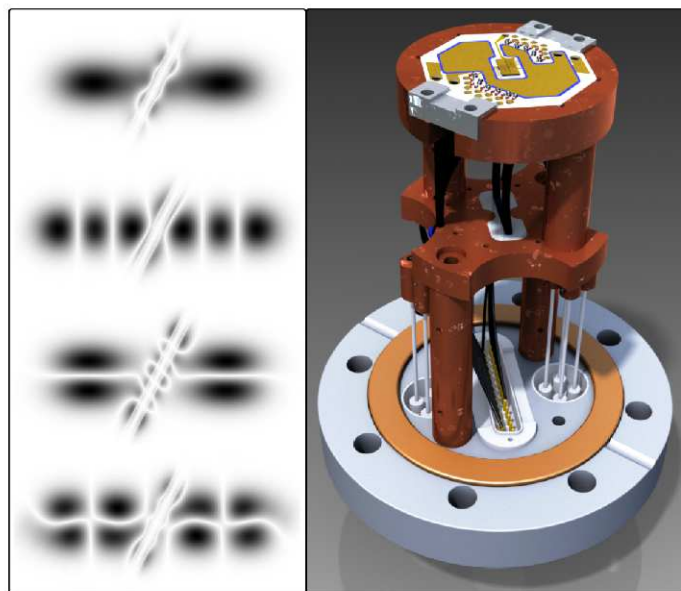
---

# Development and characterisation of a combined atom-ion micro trap

---

Jannis Joger

October 15, 2013



JOHANNES GUTENBERG  
UNIVERSITÄT MAINZ

Erstgutachter: Prof. Dr. Ferdinand Schmidt-Kaler  
Zweitgutachter: Prof. Dr. Patrick Windpassinger

# Abstract

Recent implementations of laboratory ultracold atom-ion systems have opened up a variety of promising research directions. These systems allow for studying atom-ion collisions in the ultracold (quantum) regime, as well as cold chemistry and may find applications in quantum computing. Precisely controlled ions could be used to explore the physics of impurities in (one-dimensional) Bose-Einstein condensates or to perform in situ measurements of ultracold atomic quantum gases. Hybrid atom-ion systems may also be applicable for sympathetic ground state cooling of trapped ions with ultracold atoms or vice versa.

Since the long range atom-ion interaction is much stronger than typical atom-atom interactions, single trapped ions may be used to control the dynamics of atomic systems. In this thesis - as an example of such a system - an atomic Josephson junction that is controlled by a single ion is investigated theoretically. By placing an ion between an atomic double well system the tunnelling rate can be controlled by the spin of the ion. Here, also many-body phenomena such as self-trapping may be observed.

This thesis I shows a result obtained in a previous work revealing that in theory the tunnelling rate can not only be controlled by the spin of the ion but also by its motion. In analysing this problem, I supply a more realistic model that can be tested in future experiments. In particular I investigated the effects of imperfect ion cooling on the tunnelling dynamics.

I built an experimental setup that is developed around a specially designed atom-ion *micro* trap combining the technologies of planar ion traps and atom chips. This hybrid trap, which is meant to trap  $^{87}\text{Rb}$  atoms and  $^{171}\text{Yb}^+$  ions, is part of an octagonal chip, coated with multiple conductive layers featuring the magnetic U and Z shape trap for atoms and the surface electrodes for a planar linear trap for ions. It has an outside diameter of 45 mm and a total height of 1 mm. With this design we expect trapping frequencies of  $\nu > 1.0\text{ kHz}$  for the atoms and frequencies over 1 MHz for the linear ion crystal. Compared to common hybrid traps my trap design is an obvious infrastructural simplification and it provides increased trapping stability. For realising atomic Josephson junctions this setup will enable us to form double well potentials by radio frequency induced adiabatic dressing. Due to the small size of the trap design we realise tight confinement of the ions and atoms. This will allow us to form wave packets of the size of the atom-ion interaction range and to reach the one-dimensional regime. With this setup we will also be able to study many-body phenomena like ion-perturbed quantum gases and ion-enabled entanglement.

To perform these experiments several frequency stabilized lasers are required. As part of this thesis a master-slave laser setup is constructed. The low-power master laser ( $\lambda = 780\text{ nm}$ ,  $P_{\text{max}} = 90\text{ mW}$ ) is a self-built grating stabilized diode laser that is locked

---

to an atomic transition via frequency modulation spectroscopy in a Rubidium vapour cell. I achieved major improvement in output power by realizing master-slave injection locking of a free running high-power slave laser ( $\lambda = 780$  nm,  $P_{\max} = 300$  mW) to the stabilized frequency of the master laser.

The key goals for the near future is an implementation of this experiment by completing and assembling the setup and a realization of  $^{87}\text{Rb}$  Bose-Einstein condensation as well as ground state cooling of trapped  $^{171}\text{Yb}^+$  ions. A future development will be the optimization of the trap design by reducing the number of layers.

# Zusammenfassung

In jüngster Zeit hat die erfolgreiche Realisierung von ultrakalten Atom-Ionen Systemen einige vielversprechende Forschungsrichtungen eröffnet. Die Systeme erlauben das Erforschen von Atom-Ionen Kollisionen im Quantenregime und möglicherweise werden sie auch Anwendung in der Quanteninformationstechnologie finden. Präzise kontrollierte Ionen könnten dazu benutzt werden, das Verhalten von Ionen als Verunreinigungen in (eindimensionalen) Bose-Einstein Kondensaten zu erforschen oder lokale Messungen in ultrakalten atomaren Quantengasen durchzuführen. Hybride Atom-Ionen Systeme könnten außerdem für sympathetisches Grundzustandskühlen von gefangenen Ionen und ultrakalten Atomen mit der jeweils anderen Spezies genutzt werden.

Da die langreichweitige Atom-Ionen Wechselwirkung viel stärker ist als typische Atom-Atom Wechselwirkungen, könnten gefangene Ionen dazu benutzt werden, das Verhalten von atomaren Systemen zu steuern. Als Beispiel wird in der vorliegenden Arbeit ein atomarer Josephson-Kontakt, welcher durch ein einziges Ion gesteuert wird, theoretisch erforscht. Platziert man ein Ion zwischen eine atomare Doppelmulde, kann die Tunnelrate durch den Spin des Ions kontrolliert werden. Hier sind möglicherweise auch Vielkörper-Phänomene wie zum Beispiel das *self-trapping* zu beobachten.

In dieser Arbeit zeige ich theoretisch, dass die Tunnelrate nicht nur durch den Spin des Ions sondern auch durch dessen Bewegung kontrolliert werden kann. Bei der Analyse dieses Problems baue ich auf vorherigen Arbeiten auf und entwickle daraus ein realistischeres Model, welches in zukünftigen Experimenten überprüft werden kann. Insbesondere werden die Auswirkungen auf die Tunneldynamik bei unvollkommener Ionenkühlung untersucht.

Darüber hinaus habe ich einen Versuch rund um eine speziell entwickelte Atom-Ionen Mikrofalle entworfen und deren Aufbau begonnen. Diese Falle, die zum gemeinsamen Fangen von  $^{87}\text{Rb}$  Atomen und  $^{171}\text{Yb}^+$  Ionen konzipiert ist, kombiniert die Technologien von planaren Ionenfallen und Atomchips. Sie ist Teil eines oktogonalen Chips mit einem Außendurchmesser von 45 mm und einer Gesamthöhe von 1 mm, der mit mehreren Leiterebenen beschichtet ist. Diese Leiter sind zum einen U und Z geformt für die magnetische Atomfalle und zum anderen gibt es Oberflächen-Elektroden für eine planare lineare Ionenfalle. Mit diesem Design erwarten wir Fallenfrequenzen von  $\nu > 1.0\text{ kHz}$  für die Atome und Frequenzen von über 1 MHz für den linearen Ionenkristall. Verglichen mit üblichen Hybridfallen ist dieses Design baulich grundlegend vereinfacht und erhöht die Stabilität der Falle. Zur Realisierung von Josephson Kontakten ermöglicht dieser Aufbau die Erzeugung von Doppelmulden-Potentialen durch Radio-Frequenz induziertes adiabatisches *dressing*. Auf Grund der kleinen geometrischen Abmessungen der Falle sind die Atome und Ionen stark lokalisiert. So wird das Erzeugen von eindimensionalen Bose-Einstein Kondensaten sowie von Wellenpaketen im Größenbereich der

---

Atom-Ionen Wechselwirkung ermöglicht. Außerdem werden wir mit diesem Aufbau im Stande sein, Vielkörper-Phänomene wie Quantengase mit Fremdionen oder Ionen-induzierte Verschränkung zu erforschen.

Diese Experimente benötigen einige Frequenz-stabilisierte Laser. Als Teil dieser Arbeit habe ich einen Master-Slave Laser konstruiert. Bei dem schwachen Master-Laser ( $\lambda = 780 \text{ nm}$ ,  $P_{\text{max}} = 90 \text{ mW}$ ) handelt es sich um einen selbstgebauten Gitter-stabilisierten Diodenlaser, der mittels Frequenzmodulations-Spektroskopie in einer Rubidium-Gaszelle auf einen atomaren Übergang stabilisiert wird. Durch die Realisierung von Master-Slave (injection locking) eines freilaufenden Slave-Lasers ( $\lambda = 780 \text{ nm}$ ,  $P_{\text{max}} = 300 \text{ mW}$ ) konnte die Ausgangsleistung des Lasers bedeutend verbessert werden.

Hauptziele für die nahe Zukunft sind die Fertigstellung und die endgültige Inbetriebnahme des Experiments, das Erzeugen von  $^{87}\text{Rb}$  Bose-Einstein Kondensaten sowie das Grundzustandskühlen von  $^{171}\text{Yb}^+$  Ionen. Daraufhin wird das Falldesign optimiert.

# Contents

<b>1. Introduction</b>	<b>1</b>
<b>2. Dynamics of an ion-controlled Josephson junction</b>	<b>3</b>
2.1. Atom-ion interaction . . . . .	4
2.2. Double well with fixed ion . . . . .	5
2.3. Double well with moving ion . . . . .	11
2.4. The effect of imperfect ion cooling on tunnelling . . . . .	14
<b>3. Trap design</b>	<b>19</b>
3.1. General considerations . . . . .	19
3.2. The atom-ion micro trap . . . . .	19
3.3. The ion micro trap . . . . .	20
3.4. The atom micro trap . . . . .	24
3.5. Coil design . . . . .	45
3.6. Vacuum Setup . . . . .	48
<b>4. Laser system</b>	<b>51</b>
4.1. Overview . . . . .	51
4.2. Master-Slave laser setup . . . . .	57
4.3. Homebuilt lasers . . . . .	64
<b>5. Outlook</b>	<b>71</b>
<b>A. Appendices</b>	<b>73</b>
A.1. Parameters, coordinates and operators used in the calculations . . . . .	73
A.2. Values of $E^*$ and $R^*$ for various combinations of atoms and ions . . . . .	75
A.3. Construction manual for assembling the coils . . . . .	77
A.4. Assembling the trap . . . . .	80
A.5. Atomic level schemes . . . . .	81
A.6. Electronic schemes and technical drawings . . . . .	84
A.7. Tables and measurements . . . . .	98



# 1

## Introduction

Recently, hybrid systems combining ultracold quantum gases and trapped ions have been explored theoretically and experimentally [1–7]. The focal points of the exploration of such systems are in understanding atom-ion collisions in the ultracold (quantum) regime [8–19], cold chemistry [20, 21] and the effects on quantum gases due to a small number of ionic impurities [22–25]. On the one hand these experiments aim at studying many-body systems [26] and on the other hand they are promising for applications such as in sympathetic cooling of trapped ions with ultracold atoms (or vice versa) and quantum computing [27–31].

The trapping of both, ions and atoms, is realized with electromagnetic fields. For example, single ions as well as ion crystals - consisting of an arrangement of ions - are spatially confined in Paul traps. These traps employ oscillating electric fields for confining ions. A prominent example of the Paul trap is the linear Paul trap consisting of four bar-shaped electrodes while a radio frequency (RF) voltage is applied to two opposing electrodes (fig. 1.1 a)). In this case the oscillating RF quadrupole field confines the ions in the radial direction and a static electric potential in the axial direction [32]. Neutral atoms can be trapped in optical traps, magnetic traps or in magneto-optical traps (MOTs) [33].

To date experiments on combined atom-ion systems typically employ conventional traps such as mm size linear Paul traps for the ions and magnetic/optical traps for the atoms [3, 7, 21]. In contrast, within the scope of this thesis, a hybrid *micro* trap is developed combining planar ion traps [34–38] and atom chip technology [39, 40, 40–43]. Such planar ion traps (fig. 1.1 b)) consist of few electrodes on the surface of a chip which forms a similar electric quadrupole trapping field as a linear Paul trap. On atom chips, micro fabricated electromagnets are used to trap atoms magnetically. Combining these techniques does not only represent a considerable infrastructural simplification in comparison to conventional traps, it also enables increased scalability since this setup allows to integrate many traps on one chip. As the ions and the atoms are held by the same structure, the positioning of them with respect to each other should be affected much less by temporal drifts and could be performed with an accuracy at the scale of the quantum wave packet size. Atomic micro traps are also advantageous for studying one-dimensional quantum gases [44–47] and double-well systems [48–50]. Combining such systems with trapped ions should enable us to study new many-body phenomena

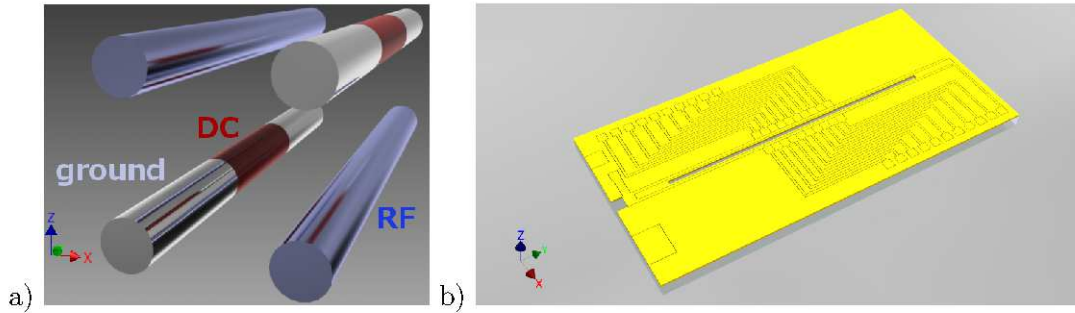


**Figure 1.1.:** Design of a linear Paul trap and of a planar ion trap.

such as in ion-perturbed quantum gases [23] and ion-enabled entanglement [51]. Since planar traps form very steep trapping potentials they can provide tighter confinement of the ions and the atoms than conventional traps. This will give us the possibility to perform exact measurements with wave packet resolution of the atom-ion interactions.

Presently, the experimental setup is still in the construction phase. We have bought all parts belonging to our setup and there were several special constructions built in our workshop. Still missing is one part of the trap which is to be completed by the time I submit this thesis. This is because in our design we make use of novel building techniques which should enable us to realize exceptionally tight atomic trapping. Unfortunately, these techniques require individually tested components. We expect assembly of the parts to proceed in the coming months.

This thesis is structured as follows: In chapter 2 an ion controlled bosonic Josephson junction is investigated theoretically as an extension of previous work published in [51]. Here the spin or motion of the ion controls the tunnelling rate of atoms between the two wells of a double well potential. In chapter 3 the design, fabrication and assembly of the experimental setup is presented and it also provides a short description of the relevant theoretical background focusing on the trapping of ions and atoms. This chapter gives a detailed description of the considerations leading to the final design of the atom-ion trap, the high-power magnetic field coils and the vacuum setup. Another important part of this thesis deals with the development and the setting-up of a complete laser system as described in chapter 4.

# 2

## Dynamics of an ion-controlled Josephson junction

One of the quantum effects we want to observe in our experiment is quantum tunnelling in a Josephson junction. The original Josephson junction consists of two superconductors separated by a thin insulator. In the a.c. Josephson effect a constant voltage is applied between both superconductors which causes the Cooper pairs - which can be seen as Bosons - to tunnel through the insulator. Here one can measure an oscillating current flow. In the d.c. Josephson effect a constant current is applied causing a constant supercurrent flowing through the insulator [52].

Atomic Josephson junctions are a very active field of research, both theoretically and experimentally [53–60]. Following [61] a Josephson junction may be realized with ultracold atoms in a double well potential. This potential is precisely controllable and provides two separated minima representing atomic traps for Bose-Einstein condensates (BEC). If a BEC is initially localized in one of these wells it can oscillate between them by quantum tunnelling. This effect can also lead to interesting quantum many-body phenomena such as self-trapping [62] and entanglement when atomic interactions are present [63].

Here, we study a new type of Josephson junction where a single ion will be used to control the tunnelling of ultracold atoms. Two BECs are trapped in a double well potential and there is a single ion trapped between them that has an internal spin state that can be tuned with laser light or radio frequency fields (fig. 2.1). As described below, the potential between the atoms and the ion is attractive at long range but strongly repulsive at short range. It also depends on the spin orientation ( $|\uparrow\rangle, |\downarrow\rangle$ ) of the ion [17] such that it should be possible to control the tunnelling rate  $\hat{J}$  by tuning the internal state of the ion. The considered setup may allow for better experimental control than proposals aiming at studying Josephson physics controlled by single trapped atomic impurities [64, 65].

In [51] the dynamics of this ion-controlled atomic Josephson junction have been studied theoretically under the simplification that the ion is static. In this chapter I improve on this simplified model by investigating how taking the motion of the ion into account influences the dynamics. Since the Hilbert space dimension of the problem increases

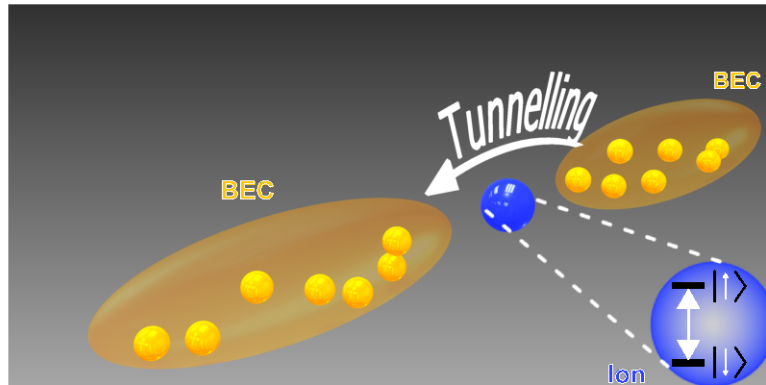


**Figure 2.1.:** Double well Josephson junction [51]. The internal state of the ion controls the tunnelling rate  $\hat{J}$  between the two BEC clouds.

significantly in this case I limit the calculation to one dimension (in contrast to [51]). In section 2.1 I describe the atom ion interaction within quantum defect theory. Then, in section 2.2, I first revisit the calculation done in [51], i.e. assuming a static ion but now in one dimension. This allows a clear insight into the methods employed for tackling the full problem in section 2.3. Here the calculation shows that the tunnelling may also be controlled by the motional state of the ion. In section 2.4 I use a simplified model to study the effect of imperfect ion cooling on the tunnelling dynamics. It is found that for low average vibrational quantum numbers of the ion, the tunnelling is not affected significantly on short time scales. The next step will be to include the micro motion of the ion in the trap. This is not part of this thesis but the complete theory will be published in a subsequent paper.

## 2.1. Atom-ion interaction

The electric field of the ion induces an atomic dipole which attracts the ion. This can be described by an effective long range potential which at large distances is given by [10]:

$$\lim_{r \rightarrow \infty} V_{ia}(r) = -\frac{C_4}{r^4}, \quad (2.1)$$

where  $C_4 = e^2 \alpha_p / 2$  is a constant that depends on the static polarizability of the atom  $\alpha_p$  and the charge of the ion  $e$ . For  $r \rightarrow 0$  eq. 2.1 does not hold anymore since terms of higher order, like the exchange forces, start to dominate the interaction which becomes strongly repulsive. In this regime the exact form of the potential is not known well enough to solve the problem and - even more - does not need to be known for our problem. A nice approach to characterize the long range part of the interaction is given by quantum defect theory which can be used to parametrize the dynamics without knowing the exact form of the short-range interaction. In quantum defect

theory all short-range effects are included in one parameter, the short-range phase  $\phi$ . This parameter is related to the atom-ion s-wave scattering length  $a_s = -R^* \cot(\phi)$  in the ultracold regime [10, 16, 51].

In order to characterise the atom-ion potential it is useful to define the length scale  $R^* = \sqrt{2\mu C_4/\hbar^2}$  and the energy scale  $E^* = \hbar^2/(2\mu(R^*)^2)$ , where  $\mu = m_i \cdot m_a/(m_i + m_a)$  is the reduced mass. A table of characteristic lengths and energies for several atom-ion pairs and also a table of parameters and coordinates used in this chapter can be found in appendix A.1. Throughout the chapter we make the secular approximation in which the time dependence of the Paul trap is replaced by a time independent potential, such that the ion is assumed to have no micro motion.

## 2.2. Double well with fixed ion

In this section we illustrate the solution to the ion-controlled double well problem under the assumption that the ion is static and positioned right between the two wells at  $r_i = 0$ . This assumption is motivated by the observation that ions are generally trapped much tighter than atoms in experiments. The assumption also simplifies the calculation allowing us to demonstrate the basic principle of such a problem. In the next sections we show how the picture changes when the ion dynamics are taken into account.

We first consider a system of a single ion and a single atom. The ion is trapped in the electric field of an ion trap (section 3.3) and the atom is trapped in a double-well potential (section 3.4.9). For this setup the atomic Hamiltonian is given by:

$$H_a = \frac{p_a^2}{2m_a} + V_{\text{dw}}(r_a) - \frac{C_4}{r_a^4}, \quad (2.2)$$

where  $p_a = -i\hbar \partial/\partial r_a$  is the momentum of the atom,  $m_a$  is the atomic mass and  $V_{\text{dw}}(r_a)$  is the double-well potential. A symmetric double-well potential can be considered as the overlap of two single-well potentials and is often chosen in this context as [61]:

$$V_{\text{dw}}(r_a) = \frac{b}{q^4} (r_a^2 - q^2)^2 \quad (2.3)$$

An arbitrary double-well potential with  $q = b = 2$  is shown in fig. 2.2. This potential has two minima at  $r_a = \pm q$  and  $b$  is the height of the barrier between the two wells at  $r_a = 0$ . For each inter-well distance  $2q$  the local trapping frequencies for this potential  $\omega_a = \sqrt{8b/m_a q^2}$  are fixed by setting  $b = \omega_a^2 m_a q^2/8$ , such that  $q$  can be changed without changing the local trapping frequency. It is also convenient to introduce the dimensionless parameter  $\alpha_a = (R^*/4l_a)^4 = (\hbar\omega_a/2E^*)^2$  which compares the length scale  $R^*$  to the size of the atomic ground state  $l_a = \sqrt{\hbar/2m_a\omega_a}$ .

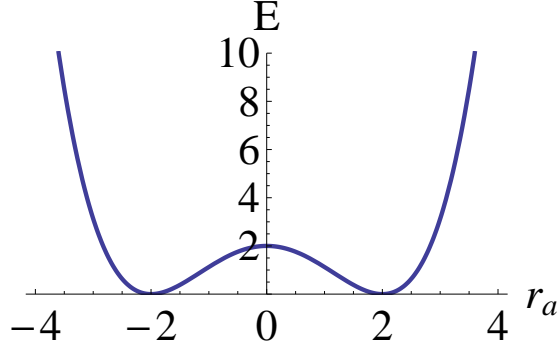


**Figure 2.2.:** Example of a double-well potential with minima at  $r_a = \pm q$  for  $q = 2$  and an inter-well barrier height of  $b = 2$ .

On the basis of these considerations the Hamiltonian is rewritten in units of  $E^*$  and  $R^*$ :

$$H_a = \underbrace{-\frac{\mu}{m_a} \frac{\partial^2}{\partial r_a^2} + \frac{m_a}{\mu} \alpha_a r_a^2 - \frac{1}{r_a^4}}_{H_a^{(0)}} + \underbrace{\alpha_a \frac{m_a}{\mu} \left( \frac{q^2}{4} - \frac{3r_a^2}{2} + \frac{r_a^4}{4q^2} \right)}_{H_a^{(1)}} \quad (2.4)$$

As described above, quantum defect theory is implemented to deal with the term  $-1/r_a^4$

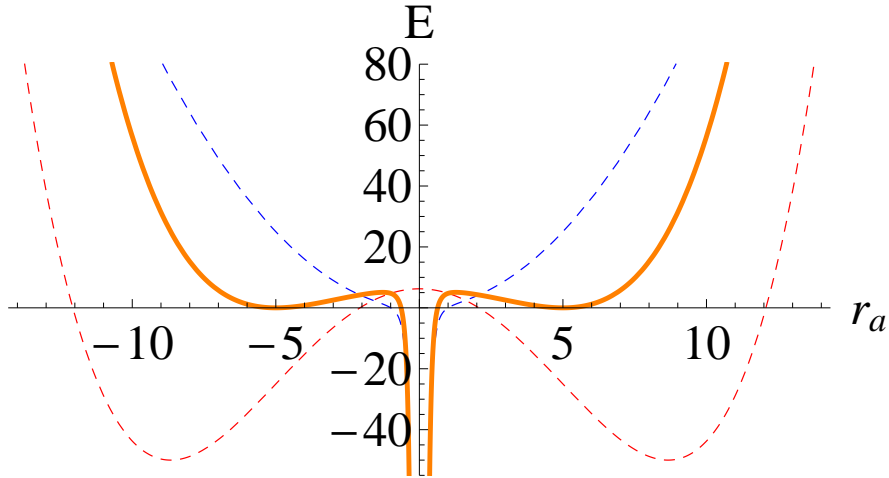


**Figure 2.3.:** Qualitative illustration of the potentials in eq. 2.4 with  $\alpha_a \frac{m_a}{\mu} = 1$  in units of  $E^*$  and  $R^*$ . The blue, dashed line corresponds to  $r_a^2 - 1/r_a^4$  in  $H_a^{(0)}$  and the red, dashed line to the expression in the brackets in  $H_a^{(1)}$  for  $q = 2$ . The thick, orange curve is the sum of both potentials.

in  $H_a^{(0)}$  for  $r_a \rightarrow 0$ . The Schrödinger equation for  $H_a^{(0)}$  is given by:

$$E^{(0)}\psi = H_a^{(0)}\psi \quad (2.5)$$

For  $r_a \rightarrow 0$  we can neglect all potential energy terms but  $-1/r_a^4$ , which leaves us with:

$$0 = \left( -\frac{\mu}{m_a} \frac{\partial^2}{\partial r_a^2} - \frac{1}{r_a^4} \right) \psi \quad (2.6)$$

The solutions of eq. 2.6 include the short-range phase  $\phi$  mentioned above. In the one dimensional case we have to replace  $\phi$  by a pair of phases,  $\phi_e$  and  $\phi_o$ , to allow even and odd solutions,  $\tilde{\psi}_e$  and  $\tilde{\psi}_o$ , which are given by [10]:

$$\tilde{\psi}_e(r_a) = |r_a| \sin \left( \sqrt{\frac{m_a}{\mu}} \frac{1}{|r_a|} + \phi_e \right), \quad (2.7)$$

$$\tilde{\psi}_o(r_a) = r_a \sin \left( \sqrt{\frac{m_a}{\mu}} \frac{1}{|r_a|} + \phi_o \right). \quad (2.8)$$

Solving the Schrödinger equation 2.5 is done with the Numerov method [16, 66], using the wave functions eqs. (2.7, 2.8) as a boundary condition at some point  $r_{min} \gtrsim 0$ . We choose  $r_{min}$  such that  $\frac{1}{r_{min}^4} \gg E_{max}$ , where  $E_{max}$  is the largest energy considered. The short-range phases are not known for any atom-ion combination, so we choose realistic values for our calculations<sup>1</sup>. This method gives the solutions  $\psi_k^{(0)}(r_a)$  with the eigenenergies  $E_k^{(0)}$  with quantum number  $k$ .

Following [11] we expand the solution to the double well problem in the basis of  $\psi_k^{(0)}(r_a)$ :

$$\psi(r_a) = \sum_k c_k \psi_k^{(0)}(r_a) \quad (2.9)$$

The Schrödinger equation of this problem which has to be solved is given by:

$$\sum_k c_k \left( E_k^{(0)} + \frac{\alpha q^2}{4} - \frac{3\alpha r_a^2}{2} + \frac{\alpha r_a^4}{4q^2} \right) \psi_k^{(0)}(r_a) = E \sum_k c_k \psi_k^{(0)}(r_a) \quad (2.10)$$

The next step is to multiply  $(\psi_{k'}^{(0)}(r_a))^*$  from the left and integrate over  $r_a$ :

$$\delta_{k'k} c_{k'} \left( E_k^{(0)} + \frac{\alpha q^2}{4} \right) - \alpha \sum_k c_k \int dr_a (\psi_{k'}^{(0)}(r_a))^* \left( \frac{3r_a^2}{2} - \frac{r_a^4}{4q^2} \right) \psi_k^{(0)}(r_a) = E c_{k'}, \quad (2.11)$$

where  $\delta_{k'k}$  is the Dirac delta function. Eq. 2.11 is a matrix equation which can be written in the form:

$$\sum_k H_{k'k} c_k = E c_{k'} \quad (2.12)$$

In this case, to determine  $H_{k'k}$  we will have to evaluate one quadratic and one quartic matrix element:

$$M_{k,k'}^{(2)} = \int dr_a (\psi_k^{(0)}(r_a))^* r_a^2 \psi_{k'}^{(0)}(r_a) \quad (2.13)$$

<sup>1</sup>We note that these values can be tuned in an experiment by external confinement or with magnetic fields [17].

## 2. Dynamics of an ion-controlled Josephson junction

and

$$M_{k,k'}^{(4)} = \int dr_a (\psi_k^0(r_a))^* r_a^4 \psi_{k'}^0(r_a) \quad (2.14)$$

The Hamiltonian with these matrix elements is therefore given by:

$$H_{kk'} = \left( E_k^{(0)} + \frac{\mu\alpha q^2}{4m_a} \right) \delta_{kk'} - \frac{3\mu\alpha}{2m_a} M_{kk'}^{(2)} + \frac{\mu\alpha}{4m_a q^2} M_{kk'}^{(4)} \quad (2.15)$$

We find the eigenstates and eigenenergies of the double well by diagonalising the Hamiltonian. For these calculations we used *The MathWorks' MATLAB* and for plotting the results we used *Wolfram's Mathematica*.

### 2.2.1. Example

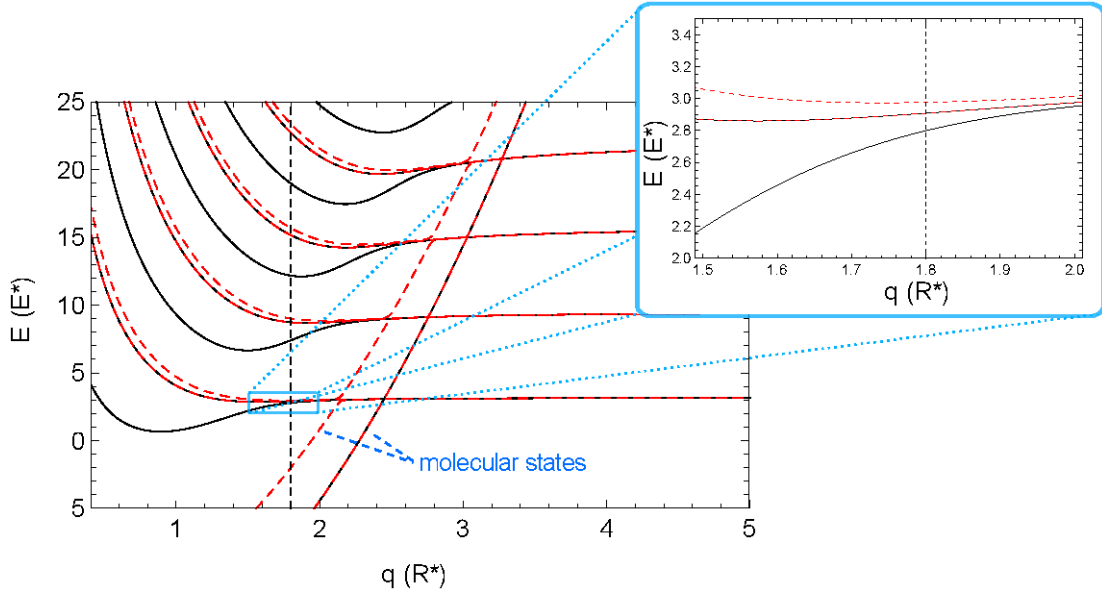


**Figure 2.4.:** Spectrum for one  $^{87}\text{Rb}$  atom and one  $^{171}\text{Yb}$  ion. The black, solid lines represent the spectrum for  $\phi_e = -\pi/4$  and  $\phi_o = \pi/4$ . The red, dashed lines represent  $\phi_e = \pi/4$  and  $\phi_o = \pi/3$ . The blue box offers an enlarged view of this spectrum for the ground state in the region of interest. Here, the strength of the splitting at the black, dashed line at  $q = 1.8 R^*$  differs for both spectra depending on the values of  $\phi_e$  and  $\phi_o$  (We note that the black, solid line for  $\phi_o = \pi/4$  and the red, dashed line for  $\phi_e = \pi/4$  are overlapped with each other because the Hamiltonian conserves parity).

We consider a system of  $^{87}\text{Rb}$  and  $^{171}\text{Yb}^+$ . For these species we obtain  $E^*/h = 935$  Hz and  $R^* = 306$  nm. The parameter  $\alpha_a$  is chosen to be  $\alpha_a = 10$  corresponding to a local trap frequency of  $\omega_a = 2\pi \times 1.794$  kHz. The spectrum as a function of the inter-well distance  $q$  is illustrated in fig. 2.4. The black, solid lines represent the spectrum for

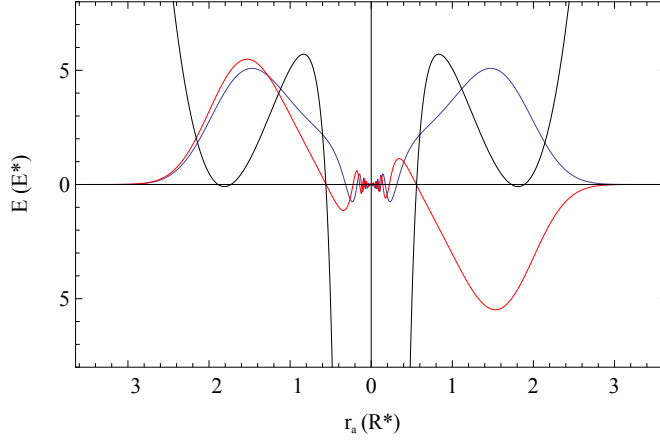


**Figure 2.5.:** Wave functions for the ground state (blue) and the first excited state (red) for a double well potential with  $q = 1.8 R^*$  and  $\alpha_a = 10$ . The double well potential including atom-ion interaction is shown in black.

$\phi_e = -\pi/4$  and  $\phi_o = \pi/4$ , the red, dashed lines represent the spectrum for  $\phi_e = \pi/4$  and  $\phi_o = \pi/3$ . This spectrum illustrates the short-range phase dependence of the double well problem. For large inter-well distances the spectrum is degenerate as there is no coupling between the wells, such that the spectra are equal to that of a harmonic oscillator, i.e. the level spacing is equidistant. For smaller distances the coupling is getting stronger such that the degeneracy of both spectra is lifted as the energies for even and uneven wave functions (eqs. (2.7, 2.8)) start to differ. In particular, the states corresponding to the trap ground states split in symmetric and antisymmetric superpositions given by:

$$\Phi_{g,e}(\mathbf{r}) = \frac{1}{\sqrt{2}} (\Phi_L(\mathbf{r}) \pm \Phi_R(\mathbf{r})) \quad (2.16)$$

with the energies  $E_g$  and  $E_e$  where  $\Phi_{L,(R)}$  is the wave packet located in left (right) well [61]. This can also be seen in fig. 2.5 where the wave functions for the ground state (blue) and the first excited state (red) are shown as a function of the inter-well distance  $2q$  and in fig. 2.6 which shows the even and odd wave functions also for the first few excited states and a molecular state<sup>2</sup>. When the energy splitting  $\Delta E = E_g - E_e$  is much smaller than the energy gap to the other levels in the spectrum we can employ a two-mode approximation [54] with the inter-well coupling  $J$  which is given by:

$$J = \frac{\Delta E}{2\hbar} \quad (2.17)$$

For  $\phi_e = -\pi/4$ ,  $\phi_o = \pi/4$  the tunnelling rate at  $q = 1.8 R^*$  (black, dashed line) is  $J = 2\pi \cdot 90$  Hz and for  $\phi_e = \pi/4$ ,  $\phi_o = \pi/3$  it is  $J = 2\pi \cdot 60$  Hz. Since the short-range

<sup>2</sup>Although the molecular states have a lower energy, we always refer to the ground state as the state that can be associated with the trap ground state for large well separation.

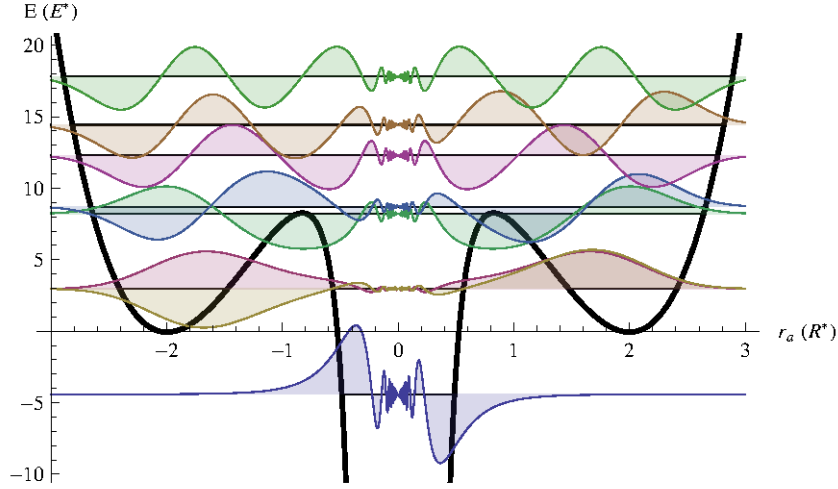


**Figure 2.6.:** Wave functions for a double well with  $q = 2R^*$  and  $\alpha_a = 10$  (compare to fig. 2.4). The double well potential including atom-ion interaction is shown in black.

phase depends on the spin of the ion, we can conclude that this spin can control the tunnelling of the atom. The dependence of the inter-well coupling  $J$  to the short-range phase  $\phi$  is relatively large such that it should be measurable. We can therefore treat  $J$  as an operator which is given by:

$$\hat{J} = J_{\downarrow} |\downarrow\rangle \langle \downarrow| + J_{\uparrow} |\uparrow\rangle \langle \uparrow| \quad (2.18)$$

### 2.2.2. Many-body scenario

To deal with more atoms, we introduce the usual operators  $\hat{c}_i$  ( $\hat{c}_i^\dagger$ ) ( $i = L, R$ ) annihilating (creating) atoms in the left ( $L$ ) or right ( $R$ ) well ground state. The condition for employing this two-mode approximation is that the energy splitting  $\Delta E$  is much smaller than the energy gap to neighbouring levels [51].

For the many-body system we end up at an effective description given by the Bose-Hubbard Hamiltonian:

$$\hat{H}_{\text{BH}} = \hbar \hat{J} \hat{\alpha} + \hbar \hat{U} \hat{n}^2 = \hbar \hat{J} \left( \hat{c}_L^\dagger \hat{c}_R + \hat{c}_R^\dagger \hat{c}_L \right) + \hbar \hat{U} \frac{1}{4} \left( \hat{c}_R^\dagger \hat{c}_R - \hat{c}_L^\dagger \hat{c}_L \right)^2 \quad (2.19)$$

where  $\hat{\alpha}$  is the tunnelling operator,  $\hat{n}$  considers imbalances of the populations in both wells and  $\hat{U}$  is an operator for the on-site atom-atom interaction [54]. Using the single-particle wave function we can estimate the on-site atom-atom interaction energy [61]:

$$U = E^* \frac{U_0}{\hbar} \int d\mathbf{r} |\Phi_L(\mathbf{r})|^4 \quad (2.20)$$

where  $U_0 = 8\pi a_{s,Rb}\mu/m_a R^*$  measures the strength of the atom-atom interaction and  $a_{s,Rb} = 106 \cdot a_0$  is the atom-atom s-wave scattering length for  $^{87}\text{Rb}$  where  $a_0$  is the Bohr radius. Since the wave functions depend on the short-range phases, also  $\hat{U}$  (like  $\hat{J}$ ) depends on the spin of the ion and is an operator.

With this description of the many-body system we can describe interesting interactions such as self-trapping [62] and entanglement [63]. Following [67] we introduce the interaction parameter  $\Lambda = U N/2 J$  where  $N$  is the total number of atoms. For  $\Lambda > \Lambda_c = 2$ , a state which is initially localized in one well is predicted to remain in this well. We are therefore in the self-trapping regime. We can plot the time-dependend relative population

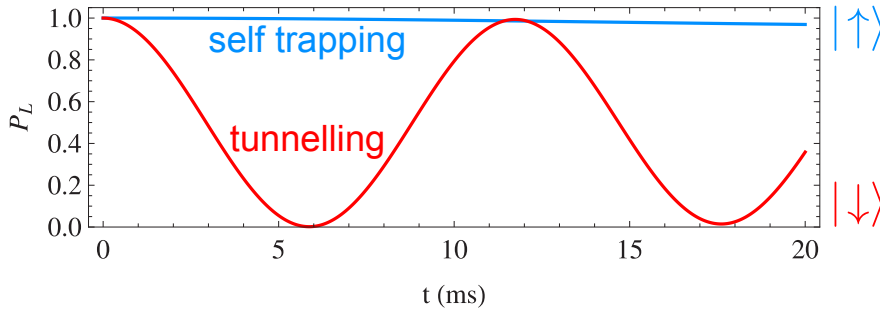


**Figure 2.7.:** Relative population in the left well as function of time for  $N = 20$  atoms,  $\alpha = 0.026$ ,  $\omega_a = 2\pi \cdot 200\text{Hz}$ ,  $q = 6.39R^*$ ,  $\phi_\uparrow = -\frac{\pi}{4}$  and  $\phi_\downarrow = \frac{\pi}{4}$  based on three-dimensional calculations [51].

in the left well for  $N = 20$  atoms,  $\phi_\uparrow = -\frac{\pi}{4}$  and  $\phi_\downarrow = \frac{\pi}{4}$  (see fig. 2.7). This plot is based on three-dimensional calculations [51] and was obtained by numerically integrating the Schrödinger equation for the Hamiltonian 2.19. Because it is three-dimensional there is only one short range phase per spin state. For  $N = 20$  atoms we obtain interaction parameter values of  $\Lambda^\uparrow = 5.2 > \Lambda_c$  and  $\Lambda^\downarrow = 0.32 < \Lambda_c$  which means that for an ion with  $|\uparrow\rangle$  we are in the self-trapping regime and for an ion with  $|\downarrow\rangle$  we are in the Rabi regime where the atoms are oscillating between the two wells via tunnelling.

## 2.3. Double well with moving ion

We now consider a system similar to the one in section 2.2 but now we allow the ion to move. In this case the Hamiltonian for a single ion and atom is given by:

$$H = \underbrace{\frac{p_i^2}{2m_i} + \frac{1}{2}m_i\omega_i^2 r_i^2}_{H_i} + \underbrace{\frac{p_a^2}{2m_a} + V_{\text{dw}}(r_a)}_{H_a} - \underbrace{\frac{C_4}{(r_i - r_a)^4}}_{H_{ia}}, \quad (2.21)$$

where  $p_i = -i\hbar\partial/\partial r_i$  is the momentum of the ion,  $m_i$  its mass and  $\omega_i$  is the ion trap frequency. Now that the ion and the atom are moving, the interaction term  $H_{ia}$  depends

## 2. Dynamics of an ion-controlled Josephson junction

---

on the relative coordinate ( $r_i - r_a$ ). Hence it is reasonable to rewrite the Hamiltonian in terms of center of mass (COM) and relative coordinates, using:

$$R = \frac{m_i r_i + m_a r_a}{m_i + m_a} \quad (\text{COM coordinate}) \quad (2.22)$$

$$r = r_i - r_a \quad (\text{relative coordinate}) \quad (2.23)$$

$$M = m_i + m_a \quad (\text{total mass}) \quad (2.24)$$

$$\mu = \frac{m_i m_a}{m_i + m_a} \quad (\text{reduced mass}) \quad (2.25)$$

$$\omega_R = \frac{m_i \omega_i^2 + m_a \omega_a^2}{m_i + m_a} \quad (2.26)$$

The Hamiltonian can now be written as the following sum:

$$H = H_R^{(0)} + H_r^{(0)} + H^{(1)}, \quad (2.27)$$

where  $H_R^{(0)}$ ,  $H_r^{(0)}$  and  $H^{(1)}$  are given by:

$$H_R^{(0)} = -\frac{\hbar^2}{2M} \frac{\partial^2}{\partial R^2} + \frac{1}{2} M \omega_R^2 R^2 \quad (2.28)$$

$$H_r^{(0)} = -\frac{\hbar^2}{2\mu} \frac{\partial^2}{\partial r^2} + \frac{1}{2} \mu \omega_r^2 r^2 - \frac{C_4}{r^4} \quad (2.29)$$

$$H^{(1)} = \mu(\omega_i^2 - \omega_a^2) R r + V_{\text{dw}}(R, r) - \frac{\mu \omega_a^2}{2} \left( \frac{m_a}{\mu} R^2 + \frac{\mu}{m_a} r^2 + R r \right). \quad (2.30)$$

Eq. 2.28 is the Hamiltonian of a harmonic oscillator with the mass  $M$ , the coordinate  $R$  and the trap frequency  $\omega_R$ . The solutions of this Hamiltonian are therefore Fock states  $f_n(R)$  with energies  $E_n = \hbar \omega_R (n + \frac{1}{2})$  where  $n = a^\dagger a$  is the particle number. Eq. 2.29 is similar to  $H_a^{(0)}$  in eq. 2.4 for a fixed ion (section 2.2). As described in that section we can solve the corresponding Schrödinger equation using quantum defect theory. The solutions of this problem are the wave functions  $\Phi_k(r)$  with the energies  $E_k$ . The terms in eq. 2.30 can be understood as follows: The first term  $\mu(\omega_i^2 - \omega_a^2) R r$  expresses the effect to the system due to the mismatch between the ionic and atomic trap frequencies. The second term  $V_{\text{dw}}(R, r)$  is the double well potential in COM and relative coordinates and the third term  $-\frac{\mu \omega_a^2}{2} \left( \frac{m_a}{\mu} R^2 + \frac{\mu}{m_a} r^2 + R r \right)$  corresponds to  $-\frac{1}{2} m_a \omega_a^2 r_a^2$  which was transformed in the new coordinates. This term was added to simplify eqs. (2.28,2.29) and now it is subtracted again.

It is useful to introduce the following parameters:

$$\gamma = \frac{\omega_i}{\omega_a}, \quad \alpha = \left( \frac{\hbar \omega_r}{2E^*} \right)^2, \quad \beta^2 = \frac{1}{M} (m_i + \gamma^2 m_a), \quad B^2 = \frac{m_a + \gamma^2 m_i}{m_i + \gamma^2 m_a}.$$

With these parameters and in units of  $E^*$  and  $R^*$  the Hamiltonians take the form:

$$H_R^{(0)} = -\frac{\mu}{M} \frac{\partial^2}{\partial R^2} + \frac{M}{\mu} B^2 \alpha R^2, \quad (2.31)$$

$$H_r^{(0)} = -\frac{\partial^2}{\partial r^2} + \alpha r^2 - \frac{1}{r^4}, \quad (2.32)$$

$$\begin{aligned} H^{(1)} = & -\frac{\alpha}{\beta^2} \left( \frac{\mu}{m_a} M^{(2)} - 2\gamma R \otimes M^{(1)} + \frac{m_a}{\mu} R^2 \right) \\ & + \frac{\alpha m_a}{\mu \beta^2} \left( \frac{q^2}{4} - \frac{m_i^2}{2M^2} M^{(2)} + \frac{m_i^4}{4M^4 q^2} M^{(4)} \right. \\ & \quad \left. + \frac{m_i}{M} R \otimes M^{(1)} - \frac{m_i^3}{M^3 q^2} R \otimes M^{(3)} - \frac{1}{2} R^2 \right. \\ & \quad \left. + \frac{3m_i^2}{2M^2 q^2} R^2 \otimes M^{(2)} - \frac{m_i}{M q^2} R^3 \otimes M^{(1)} + \frac{1}{4q^2} R^4 \right), \quad (2.33) \end{aligned}$$

with the matrix elements

$$M_{kk'}^{(j)} = \int \Phi_{k'}^*(r) r^j \Phi_k(r) dr. \quad (2.34)$$

The Hamiltonian can be diagonalized in the basis  $|f_n(R)\Phi_k(r)\rangle$ .

As an example we again consider a system of a single  $^{87}\text{Rb}$  atom and a single  $^{171}\text{Yb}^+$  ion. This is illustrated in fig. 2.8 where the resulting correlation spectrum (black line) compared to the same system but neglecting the atom-ion interaction (red, dashed line) are plotted as a function of the inter-well distance  $2q$ . The parameters are chosen to be:  $\alpha = 10$ ,  $\gamma = 5.5$ ,  $\phi_e = -\pi/4$ ,  $\phi_o = \pi/4$ . Due to the fact that the ion is now allowed to move these spectra look more complicated than in fig. 2.4. At large inter-well distances the Fock states ( $|00\rangle$ ,  $|10\rangle$ , ...) are the same for both spectra. This is because for large distances the ion and the atom are localized in well separated traps hence the atom-ion interaction is very small. This slightly changes for atom states of higher order. Here, the interaction has an effect even for large separations of the traps.

The corresponding probability distributions that asymptotically are related to the states  $|00\rangle$ ,  $|02\rangle$ ,  $|10\rangle$  and  $|11\rangle$  for an inter-well distance of  $q = 2.55R^*$  (green circles in fig. 2.8) are shown in fig. 2.9. These clearly illustrate the probability of finding the atom at a point  $r_a$  and the ion at a point  $r_i$ , with black (white) being high (zero) probability. For  $r_a - r_i \gg 0$  the states somewhat resemble the Fock states, with the number of nodes in each direction giving the quantum numbers  $|nm\rangle$  for the ion and the atom. For short ranges ( $r_a - r_i \approx 0$ ) atom-ion interactions dominate such that there are many sharp features in the wave functions which are not completely resolved in the plot.

We can also calculate the resulting correlation spectrum of this system as a function of the inter-well distance  $2q$  for the special case when  $\alpha = \left(\frac{\hbar\omega_r}{2E^*}\right)^2 = 100$ ,  $\gamma = \frac{\omega_i}{\omega_a} = 1$ ,  $\phi_e = -\pi/4$ ,  $\phi_o = \pi/4$  (see fig. 2.10). This plot illustrates the initial degeneracy of each

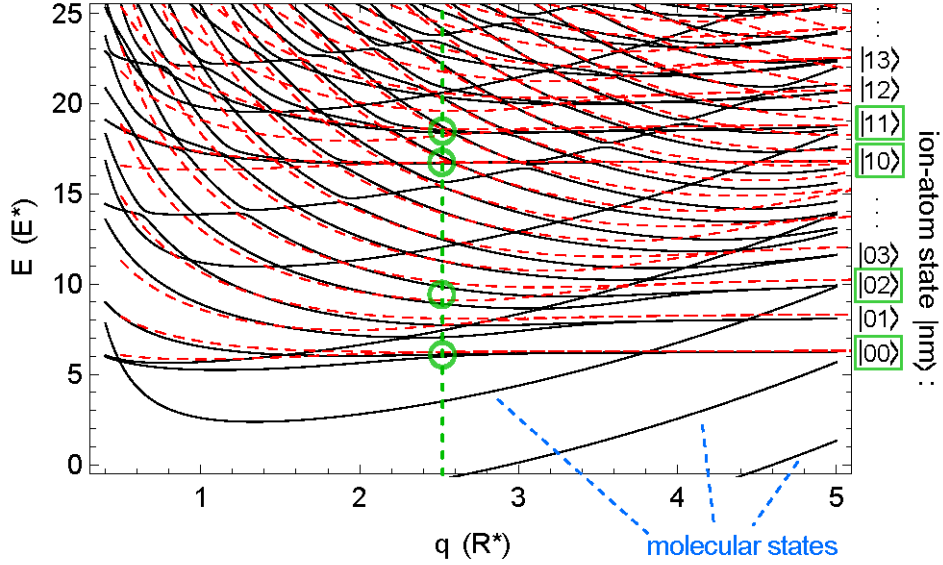


**Figure 2.8.:** Spectrum of double well with moving ion (black line) compared to the same system but neglecting the atom-ion interaction (red, dashed line) for  $^{87}\text{Rb}$  and  $^{171}\text{Yb}^+$  with  $\alpha = 10$ ,  $\gamma = \frac{\omega_i}{\omega_a} = 5.5$ ,  $\phi_e = -\pi/4$ ,  $\phi_o = \pi/4$  corresponding to  $\omega_a = 2\pi \times 1.794$  kHz and  $\omega_i = 2\pi \times 9.868$  kHz.

state for large inter-well distances  $q$  as the trap frequencies of the atom and ion are the same. The degeneracy is determined by counting the energy levels originating from each state as  $q$  is decreased.

## 2.4. The effect of imperfect ion cooling on tunnelling

Previous calculations always assumed the ideal case with ground state cooled ions [51]. In this section we will make a simple model prediction of how imperfect cooling of the ion will affect the atomic tunnelling between the two wells. An enlarged view of the five first Fock states obtained in fig. 2.8 can be seen in fig. 2.11. These are very helpful in understanding the behaviour of such a system. In an experiment we would initially prepare a system of a ground state cooled ion and an atom cloud located in one of the two wells with large inter-well separation  $q$ . If we consider a single atom located in the left well the corresponding ground state is  $|00\rangle_L$ . For this state the curve looks very similar to the one in fig. 2.4 such that our assumption of a static ion was justified. As for the fixed ion we get tunnelling by decreasing the inter-well distance  $q$  causing the ground state to split which is for a moving ion given by:

$$|00\rangle_L \rightarrow \frac{1}{\sqrt{2}} |0\rangle (|\Phi_e - \Phi_g\rangle), \quad (2.35)$$

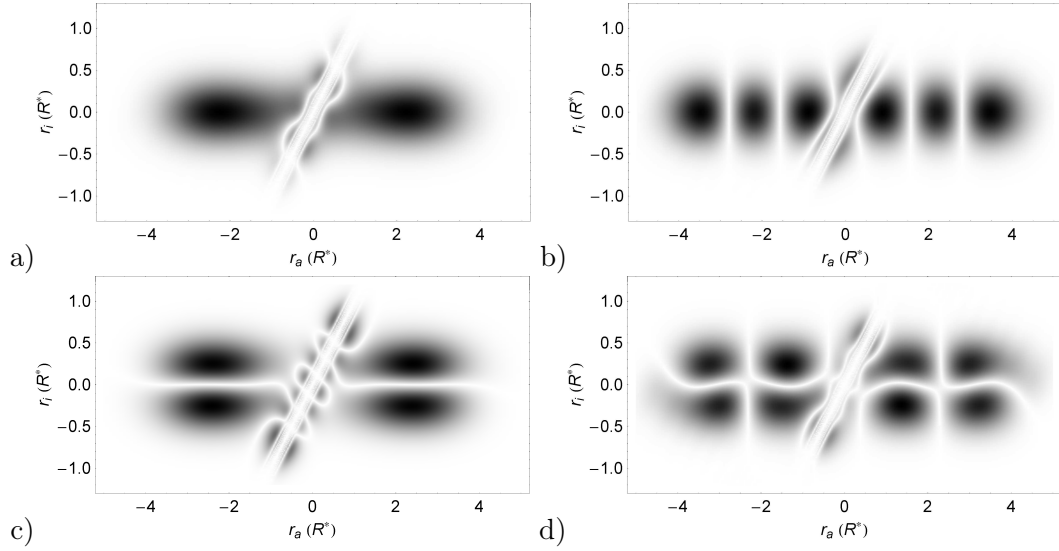


**Figure 2.9.:** a)-d): Probability distributions of the ion-atom states asymptotically corresponding to  $|00\rangle$ ,  $|02\rangle$ ,  $|10\rangle$  and  $|11\rangle$  for an inter-well distance of  $q = 2.55R^*$  for  $^{87}\text{Rb}$  and  $^{171}\text{Yb}^+$  with  $\alpha = 10$ ,  $\gamma = \frac{\omega_i}{\omega_a} = 5.5$ ,  $\phi_e = -\pi/4$ ,  $\phi_o = \pi/4$  corresponding to  $\omega_a = 2\pi \times 1.794$  kHz and  $\omega_i = 2\pi \times 9.868$  kHz.

where the tunnelling rate is given by the energy difference  $\Delta E = E_g - E_e$  between the states  $\Phi_g$  and  $\Phi_e$  (eq. 2.17). For further considerations it is convenient to include the vibrational quantum number  $n$  of the ion such that the states are given by  $|\Phi_e\rangle_n$  and  $|\Phi_g\rangle_n$ . The curve for the state  $|10\rangle_L$  looks very similar to the one for  $|00\rangle_L$  but around  $q = 3.1R^*$  an avoided crossing appears making it harder to keep track of  $|\Phi_e\rangle_n$  and  $|\Phi_g\rangle_n$ . While decreasing  $q$  further even more avoided crossings appear. This could lead to trouble in an experiment where we want to prepare such states with well defined inter-well coupling. To achieve that the avoided crossings need to be passed diabatically but without exciting the atoms' motion. For  $|00\rangle_L$ ,  $|10\rangle_L$ ,  $|20\rangle_L$  and  $|30\rangle_L$  we are still able to keep track of  $|\Phi_e\rangle_n$  and  $|\Phi_g\rangle_n$  with great certainty but for  $|n0\rangle_L$  with  $n \geq 4$  this is associated with a relatively large degree of uncertainty making it almost impossible to prepare the desired system.

To fully understand this problem the Schrödinger equation for dynamically changing  $q(t)$  needs to be solved while keeping track of all probability amplitudes for each avoided crossing. A simplified approach is to assume that we already prepared a mixture of the states represented by the four red dots in fig. 2.11. We therefore only take into account states with  $n < 4$  which simplifies the problem extraordinarily. In this case we can assume that we start with a mixture of superpositions  $\frac{1}{\sqrt{2}} (|\Phi_e\rangle_n - |\Phi_g\rangle_n)$  such that

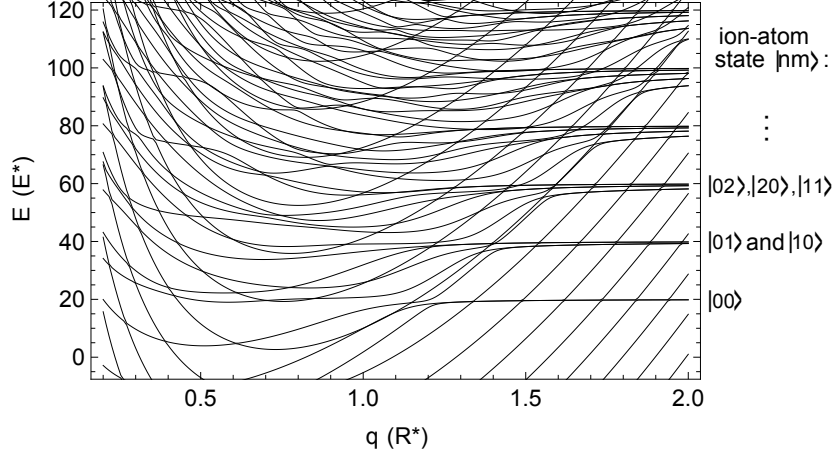


**Figure 2.10.:** Double well spectrum with moving ion for  $^{87}\text{Rb}$  and  $^{171}\text{Yb}^+$  with  $\alpha = 100$ ,  $\gamma = 1$ ,  $\phi_e = -\pi/4$ ,  $\phi_o = \pi/4$ .

the atom is mostly in the left well. We include the thermal nature of the system by weighting these superpositions with a thermal distribution given by:

$$P_n(\bar{n}) = \frac{1}{1 + \bar{n}} \left( \frac{\bar{n}}{\bar{n} + 1} \right)^n, \quad (2.36)$$

where  $\bar{n}$  corresponds to the average number of vibrational quanta in the ion in the asymptotic state. Since  $n > 4$ ,  $\bar{n}$  is limited to small values. For this model the energy difference  $\Delta E^{(n)} = E_g^{(n)} - E_e^{(n)}$  between each pair of states is given by:

$$\vec{J} = (0.0146, 0.0137, 0.0057, 0.0070)E^* \quad (2.37)$$

We achieve very stable tunnelling due to the similarity of the first two values that are most prominent in this distribution. Since these values are much bigger than the other two values we can estimate that with increasing  $\bar{n}$  the tunnelling will die out slowly. To determine the tunnelling dynamics we compute the square of the overlap with the initial state after some time  $t$ . The dynamics of each state is given by:

$$|\psi(t)\rangle_n = e^{-\frac{iE_e^{(n)}t}{\hbar}} |\Phi_e\rangle_n + e^{-\frac{iE_g^{(n)}t}{\hbar}} |\Phi_g\rangle_n, \quad (2.38)$$

and since it is a thermal problem we end up with an incoherent sum of frequencies to estimate the probability of finding the atom once more in the left state after some time  $t$  which is given by:

$$P_L(\bar{n}) = \sum_n P_n | \langle \psi(0) | \psi(t) \rangle_n |^2 = \frac{1}{2} + \frac{1}{2} \sum_n P_n \cos\left(\frac{J_n t}{\hbar}\right) \quad (2.39)$$

The resulting tunnelling dynamics for  $\bar{n} = 0, 0.3$  and  $0.6$  are shown in fig. 2.12. Since we are only considering the dynamics for  $n < 4$  we cut the thermal distribution (eq. 2.36)

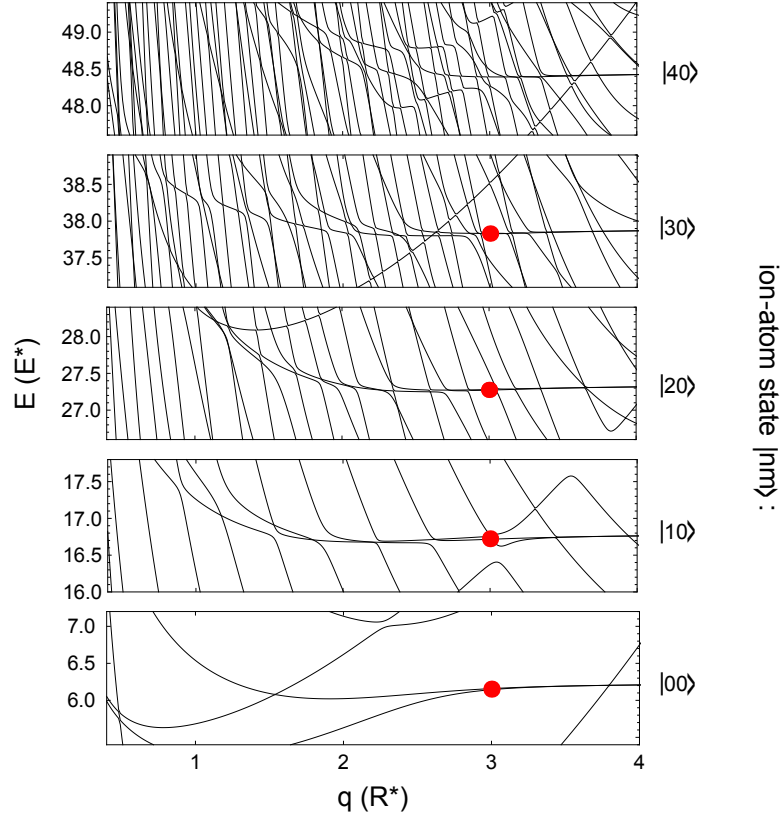


**Figure 2.11.:** Enlarged view of the five first Fock states of the ion in the spectrum of a double well with moving ion for  $^{87}\text{Rb}$  and  $^{171}\text{Yb}^+$  with  $\alpha = 10$ ,  $\gamma = \frac{\omega_i}{\omega_a} = 5.5$ ,  $\phi_e = -\pi/4$ ,  $\phi_o = \pi/4$  corresponding to  $\omega_a = 2\pi \times 1.794$  kHz and  $\omega_i = 2\pi \times 9.868$  kHz. Every red dot actually indicates an even and an uneven state while the tunnelling rate is given by the energy difference between these states (see text).

such that part of the population is neglected. For example, for  $\bar{n} = 0.6$  still 98% of the population is included. Even for this large fraction value the neglecting affects the system in such a way that the tunnelling amplitude goes down far less than we would expect for non-pure state dynamics. For larger values of  $\bar{n}$  we will require more sophisticated methods such that we can perform time-dependent analysis of the complex problem. However it is clear that for small time scales and small average quantum number  $\bar{n}$ , we can expect reasonable tunnelling dynamics. In the present example, the tunnelling is also more robust due to the similarity of the tunnelling rate for  $n = 0$  and  $n = 1$ , the two largest populations in the thermal distribution. A next step in this calculation would be to include dissipation, such as ion heating and/or cooling, and studying the many-body scenario.

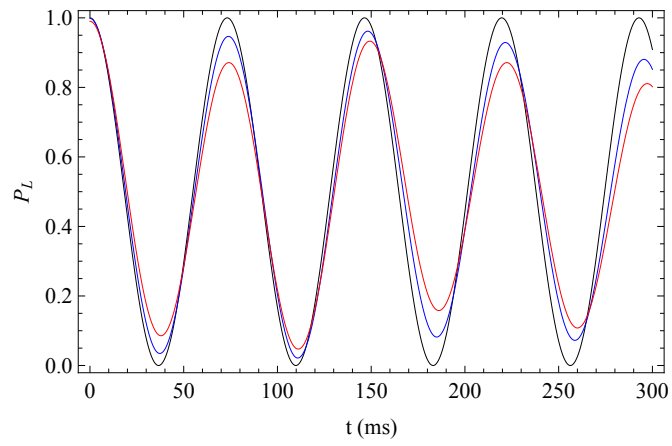


**Figure 2.12.:** Probability of finding the atom once more in the left well after some time  $t$  for a thermal ion state with  $\bar{n} = 0, 0.3, 0.6$  corresponding to black, blue and red respectively.

# 3

## Trap design

In this chapter the design and development of a combined atom-ion micro trap is documented and explained in detail.

### 3.1. General considerations

There are numerous ways to realize a combined atom-ion micro trap. The most straight forward approach being glueing a planar ion trap to an atom chip. A more intricate design where the trapping fields are derived from the same structures would however give benefits in trap depth and stability and we were first considering a trap of this kind. However, this introduces also a number of problems such as heating of the chip due to the atom trap wires which carry relatively high currents, and it requires very complicated designs to generate the correct fields for both, atoms and ions, which could cause new problems. Another big disadvantage of this design is that the ions can directly sense the electric field of the atom trap wires which can perturb the ion trap.

We decided to use a fully developed and tested ion trap chip and to design a planar atom trap which we can mount beneath the ion trap. This simplifies the problem significantly because here we don't have the task to invent a completely new design as each technique itself already exists. Another advantage of this design is that we can concentrate on good heat dissipation from the atom trap wires to the heat sink which enables us to work with higher currents. The big disadvantage of this design is that we have to align the chips to each other with high precision and the atomic trap depth is reduced by the nearby surface. Care must be taken to ensure that the ion trap surface is parallel to the atom trap surface and that both trapping axes are placed directly above one another.

### 3.2. The atom-ion micro trap

An exploded view of the design of the combined atom-ion micro trap developed in this thesis is shown in fig. 3.1. It primarily consists of a big octagonal chip with an outside diameter of 45 mm which is used as the surface for the atom trap wires (section 3.4)

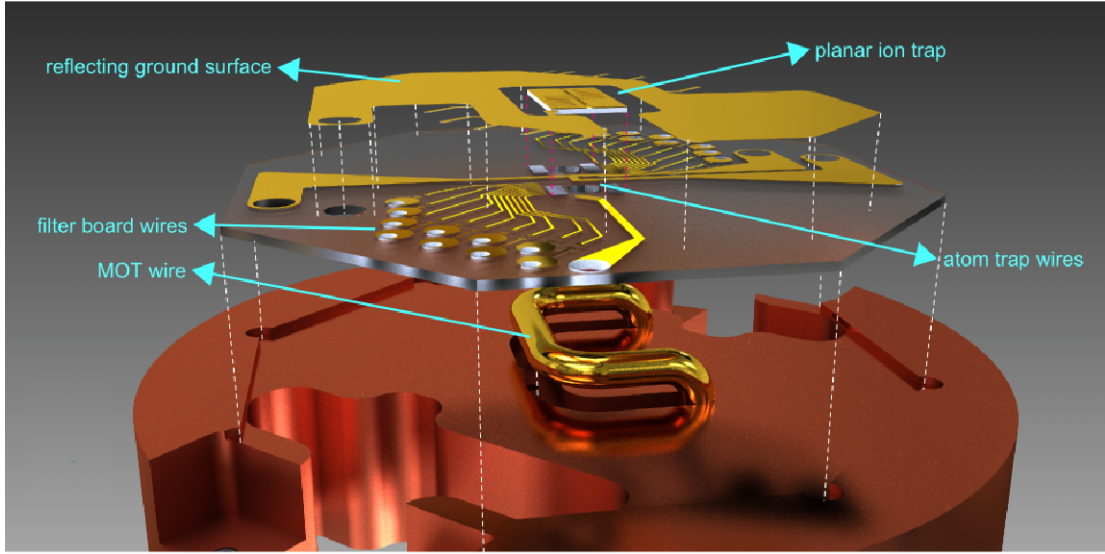


**Figure 3.1.:** Exploded view of the design of our hybrid atom-ion micro trap.

and for the filter board of the ion trap (section 3.3) which is to be glued to the atom trap using a UV adhesive<sup>1</sup>. The chip is currently being build at the physics faculty in Siegen. A wire bonder<sup>2</sup> enables us to connect the electrical circuits of the ion trap with the filter board at the atom trap chip. The chip will also feature a second isolated gold layer which is grounded and which serves on the one hand to protect the wires and on the other hand to reflected the MOT laser beams as explained later. Right beneath the chip there is a big u-shaped wire which will be needed to form the magnetic field of the magneto optical trap (section 3.4.1).

### 3.3. The ion micro trap

#### 3.3.1. Ion trapping and the secular approximation

An ion trap is a (dynamic) system spatially confining charged particles (e.g. ions) over an extended period of time. A harmonic Coulomb potential that would trap ions is given by:

$$\Phi(x, y, z, t) \propto \alpha_x x^2 + \alpha_y y^2 + \alpha_z z^2 \quad (3.1)$$

where  $\alpha_i > 0$ . Unfortunately, the Maxwell equations prevent us from forming such electric potentials, as can be seen from the Laplace equation  $\Delta\Phi(x, y, z, t) = 0$ . However, a time dependent field can be used to overcome this problem, and the resulting trap

<sup>1</sup>Epoxy Technology: EPO-TEK® OG142-112 UV Cure Optical Epoxy

<sup>2</sup>TPT: HB10 Wedge and Ball Bonder

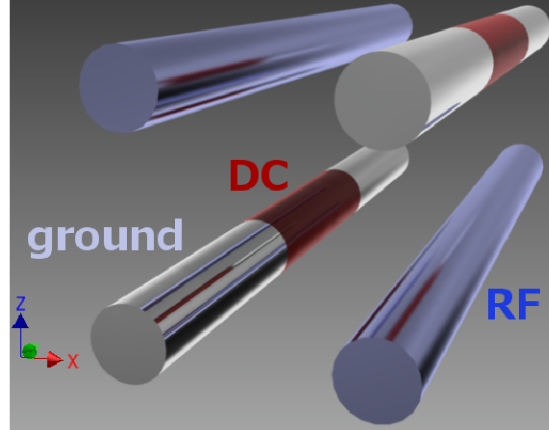


**Figure 3.2.:** Scheme of a linear Paul trap.

is known as a Paul trap, after its inventor. We consider a dynamic potential that can be split in a harmonic time-independent static part and a time-dependent oscillating part driven with a radio frequency (RF) with frequency  $\Omega$ . Here, always one  $\alpha_i$ -value is smaller than zero but due to inertia we get an effective trapping. The resulting potential is given by:

$$\Phi(x, y, z, t) = U \frac{1}{2} (\alpha_x x^2 + \alpha_y y^2 + \alpha_z z^2) + \tilde{U} \cos(\Omega t) \frac{1}{2} (\beta_x x^2 + \beta_y y^2 + \beta_z z^2) \quad (3.2)$$

The Laplace equation sets the following constrains:

$$\alpha_x + \alpha_y + \alpha_z = 0 \quad (3.3)$$

$$\beta_x + \beta_y + \beta_z = 0 \quad (3.4)$$

A common ion trap is the linear Paul trap consisting of four bar-shaped electrodes (see fig. 3.2) with:

$$\alpha_x + \alpha_y = -\alpha_z \quad \text{and} \quad \beta_x = -\beta_y, \beta_z = 0 \quad (3.5)$$

The RF voltage is applied to two opposing electrodes and the other two electrodes are segmented in three parts respectively while the middle parts are applied to a DC voltage and the remaining parts are grounded [32].

Typically the motion of a trapped ion is investigated by considering it as a harmonic oscillator while neglecting the micromotion due to the RF field. But there is evidence that micromotion changes the atom-ion interaction [6, 68].

One way to find the motion of the ion is to solve this problem classically following [32]. In anticipation of future work on solving the double-well problem including micromotion, we treat the quantum case here, following [6].

### 3. Trap design

---

The motion of an ion is governed by the Schrödinger equation:

$$i\hbar \frac{\partial}{\partial t} \Psi(\vec{x}, t) = H(t) \Psi(\vec{x}, t) \quad (3.6)$$

and in typical Paul traps the dynamics along the three spatial dimensions is decoupled, so that we can limit ourselves to a single dimension here. For the x-axis the associated Hamiltonian  $H(t)$  is given by:

$$H(t) = \frac{P^2}{2m_i} + \frac{1}{8} m_i \Omega^2 x^2 [a + 2q \cos(\Omega t)] \quad (3.7)$$

where  $m_i$  is the mass of the ion and  $\Omega$  is the frequency of oscillating potential.  $a$  and  $q^3$  are trap parameters depending on  $m_i$ ,

$\Omega$  and the charge of the ion  $e$ . For typical Paul traps  $a \ll q$  and  $0 < q < 4$ . The Hamiltonians in  $y$ - and  $z$ -direction have similar forms but different values for  $a$  and  $q$  while obeying the constraints set in eq. 3.5 with:

$$a_x = a_y = -\frac{1}{2} a_z = a \quad \text{and} \quad q_x = -q_y, q_z = 0 \quad (3.8)$$

As a result of the electric potential (eq.3.2) the motion of the ion is an oscillation which consists of a slow, harmonic secular motion with the frequency  $\omega_i$  and the micromotion with the frequency  $\Omega$ . These are related to each other by:

$$\omega_i = \frac{\Omega}{2} \sqrt{a + \frac{q^2}{2}} \quad \text{with} \quad |q| \ll 1 \quad \text{and} \quad |a| \ll q^2 \quad (3.9)$$

If  $\Omega$  is a high frequency, the RF-potential has little effect on the particle motion because it averages to zero over the short time period  $\frac{2\pi}{\Omega}$ . Hence the micromotion vanishes such that only the (harmonic) secular oscillation with the frequency  $\omega_i$  remains. This is the basis for the secular approximation.

Following [69] we make the following ansatz for the wave function to study the quantum case:

$$\Psi(x, t) = \exp \left[ -\frac{i}{4\hbar} m_i q \Omega x^2 \sin(\Omega t) \right] \Phi(x, t) \quad (3.10)$$

Here, the idea is that most of the fast oscillating terms are included in the exponent. Hence, we can consider  $\Phi(x, t)$  as a wave function for the secular motion. This results in the following Schrödinger equation for  $\Phi(x, t)$ :

$$\begin{aligned} i\hbar \frac{\partial}{\partial t} \Phi(x, t) &= \left[ -\frac{\hbar^2}{2m_i} \frac{\partial^2}{\partial x^2} + V_{\text{eff}}(x) \right] \Phi(x, t) \\ &= \left[ -\frac{\hbar^2}{2m_i} \frac{\partial^2}{\partial x^2} + \frac{1}{2} m_i \omega_i^2 x^2 - m_i (\gamma' \omega_i)^2 x^2 \cos(2\Omega t) \right. \\ &\quad \left. + 2i\hbar \gamma' \omega_i \left( x \frac{\partial}{\partial x} + \frac{1}{2} \right) \sin(\Omega t) \right] \Phi(x, t) \end{aligned} \quad (3.11)$$

---

<sup>3</sup>We note that this parameter  $q$  is not to be confused with the inter-well separation used in the previous chapter.

where  $V_{\text{eff}}(x)$  is the time-independent potential energy and  $\gamma'$  is given by:

$$\gamma' = \frac{1}{\sqrt{2\left(1 + \frac{2a}{q^2}\right)}} \quad (3.12)$$

The corresponding Hamiltonian  $H_{\text{eff}}(t)$  for the solution  $\Phi(x, t)$  is therefore given by:

$$H_{\text{eff}}(t) = \frac{p^2}{2m_i} + \frac{1}{2}m_i\omega_i^2x^2 - m_i(\gamma'\omega_i)^2x^2 \cos(2\Omega t) - \gamma'\omega_i\{x, p\} \sin(\Omega t) \quad (3.13)$$

where  $\{x, p\}$  is the anticommutator of the position and momentum operators. The first two terms represent an harmonic trap at the secular frequency, while the latter two terms represent the effects of the micromotion. It can be shown [6] by employing Floquet theory, that these last terms are unimportant when considering only ions. This is the quantum mechanical basis for the secular approximation.

When the ion is strongly interacting with another system, such as atoms, the effects can also be studied using Floquet theory [6] and the picture changes. In a next step, we plan to take these last two terms into account in the calculation of the double well problem discussed in chapter 2. Unfortunately, the necessary Floquet theory results in an extremely large Hilbert space, and we have not been able to tackle the full problem up until now. We note that the analysis is more complicated than the one in [6] as the present problem inherently prevents making static approximations for either ion or atom.

### 3.3.2. Design of the planar ion trap

The trap we will use in the experiment was made kindly available by Prof. Hartmut Häffner from the *Quantum Information with Trapped Ions*-group<sup>4</sup> at UC Berkeley. It is a micro-fabricated surface electrode segmented trap with a trapping height of 100  $\mu\text{m}$ . The chip itself has a length of 9 mm, a width of 4.5 mm and a thickness of 500  $\mu\text{m}$  and it features a slit, 100  $\mu\text{m}$  wide and 6.5 mm long, right below the trapping region which will be used to load atoms through (section: 3.2).

The fabrication process of this chip works as follows: the electrode structure is etched on a fused silica<sup>5</sup> substrate using a combination of laser weakening and HF-etching<sup>6</sup> followed by evaporation of four metal layers. The metal layers are 20 nm Titanium, 150 nm gold, 20 nm Titanium and 150 nm gold, i.e. 300 nm gold in total [70].

<sup>4</sup><http://www.physics.berkeley.edu/research/haeffner/>

<sup>5</sup>Non-crystalline glass of silicon dioxide ( $\text{SiO}_2$ )

<sup>6</sup>HF-etching: Hydrofluoric acid is used to etch structures. It has a strong corrosive characteristic against  $\text{SiO}_2$ .

### 3. Trap design

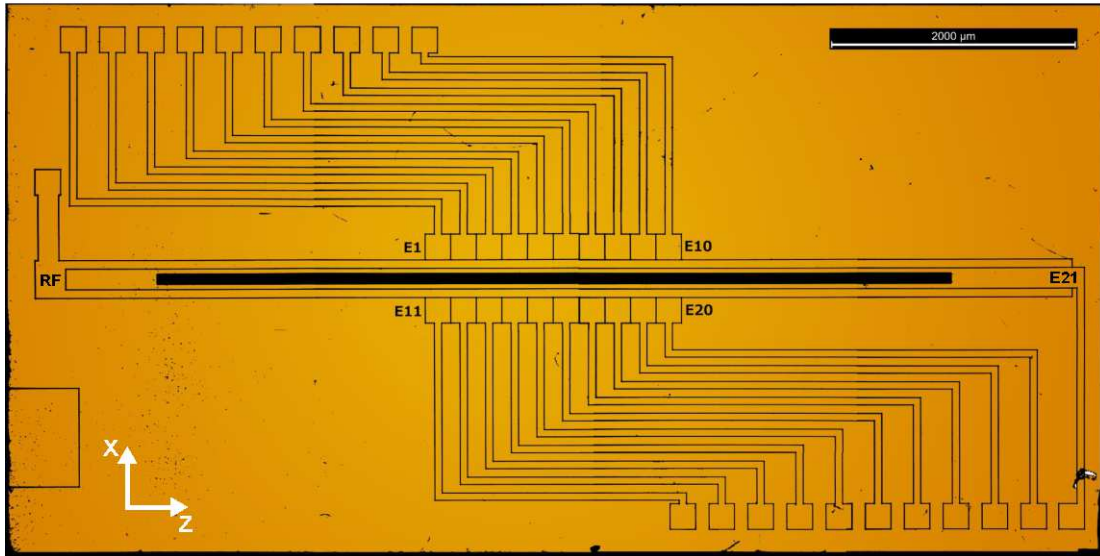


**Figure 3.3.:** Ion trap with slit from Berkeley consisting of 14 Picos taken with a high resolution microscope.

The structure consists of 21 DC electrodes (E1-E21) and one RF electrode (RF), the rest of the surface is grounded. The axes are the same as for the atom trap, where the z-axis indicates the longitudinal direction of the atom cloud. A detailed description of the trap and its properties can be found in [38, 71]. The trap we received has shorts on electrodes 10 and 12 which will not be a problem in our experiments but has to be taken into account.

### 3.4. The atom micro trap

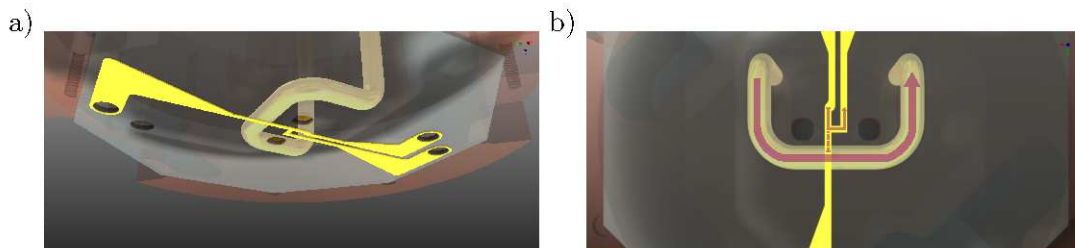


**Figure 3.4.:** Structure of planar atom trap. a) Beneath the surface with the wire structure on it there is a big u-shaped wire we implemented to trap more atoms. b) Illustration of how the current can be sent through the wires. At the top wire we can switch from u- to z-shape by switching the connections.

The wires on the atom trap chip basically have two shapes, an u-shape and a z-shape (see fig. 3.4). To be able to load the trap with as many atoms as possible we plan to form a mirror magneto-optical trap (mMOT - section 3.4.1) which traps and cools atoms in a wide area. By transferring the atoms to another mMOT which is formed by a big u-shaped wire they are confined close to the trap surface. Next the mMOT will be formed by a small u-shaped wire structure on the chip to compress the atom cloud and to couple the atoms to the trap. Finally we aim to switch on the z-shaped wire structure which forms the magnetic trap (section 3.4.2).

### 3.4.1. Mirror magneto-optical trap (mMOT)

As described in section 4.1 we will need four circularly polarized laser beams and a magnetic quadrupole field to form a mMOT. The process which will be used in our setup are illustrated in fig. 3.5.

- 1) A wide quadrupole field is generated by two current carrying coils (section 3.5) in anti-Helmholtz configuration (2-5)mm above the reflecting surface of the chip. For a proper trapping efficiency typically field gradients are chosen to be (10-20)G/cm [43].
- 2) The second step is to turn off the coils while switching on a big u-shaped wire beneath the chip which generates a quadrupole field with a minimum at infinity. This can be raised 2.0 mm above the surface by applying an external homogeneous bias field as described below. The atoms can now be confined right above the chip surface in a spatially smaller area.
- 3) Before we will finally switch to the z-shaped wire a small u-shaped wire on the chip will be used as an intermediate step because it generates a spatially smaller and steeper mMOT volume which compresses the atom cloud further and shifts the atoms close to the trap surface. The setup should allow us to trap  $^{87}\text{Rb}$  atoms which will be evaporated from a dispenser<sup>7</sup> with temperatures of about 750 °C and to cool them down to  $T_D = 140 \mu\text{K}$ . [72]

### 3.4.2. Magnetic trapping of atoms in a planar trap

The interaction energy of an atom with mass  $m$ , magnetic moment  $\boldsymbol{\mu}$  and hyperfine spin  $\boldsymbol{F}$  in a magnetic field is given by

$$U(\mathbf{r}) = -\boldsymbol{\mu} \cdot \mathbf{B}(\mathbf{r}) = \mu_{BF} \mathbf{F} \cdot \mathbf{B}(\mathbf{r}), \quad (3.14)$$

---

<sup>7</sup>SAES, Alkali Metal Dispenser, Rubidium, RB/NF/3.4/12 FT10+10

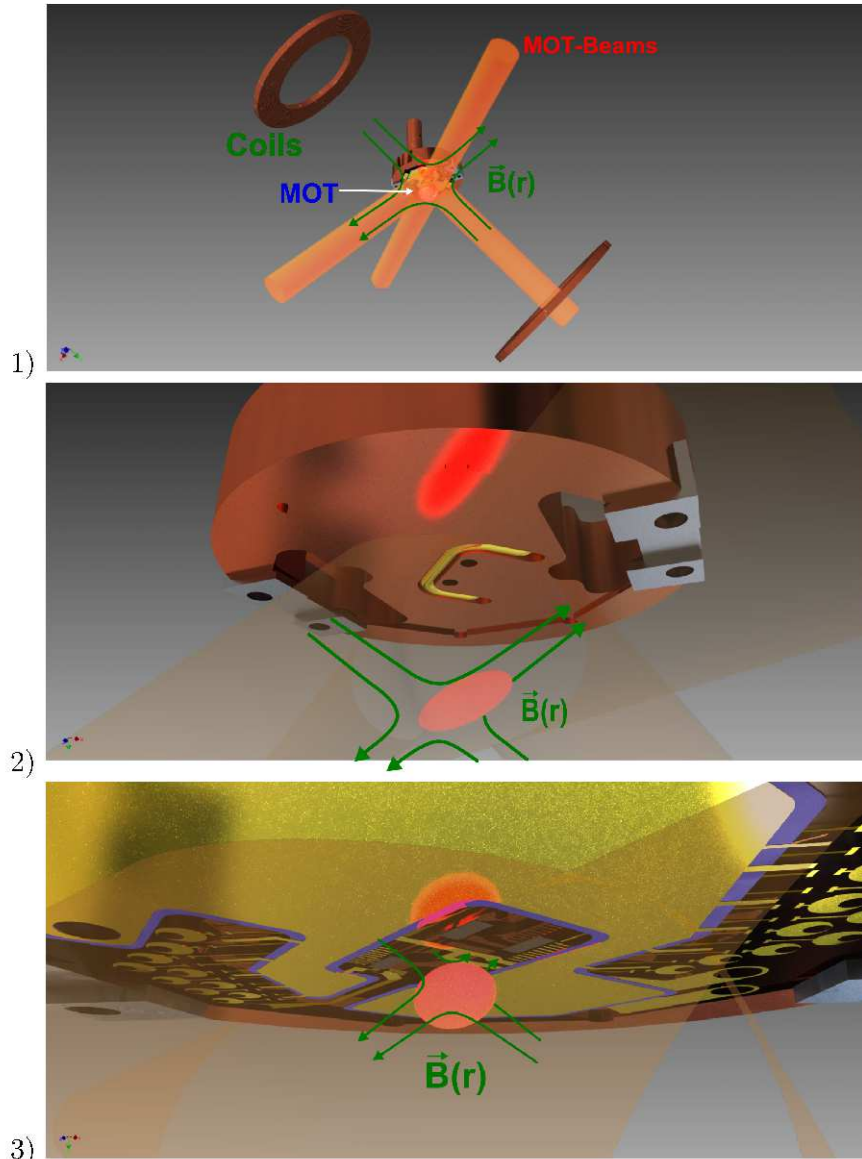


**Figure 3.5.:** 1) A mMOT is formed with four  $\sigma^+$ -polarized light beams (section 4.1 - *Laser cooling*) and a magnetic quadrupole field which is obtained by two current carrying coils in anti-Helmholtz configuration. 2) The magnetic field of a current carrying u-shaped wire beneath the chip superimposed with a homogeneous bias field will provide the quadrupole field for the mMOT. 3) Another u-shaped wire structure on the chip forms a smaller and steeper quadrupole field right above the trap.

where  $\mu_B$  is the Bohr magneton and  $g_F$  is the Landé factor. The spin of an atom in a magnetic field performs *Larmor precession* about the direction of the local field with the frequency

$$\omega_L = g_F \mu_B B(r) / \hbar. \quad (3.15)$$

In an inhomogeneous field it can happen that the spin cannot follow the changing field adiabatically such that *Majorana spin flips* occur which turn a "weak-field-seeking" atom into a non-trappable "strong-field seeking" atom. In the adiabatic limit when the Larmor precession frequency is much higher than the trapping frequency, i.e. when  $\omega_L \gg \omega_{\text{trap}}$ , these *Majorana losses* are prevented and the potential is given by

$$U(\mathbf{r}) = -g_F \mu_B m_F B(\mathbf{r}), \quad (3.16)$$

where  $m_F$  is the magnetic quantum number. For  $^{87}\text{Rb}$  the "weak-field-seeking" magnetically trappable states are  $|F = 2, m_F = 2\rangle$ ,  $|F = 2, m_F = 1\rangle$  and  $|F = 1, m_F = -1\rangle$ . [73, 74]

The principle of a planar atom trap is to form the trapping field with a current carrying wire and an homogeneous bias field as shown in fig. 3.6. The magnetic field of a current carrying *infinitely* long perfect wire can be obtained from *Biot-Savart's law* and is given by

$$B(r) = \frac{\mu_0 I}{2\pi r} \quad (3.17)$$

where  $\mu_0 = 4\pi \times 10^{-7} \text{ Vs/Am}$  is the vacuum permeability and  $r = |\vec{r}|$  is the radial distance to the wire while the direction of the magnetic field is perpendicular to  $\vec{r}$ . To create a field minimum at  $r = r_0$  we apply the external field  $B_{\text{ext}} = -\frac{\mu_0 I}{2\pi r_0}$  which cancels the field at  $r_0$ . In this example the infinite wire (red dot) is aligned at the z-axis pointing out of the plane and it carries a current of 15 A. To form a trapping potential at (0, 0.5, 0)mm we need to apply the field  $\vec{B}_{\text{bias}} = (60, 0, 0)\text{G}$  which is homogeneous and aligned in x-direction. [39]

In the following the magnetic fields of the single wires, their gradients and also the trapping frequencies for the z-shaped wire will be calculated. For the calculations and graphs we used *Wolfram's Mathematica* assuming perfect, infinitely thin wires and for realistic wire calculations we used the add-on *radia*.

### 3. Trap design

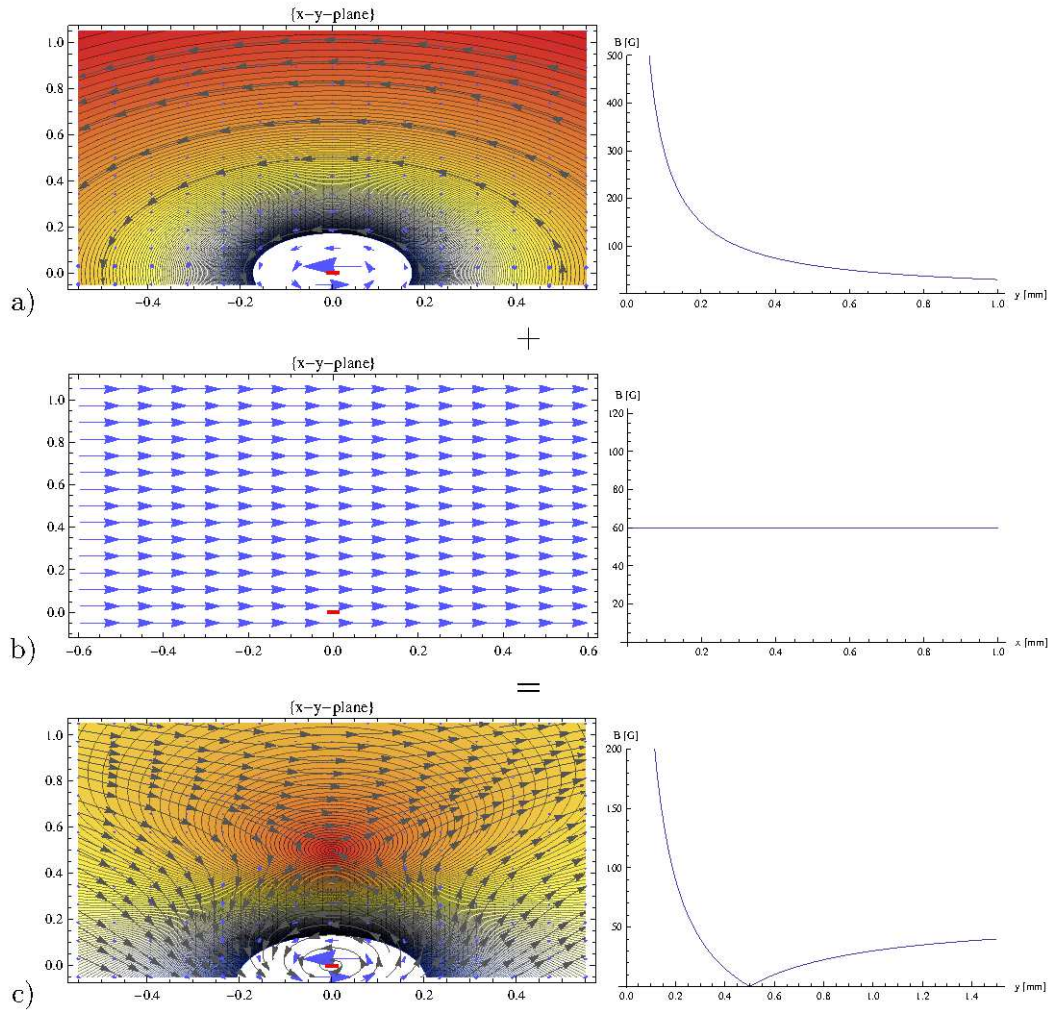


**Figure 3.6.:** Forming a two dimensional trap with a current carrying wire and an homogeneous bias field. a) Field and potential of a infinite current carrying wire on the  $z$ -axis. b) Homogeneous field in  $x$ -direction. c) The resulting field has a minimum at  $(0,0.5,0)$ mm.

### 3.4.3. Magnetic fields due to steady currents in finite perfect wires

The magnetic fields for *finite* perfect wires aligned in x-, y-, or z-direction with the associated lengths  $dx$ ,  $dy$  or  $dz$  are given by

$$\vec{B}_x(x, y, z, dx) = \frac{K}{y^2+z^2} \left( \frac{x+\frac{dx}{2}}{\sqrt{(x+\frac{dx}{2})^2+y^2+z^2}} - \frac{x-\frac{dx}{2}}{\sqrt{(x-\frac{dx}{2})^2+y^2+z^2}} \right) \begin{pmatrix} 0 \\ -z \\ y \end{pmatrix}, \quad (3.18)$$

$$\vec{B}_y(x, y, z, dy) = \frac{K}{x^2+z^2} \left( \frac{y+\frac{dy}{2}}{\sqrt{(y+\frac{dy}{2})^2+z^2+x^2}} - \frac{y-\frac{dy}{2}}{\sqrt{(y-\frac{dy}{2})^2+z^2+x^2}} \right) \begin{pmatrix} z \\ 0 \\ -x \end{pmatrix}, \quad (3.19)$$

$$\vec{B}_z(x, y, z, dz) = \frac{K}{x^2+y^2} \left( \frac{z+\frac{dz}{2}}{\sqrt{(z+\frac{dz}{2})^2+y^2+x^2}} - \frac{z-\frac{dz}{2}}{\sqrt{(z-\frac{dz}{2})^2+y^2+x^2}} \right) \begin{pmatrix} -y \\ x \\ 0 \end{pmatrix}, \quad (3.20)$$

where  $K$  is

$$K = \frac{\mu_0 I}{4\pi 10^{-3}[\text{m}]} = 1\text{G} \quad \text{for } I = 1\text{A}. \quad (3.21)$$

To calculate the desired fields one has to sum every single field:

$$\vec{B}_{\text{wires}} = \sum_j \vec{B}_{D(j)}(x - x_j, y - y_j, z - z_j) \quad (3.22)$$

where  $D(j)$  is the direction of wire  $j$  which is located at  $(x_j, y_j, z_j)$ . We also need to define the bias field that creates a field zero at  $(x_0, y_0, z_0)$

$$\vec{B}_{\text{bias}} = -\vec{B}_{\text{wires}}(x_0, y_0, z_0), \quad (3.23)$$

The total magnetic field is

$$\vec{B}_{\text{total}} = \vec{B}_{\text{wires}}(x, y, z) + \vec{B}_{\text{bias}}, \quad (3.24)$$

and the gradient  $\mathbf{g}$  can now be determined by calculating the derivative of  $\vec{B}_{\text{total}}$

$$\mathbf{g} = \frac{d\vec{B}_{\text{total}}}{d\vec{x}} = (\vec{\nabla} \vec{B}_{\text{total}}). \quad (3.25)$$

This gradient  $\mathbf{g}$  is a  $3 \times 3$  tensor.

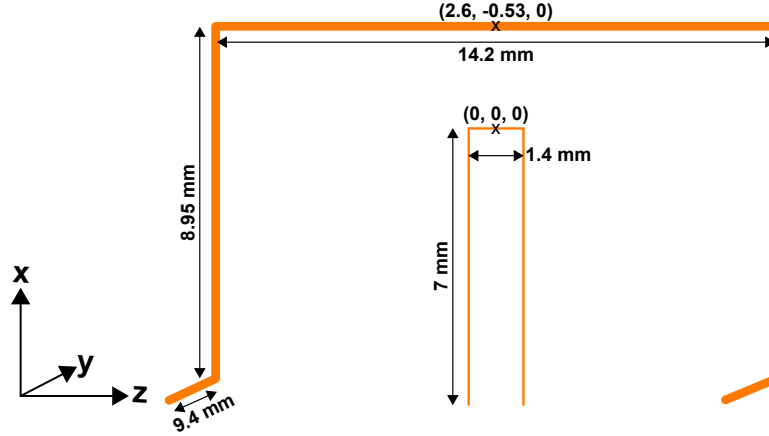


Figure 3.7.: u-shaped wires.

### 3.4.4. Magnetic fields of u-shaped wires

#### Field of big u-shaped wire

The magnetic field of the big u-shaped wire is (all positions and lengths in mm)(fig. 3.7):

$$\begin{aligned} \vec{B}_{\text{big wire}}(x, y, z) = & \vec{B}_z(x - 2.6, y + 0.53, z, 14.2) \\ & + \vec{B}_x(x + 1.9, y + 0.53, z + 7.1, 8.9) - \vec{B}_x(x + 1.9, y + 0.53, z - 7.1, 8.9) \\ & + \vec{B}_y(x + 6.3, y + 9.93, z + 7.1, 9.4) - \vec{B}_y(x + 6.3, y + 9.93, z - 7.1, 9.4) \end{aligned} \quad (3.26)$$

With respect to eq. 3.21 these values are directly proportional to the current we apply. In the following the current in the wires is 15 A. First we calculate the field and the gradient for the big u-wire with a minimum at  $(x_0 = 2.6, y_0 = 2, z_0 = 0)$ mm. The bias field we need to generate is

$$\vec{B}_{\text{bias}} = -\vec{B}_{\text{big wire}}(2.6, 2, 0) = \begin{pmatrix} 10.3 \\ 2.2 \\ 0 \end{pmatrix} \text{G}. \quad (3.27)$$

We can now compute the magnetic field  $\vec{B}_{\text{total}}$  which is shown in fig. 3.8 and the gradient

$$\mathbf{g}(x_0, y_0, z_0) = \begin{pmatrix} -0.1 & 4.7 & 0 \\ 4.8 & 0.2 & 0 \\ 0 & 0 & -0.1 \end{pmatrix} \frac{\text{G}}{\text{mm}}. \quad (3.28)$$

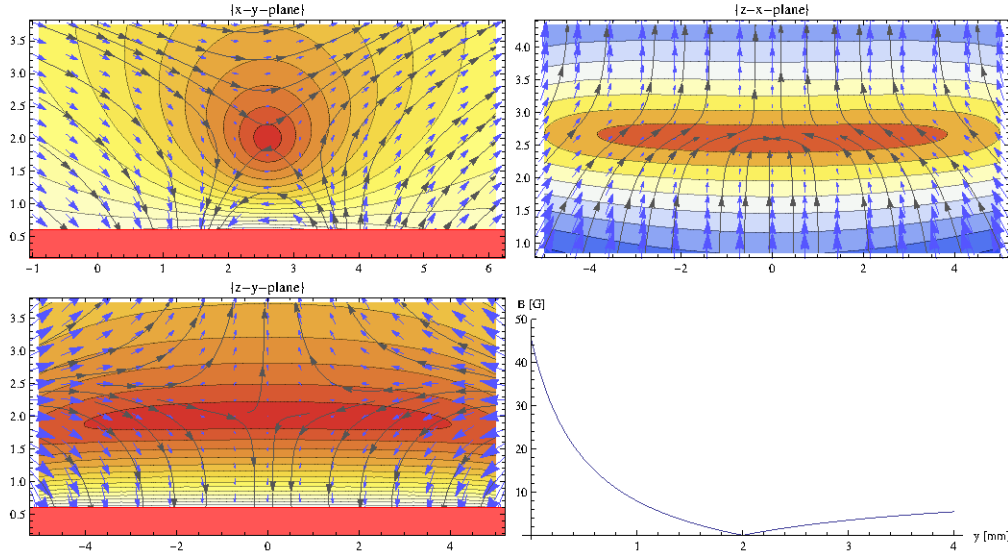


**Figure 3.8.:** B-field of big u-shaped wire in x-y-, z-x- and z-y-plane with the field minimum at  $(x = 2.6 \text{ mm}, y = 2 \text{ mm}, z = 0 \text{ mm})$  and the surface of the ion trap (red). Every colour-step in the contour corresponds to 1 Gauss.

Here it is apparent that the field in the x-y-plane is under an angle of  $45^\circ$  which is required for the mMOT. By diagonalizing it we can find the eigenvalues of the gradient and therefore the steepness of the mMOT.

$$\mathbf{g}_{\text{diag}}(x_0, y_0, z_0) = \begin{pmatrix} 4.8 & 0 & 0 \\ 0 & -4.7 & 0 \\ 0 & 0 & -0.1 \end{pmatrix} \frac{\text{G}}{\text{mm}}. \quad (3.29)$$

### Field of small u-shaped wire

The magnetic field of the small u-shaped wire is:

$$\begin{aligned} \vec{B}_{\text{small wire}}(x, y, z) = & \vec{B}_z(x, y, z, 1.4) \\ & - \vec{B}_x(x + 3.5, y, z - 0.7, 7) + \vec{B}_x(x + 3.5, y, z + 0.7, 7) \end{aligned} \quad (3.30)$$

By switching from the big u-shaped wire to the small one, we will also change the position of the mMOT to where we want to magnetically trap the atoms. The bias field we need to apply to make a trap at  $(x_0 = 0, y_0 = 0.7, z_0 = 0) \text{ mm}$  is

$$\vec{B}_{\text{bias}} = -\vec{B}_{\text{small wire}}(0, 0.7, 0) = \begin{pmatrix} 30.3 \\ 21.2 \\ 0 \end{pmatrix} \text{G}. \quad (3.31)$$

### 3. Trap design

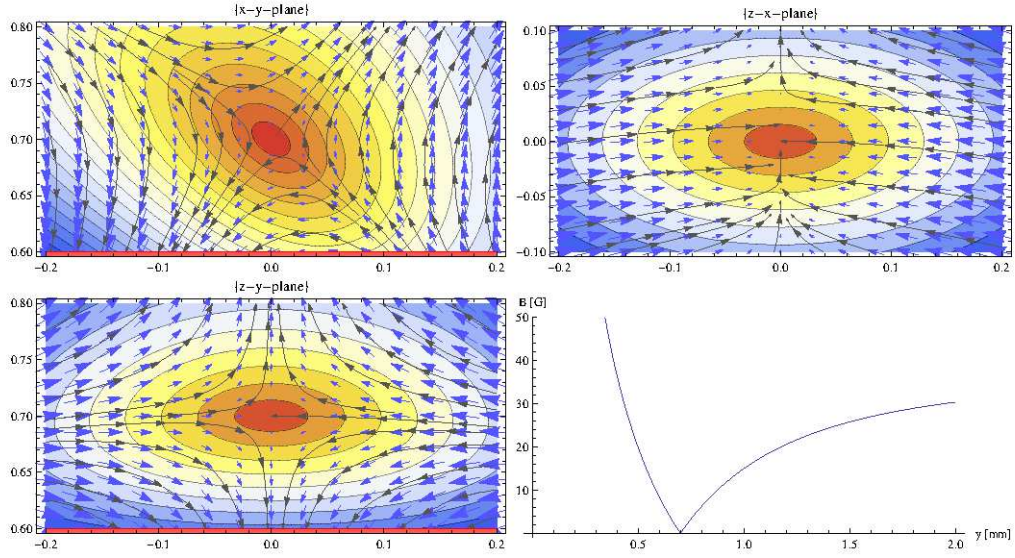


**Figure 3.9.:** B-field of small u-shaped wire in x-y-, z-x- and z-y-plane with the field minimum at  $(x = 0, y = 0.7, z = 0)$ mm and the surface of the ion trap (red). Every colour-step in the contour corresponds to 1 Gauss.

We can now compute the magnetic field  $\vec{B}_{\text{bw,total}}$  which is shown in fig. 3.9 and the gradient

$$\mathbf{g}(x_0, y_0, z_0) = \begin{pmatrix} 0 & 64.9 & 0 \\ 64.9 & 30.6 & 0 \\ 0 & 0 & -30.6 \end{pmatrix} \frac{\text{G}}{\text{mm}} \quad (3.32)$$

with the eigenvalues

$$\mathbf{g}_{\text{diag}}(x_0, y_0, z_0) = \begin{pmatrix} 82.0 & 0 & 0 \\ 0 & -51.4 & 0 \\ 0 & 0 & -30.6 \end{pmatrix} \frac{\text{G}}{\text{mm}}. \quad (3.33)$$

Since  $(10-20)\text{G}/\text{mm}$  is needed for a typical MOT, these values are easily within reach. It is also apparent that this mMOT has a capture volume that is 17 times smaller than the one formed by the big u-shaped wire. That is the reason why this MOT is called a compressed MOT (cMOT) [75].

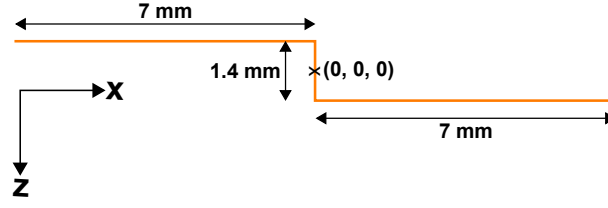
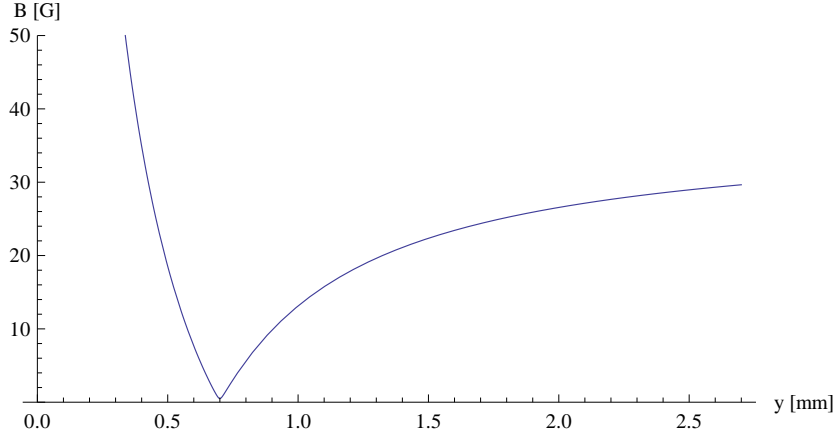


Figure 3.10.: Dimensions of z-shaped wire.


 Figure 3.11.: Ioffe-Pritchard trap potential with non-zero minimum formed by the z-shaped wire and the external fields  $\vec{B}_{zw,bias}(0, 0.7, 0)$ mm and  $\vec{B}_z = (0, 0, 0.5)$ G.

### 3.4.5. z-shaped wire for magnetic trapping

#### Magnetic field of z-shaped wire

The magnetic field of the small z-shaped wire is:

$$\vec{B}_{z\text{-wire}}(x, y, z) = \vec{B}_z(x, y, z, 1.4) + \vec{B}_x(x - 3.5, y, z - 0.7, 7) + \vec{B}_x(x + 3.5, y, z + 0.7, 7) \quad (3.34)$$

The bias field we apply for a field zero-minimum at  $(x_0 = 0, y_0 = 0.7, z_0 = 0)$ mm is

$$\vec{B}_{bias} = -\vec{B}_{z\text{-wire}}(0, 0.7, 0) = \begin{pmatrix} 30.3 \\ 0 \\ -21.2 \end{pmatrix} \text{G}. \quad (3.35)$$

To avoid *Majorana spin flips* we will apply another external field  $\vec{B}_z$  in the direction of the trapping wire to raise the minimum of the field to non-zero and with respect to eq. 3.15 to achieve the adiabatic limit [73]. The external field

$$\vec{B}_z = \begin{pmatrix} 0 \\ 0 \\ 0.5 \end{pmatrix} \text{G} \quad (3.36)$$

not only forms a non-zero minimum but we also have to consider that it displaces the minimum to

$$(x_0^* = -7.5 \times 10^{-9}, y_0^* = 0.700035, z_0^* = 5.3 \times 10^{-12})\text{mm}$$

which is at last the centre of our trap. As shown in fig. 3.11 the z-shaped wire and the applied external fields  $\vec{B}_{zw,bias}(0, 0.7, 0)\text{mm}$  and  $\vec{B}_z = (0, 0, 0.5)\text{G}$  form a Ioffe-Pritchard trap with a non-zero minimum [76]. The resulting fields and Potentials are shown in fig. 3.12.

### 3.4.6. Aligning the atoms with the ion trap

Since the magnetic field of a z-shaped wire is not always symmetric to the x-axis, the axial direction of an atom cloud trapped in this field does not necessarily need to be parallel to the z-axis. The angle between both axes is given by [77]:

$$\theta = -\arctan\left(\frac{\cos(2\xi)\sec(\xi)}{2 + \cot^2(\xi)}\right) \quad (3.37)$$

with  $\xi = \arctan(2 \cdot y_0/s)$ , where  $s$  is the length of the z-shaped wire in z-direction. As a result the length  $s$  needs to be 1.4 mm for an angle of zero (see fig. 3.13) which is exactly the case when the corresponding eigenvector is  $\vec{v}(0) = (0, 0, 1)^T$ .

The gradients are:

$$\mathbf{g}(x_0^*, y_0^*, z_0^*) = \begin{pmatrix} 0 & 64.9 & 0 \\ 64.9 & 0 & -0.3 \\ 0 & 0.3 & 0 \end{pmatrix} \frac{\text{G}}{\text{mm}}. \quad (3.38)$$

As we can see, also a z-shaped wire forms a field which is in the x-y-plane under an angle of 45°. The corresponding eigenvectors are:

$$\vec{v}(64.9) \approx \frac{1}{\sqrt{2}} \begin{pmatrix} 1 \\ 1 \\ 0 \end{pmatrix}, \quad \vec{v}(-64.9) \approx \frac{1}{\sqrt{2}} \begin{pmatrix} 1 \\ -1 \\ 0 \end{pmatrix} \quad \text{and} \quad \vec{v}(0) \approx \begin{pmatrix} 0 \\ 0 \\ 1 \end{pmatrix}. \quad (3.39)$$

As explained in section 3.4.6 the eigenvector for the zero eigenvalue determines the direction of the trapped atom cloud which is in this case exactly in the z-direction.

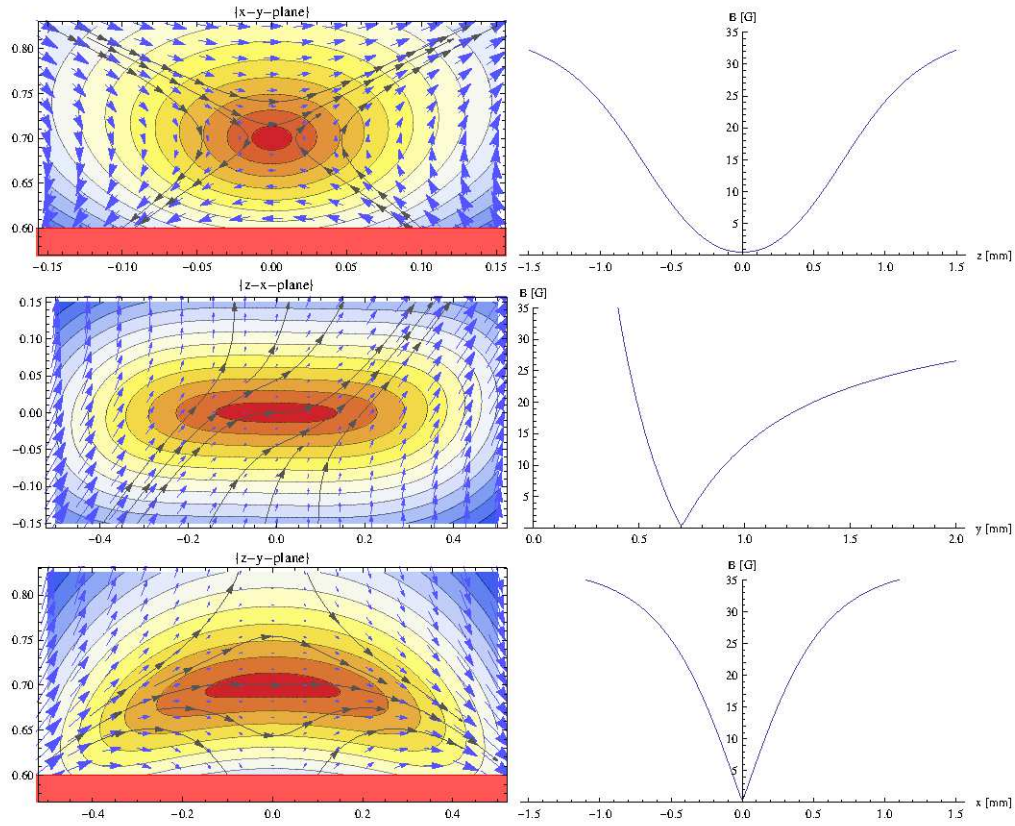


**Figure 3.12.:** B-fields and potentials of z-shaped wire in x-y-, z-x- and z-y-plane with the field minimum at  $(x_0^* = -7.5 \times 10^{-9} \text{ mm}, y_0^* = 0.700\,035 \text{ mm}, z_0^* = 5.3 \times 10^{-12} \text{ mm})$  and the surface of the ion trap (red). Every colour-step in the contour corresponds to 1 Gauss.

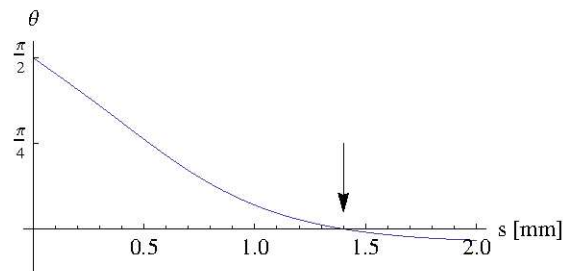


**Figure 3.13.:** Angle  $\theta$  between the z-axis and the axial direction of the atom trap potential in dependency to the length  $s$  of the z-shaped wire in z-direction for a trapping height of  $y_0 = 0.7 \text{ mm}$  above the wire. For  $\theta = 0$  both directions are parallel.

The eigenvalues are

$$\mathbf{g}_{\text{diag}}(x_0^*, y_0^*, z_0^*) = \begin{pmatrix} 64.9 & 0 & 0 \\ 0 & -64.9 & 0 \\ 0 & 0 & 0 \end{pmatrix} \frac{\text{G}}{\text{mm}}, \quad (3.40)$$

### Magnetic field and trap depth using *radia*

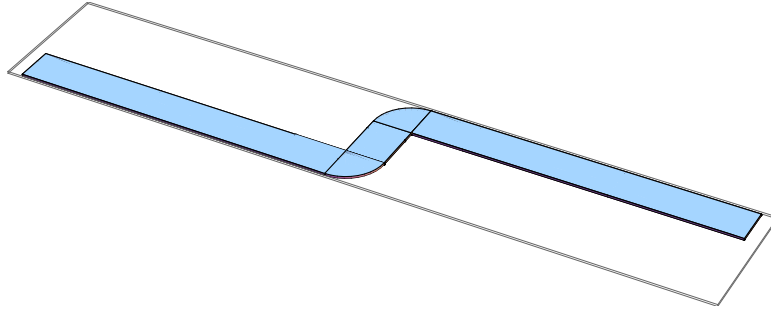


**Figure 3.14.:** Design in *radia* for simulating the z-shaped wire.

A z-shaped wire model constructed in *radia* is presented in fig. 3.14. The wire has an height of 0.08 mm and a width of 0.6 mm. With this model we are able to numerically calculate the magnetic fields of realistic wires. The magnetic potentials of a realistic z-wire by *radia* (dashed) and of a perfect finite wire (solid) are plotted in fig. 3.15. Here we can see quite clearly that the deviations of the potentials due the dimensions of the wire in contrast to the potentials of a perfect finite wire are detectable but relatively small such we can work with the predictions made with the perfect finite wire approximation.

The trap depth is given by the bias field, and the gradients and curvatures of the magnetic field from the wire. Due to the external field the trap depth is determined with eq. 3.16 and  $E_{\text{th}} = k_B T$  to 2.3 mK. But since the trapping region is limited by the surface of the ion trap at  $y = 0.6$  mm the real trap depth will be 273  $\mu\text{K}$ . The temperature we want to reach is in the low  $\mu\text{K}$ -regime such that the trap depth will be no limiting factor in our experiment [78].

### Trapping frequencies

For analysing trap properties like the trapping frequencies it is necessary to calculate the gradient  $\mathbf{g}$  (eq. 3.38) as well as the curvature  $\mathbf{c} = \nabla \mathbf{g}$  which are  $3 \times 3$  and accordingly  $3 \times 3 \times 3$  tensors. We can also define the trap tensor which is given by [77]:

$$\mathbf{t}(x, y, z) = \mathbf{B}(x, y, z) \cdot \mathbf{c}(x, y, z) + \mathbf{g}(x, y, z) \cdot \mathbf{g}(x, y, z) \quad (3.41)$$

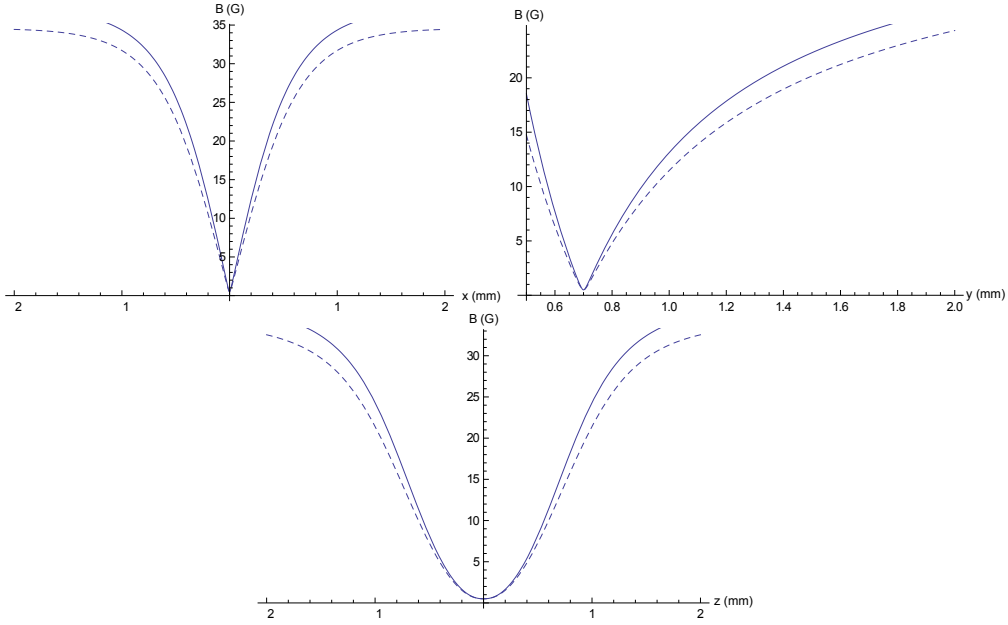


**Figure 3.15.:** Magnetic potentials of z-wire by *radia* (dashed) and with perfect finite wire approximation (solid) for  $I = 15$  A and a trapping height of  $y_0 = 0.7$  mm.

The eigenvalues of  $\mathbf{t}(x, y, z)$ ,  $T_n$  ( $n = 1, 2, 3$ ) are:

$$\vec{T} = \begin{pmatrix} 4212.60 \\ 4189.79 \\ 21.85 \end{pmatrix} \frac{\text{G}^2}{\text{mm}^2} \quad (3.42)$$

and the trap frequencies in Hz can now be obtained with:

$$\nu_n = \frac{1}{2\pi} \sqrt{\frac{10^2 g_F m_F \mu_B}{m}} \sqrt{\frac{T_n}{|\mathbf{B}(x_0^*, y_0^*, z_0^*)|}} \quad (3.43)$$

For our trap they are:

$$\vec{\nu} = \begin{pmatrix} 1170.66 \\ 1167.49 \\ 84.30 \end{pmatrix} \text{Hz} \quad (3.44)$$

### Spatially resolved atom-ion interactions

One of the main tasks of this experiment is to resolve the interaction of atoms with ions caused by an induced dipole moment. As explained in chapter 2 it is useful to define a characteristic range of the interaction which is given by the length scale  $R^* = \sqrt{2C_4/\hbar^2}$ . For resolving the interaction the atomic wave packet size  $l_a = \sqrt{\hbar/m_a\omega_a}$  needs to be in

### 3. Trap design

---

the same range as  $R^*$ . For  $^{171}\text{Yb}^+$  and  $^{87}\text{Rb}$  we get  $R^* = 306$  nm and therefore a required trap frequency of  $\nu^* = 1235$  Hz. Compared to the trapping frequencies received in eq. 3.44 this is very close to what we will achieve using a current of 15 A. The corresponding single atom wave packet sizes are:

$$l_a = \begin{pmatrix} 315, 25 \\ 315, 67 \\ 1174, 76 \end{pmatrix} \text{ nm} \quad (3.45)$$

This calculation is based on the infinity thin wire model. We note that the finite size of the wires slightly reduces the frequency.

#### Ion strings and atoms

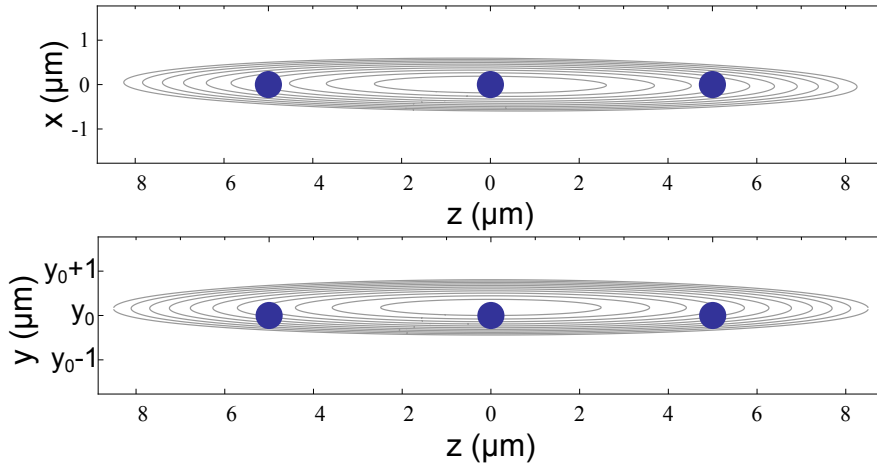


**Figure 3.16.:** Two-dimensional potential contour plot. The contours are 10 nK apart, the outer contour corresponds to 100 nK, which is the chemical potential of about 1200 atoms in the mean field approximation. Also shown is an ion string with equidistant spacing of 5  $\mu\text{m}$ . The ion radius is set to  $R^* = 306$  nm.

We can try and find out what geometry of atoms and ions our setup can realise using mean field theory. In this example the ions are 5  $\mu\text{m}$  apart and their size corresponds to the atom-ion interaction range  $R^* = 306$  nm (see fig. 3.16). The contours of the potential are 10 nK apart such that the outer contour corresponds to 100 nK. This is the chemical potential of about 1200 atoms in the mean field approximation. Due to gravity (1.52 G/mm) the ions are a bit displaced. In the experiment we will have to compensate this effect.

### 3.4.7. Production: thick film technology

The production of the chip is done by Mr. Gebauer who is part of the research group of Prof. Wunderlich (quantum optics) at the physics faculty in Siegen. They use thick film technology to print UHV<sup>8</sup>-compatible, sub-mm-scaled electrical circuits on a substrate which is typically alumina ( $\text{Al}_2\text{O}_3$ ). A major benefit of using this technology is the possibility of printing multiple circuit layers separated by isolating layers which we used for our design. A detailed exposition of this procedure is given in [79].

### 3.4.8. Heating versus material

A technical task while designing the chip is to ensure good heat dissipation between the wires and the heat sink. It has been proven that thermal surfaces generate electromagnetic fields which disturb nearby cold atom clouds. This leads to heating effects which have to be avoided. In addition heating can cause wire destruction and vacuum perturbation caused by an outgassing hot wire. A reasonable heating of the wire where these effects do not increase alarmingly is  $\Delta T \leq 50$  K [80–82]. As illustrated in the following, heating and heat dissipation both strongly depend on the choice of material for the wire and the chip-substrate.

The heating of a current carrying wire of width  $w$  and height  $h$  is caused by its electrical resistance (Joule heating) which can be calculated using Ohm's law  $R = U/I$  with

$$R = j \cdot \rho, \quad (3.46)$$

where  $j = \frac{I}{w \cdot h}$  is the current density and  $\rho$  is the electrical resistivity of the wire material. Due to Joule heating electrical energy is converted to thermal energy which leads to power losses corresponding to the released heat and is given by

$$P = I^2 R. \quad (3.47)$$

The dissipation of heat through a substrate strongly depends on its thermal conductivity  $\lambda$  and heat capacity  $C$ . Following the scheme presented in [83] the expected time-dependent heating of a current carrying wire on a substrate  $\Delta T(t)$  is given by

$$\Delta T(t) = \frac{hw\rho j^2}{2\pi\lambda} \Gamma\left(0, \frac{Cw^2}{4\pi^2\lambda t}\right) \approx \frac{\rho I j}{2\pi\lambda} \ln\left(\frac{4\pi^2\lambda t}{Cw^2}\right) \quad (3.48)$$

where  $\Gamma(a, x) = \int_x^\infty t^{a-1} e^{-t} dt$  is the incomplete gamma function.

As calculated in section 3.4.5 the current for reaching trapping frequencies of 1.2 kHz will be at least 15 A. Due to the building technique described in section 3.4.7 the height of the wire  $h$  is around 60  $\mu\text{m}$  which corresponds to four printed layers. By printing

---

<sup>8</sup>UHV: ultra-high vacuum

### 3. Trap design

---

more layers we run the risk of bubble formation which would ruin the magnetic fields. Also the width  $w$  is limited to  $600\ \mu\text{m}$  to preserve high gradients and specified trapping regions. With respect to eq. 3.48 this leaves us with three degrees of freedom:  $\rho$ ,  $\lambda$  and  $C$  which are material properties of the wire and the substrate. A table of materials which have already been used in thick film technology with properties of matter is listed in table 3.1.

Wire materials	electrical resistivity $\rho$ [n $\Omega$ m]	Substrates	Thermal conductivity $\lambda$ [W/(m K)]	Heat capacity $C$ [J/(m <sup>3</sup> K)]
Au	22.14	Al <sub>2</sub> O <sub>3</sub>	24	$3.024 \times 10^6$
Ag	15.87	AlN	180	$2.4124 \times 10^6$
Pd/Ag	$\approx 32.4$	BeO	330	$3.081 \times 10^6$
		BaTiO <sub>3</sub>	6	$3.172 \times 10^6$

**Table 3.1.:** Material properties

#### Wire material

It is not recommended to use silver (Ag) or palladium/silver (Pd/Ag) alloys due to oxidation effects. So we have decided to use gold (Au).

#### Substrates

Since beryllium oxide (BeO) and barium titanate (BaTiO<sub>3</sub>) are very toxic they should be preferably avoided. Alumina (Al<sub>2</sub>O<sub>3</sub>) is commonly used in thick film technology but also aluminium nitride (AlN) is now being used more often because it has a much higher thermal conductivity. The time-dependent heating of a gold wire on alumina and on aluminium nitride substrates based on eq. 3.48 are compared in fig. 3.17. An initial fast temperature increase ( $\mu\text{s}$  scale) results from a thermal contact resistance between the wire and the substrate and is not covered by eq. 3.48, which only holds for longer time scales. After this increase the temperature rises slowly as seen in table 3.2.

From this it follows that AlN would be a good choice for our setup but since the measurements are in a short time scale also Al<sub>2</sub>O<sub>3</sub> complies our demands.

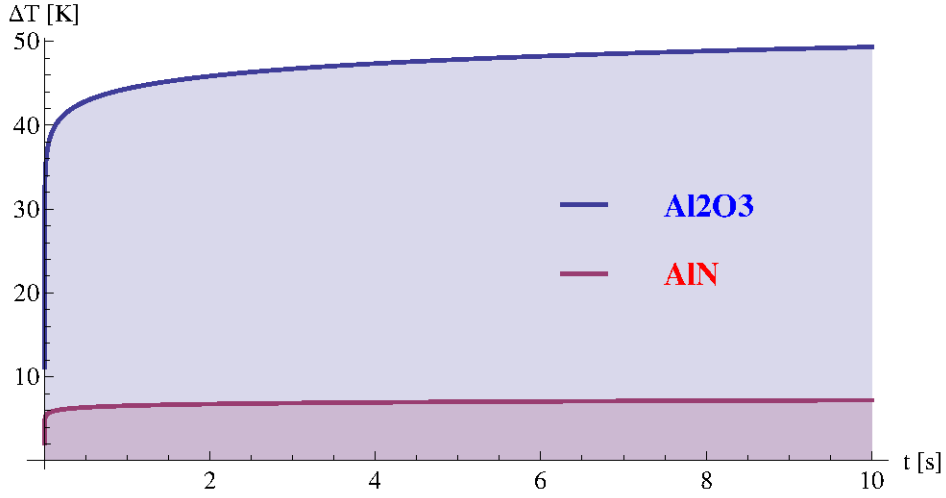


**Figure 3.17.:** Time-dependent heating of gold wire on alumina ( $\text{Al}_2\text{O}_3$ ) or aluminium nitride (AlN) substrates for  $I = 20$  A,  $w = 600$   $\mu\text{m}$  and  $h = 30$   $\mu\text{m}$ .

### Determining the temperature of a wire

In the final experiment it is very difficult to measure the temperature of the wire inside the vacuum chamber. A common method is to measure the temperature-dependent electrical resistivity  $\rho(T)$  of the wire which is given by

$$\rho(T) = \rho_0(1 + \alpha(T - T_0)), \quad (3.49)$$

where  $\rho_{0,\text{Au}} = 2.44 \times 10^{-8} \Omega \text{m}$  is the resistivity at temperature  $T_0 = 20^\circ\text{C}$  and  $\alpha_{\text{Au}} = 0.0034 \text{K}^{-1}$  is the temperature coefficient. Using Ohm's law and  $R = \rho \cdot \frac{l}{h \cdot w}$ , where  $l$ ,  $h$  and  $w$  are the length, height and width of the wire, we can determine the temperature by measuring voltage and current and using:

$$T(U, I) = T_0 - \frac{1}{\alpha} + \frac{hw}{\alpha l \rho_0} \frac{U}{I} \quad (3.50)$$

In fig. 3.18 a) our results from measuring simultaneously voltage and temperature to current of a gold wire with a height of 12-14  $\mu\text{m}$  and a width of  $w = 500$   $\mu\text{m}$  printed on an AlN test-substrate are presented. The temperature increase even at low currents arises from weak thermal contact between the test substrate and an aluminium heat sink. It is useful to plot  $T(U/I)$  which has, with respect to eq. 3.50, a linear relationship. In fig. 3.18 b) the measured results (red dots) and the expected results (black line) are

	Al <sub>2</sub> O <sub>3</sub>	AlN
$\Delta T(1\text{ s})$	44.4 K	6.6 K
$\Delta T(10\text{ s})$	49.3 K	7.2 K
$\Delta T(100\text{ s})$	54.3 K	7.9 K

**Table 3.2.:** Temperature increase of gold wire on alumina (Al<sub>2</sub>O<sub>3</sub>) or aluminium nitride (AlN) substrates for  $t = 1\text{ s}$ ,  $t = 10\text{ s}$  and  $t = 100\text{ s}$  for a current of 15 A.

plotted. Obviously our results do not match the expected values. It seems to us that the gold paste, used for this process, has a much smaller temperature coefficient  $\alpha$  which is approximately  $\alpha = 0.0083\text{ K}^{-1}$  (green, dashed line). Due to this it would be advisable to measure  $\alpha$  once we have received the trap from Siegen.

### 3.4.9. Radio frequency induced adiabatic dressed fields

The realization of a double well potential in our trap will be based on the scheme of adiabatic dressed potentials (ADP). As explained in section 3.4.2, the interaction energy of an atom confined in a static magnetic field  $\mathbf{B}(\mathbf{r})$  is given by eq. 3.14. In the adiabatic limit, where the Larmor frequency  $\omega_L$  is larger than the atomic trap frequencies, this equation simplifies to:

$$U(\mathbf{r}) = -g_F \mu_B m_F B(\mathbf{r}) \quad (3.16)$$

In the presence of a radio frequency (RF) magnetic field  $\mathbf{B}_{\text{RF}}(t)$  the atomic states have avoided crossings at the points where the RF frequency  $\omega_{\text{RF}}$  is in resonance with the frequency difference between the  $m_F$  states. The new interaction energy, experienced by the dressed atoms can be determined as follows:

Following [84] strong coupling is obtained where the static field direction is perpendicular to the direction of the RF field. In the experiment, the RF field will mostly be polarized in the  $y$ -direction as it derives from a coil mounted beneath the trap such that we can write:

$$\mathbf{B}_{\text{RF}}(t) = \hat{e}_y B_{\text{RF}} \cos(\omega_{\text{RF}} t) \quad (3.51)$$

As illustrated in section 3.4.5 the Ioffe-Pritchard field  $\mathbf{B}(\mathbf{r})$  will mostly be pointing in the  $z$ -direction. From this it follows that we have strong coupling. For determining the interaction we define a rotation  $\mathbf{R}$  that rotates any vector into the  $z$ -direction while

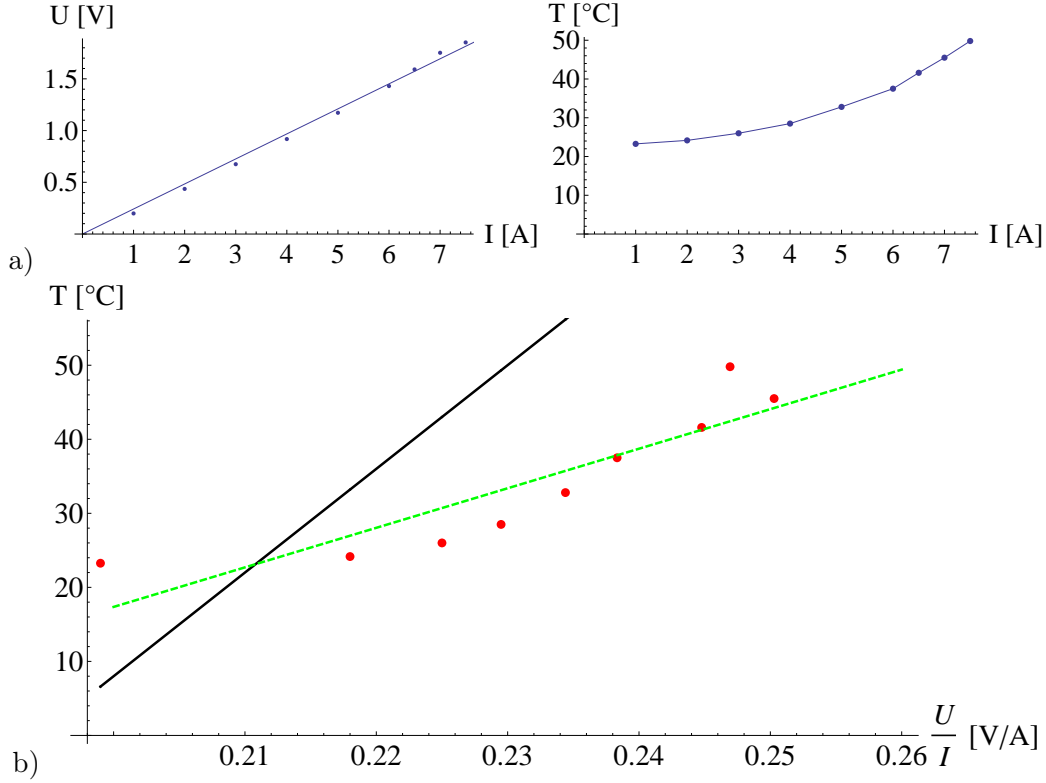


**Figure 3.18.:** a) Self-made test-measurements of  $U(I)$  and  $T(I)$  of a gold wire with ( $l = 30$  mm,  $h = 12 - 14$   $\mu\text{m}$  and  $b = 500$   $\mu\text{m}$ ) on the AlN test-substrate. b)  $T(U/I)$ . Measured results (red dots), expected results (black line) and linear fit to data where  $\alpha = 0.0083$   $\text{K}^{-1}$  (green, dashed line).

keeping its length unchanged. For an arbitrary vector  $(a, b, c)^T$  this rotation is given by [84]:

$$\mathbf{R}(a, b, c) = \begin{pmatrix} \frac{b}{\sqrt{a^2+b^2}} & -\frac{a}{\sqrt{a^2+b^2}} & 0 \\ \frac{ac}{\sqrt{a^2+b^2}\sqrt{a^2+b^2+c^2}} & \frac{bc}{\sqrt{a^2+b^2}\sqrt{a^2+b^2+c^2}} & \frac{\sqrt{a^2+b^2}}{\sqrt{a^2+b^2+c^2}} \\ -\frac{a}{\sqrt{a^2+b^2+c^2}} & -\frac{b}{\sqrt{a^2+b^2+c^2}} & \frac{c}{\sqrt{a^2+b^2+c^2}} \end{pmatrix} \quad (3.52)$$

Using this we can rotate the local static field direction into the  $z$ -direction, such that the new Hamiltonian is given by<sup>9</sup>:

$$H = \mu_B |B(r)| \sigma_z + \mu_B \mathbf{R}(\mathbf{B}(r)) [\hat{e}_y \sigma_y] B_{\text{RF}} \cos(\omega_{\text{RF}} t) \quad (3.53)$$

<sup>9</sup>For simplicity, we consider a two-level system in this section. The theory can be generalised to larger spin systems.

### 3. Trap design

where  $\sigma_i$  for  $i = x, y, z$  are the Pauli matrices. The next step is to transform the Hamiltonian with  $U = e^{i\sigma_z\omega_{\text{RF}}t}$  such that we end up with:

$$U^\dagger H U = \mu_B |B(\mathbf{r})| \sigma_z + \mu_B \vec{p}_- \cdot \mathbf{R}(\mathbf{B}(\mathbf{r})) [\hat{e}_y] B_{\text{RF}} \sigma_y, \quad (3.54)$$

where  $\vec{p}_- = \vec{p}_+^* = (1, -i, 0)^T / \sqrt{2}$  is the unit polarization vector of left handed circularly polarized RF with respect to the z-axis. The transformation of the time derivative in the time-dependent Schrödinger equation is:

$$\left( U^\dagger \left( i\hbar \frac{\partial}{\partial t} U \right) \right) \psi = i\hbar \left( -i\sigma_z \omega_{\text{RF}} + \frac{\partial}{\partial t} \right) \psi \quad (3.55)$$

With these results we are now able to diagonalize the new time-independent Hamiltonian  $\tilde{H} = U^\dagger H U - \hbar\omega_{\text{RF}}\sigma_z$  such that we receive the RF-induced adiabatic dressed potential:

$$\tilde{E} = \pm \sqrt{(\mu_B |B(\mathbf{r})| - \hbar\omega_{\text{RF}})^2 + \hbar^2 \Omega^*(\mathbf{r}) \Omega(\mathbf{r})} \quad (3.56)$$

In this approach we made the *rotating wave approximation* which is valid as long as  $\omega_{\text{RF}} \gg \Omega$ , where  $\hbar\Omega(\mathbf{r}) = \mu_B \vec{p}_- \cdot \mathbf{R}(\mathbf{B}(\mathbf{r})) [\hat{e}_y \sigma_y] B_{\text{RF}}$  is the Rabi frequency, such that terms rotating with  $2\omega_{\text{RF}}$  can be neglected.

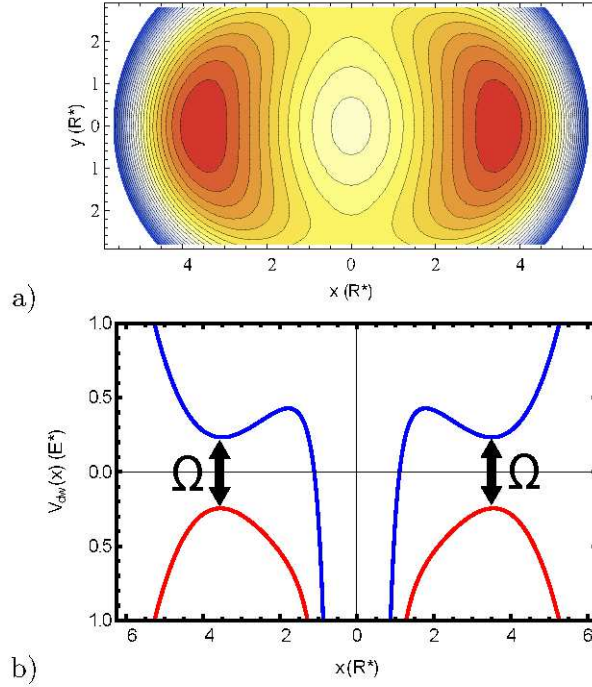


**Figure 3.19.:** a) Example of dressed potentials in the  $x, y$ -plane in units of  $R^*$ .

b) Dressed potential in the  $x$ -direction combined with the atom-ion interaction assuming the ion is trapped at  $x_i = 0$ .

In consideration of the trapping potentials in fig. 3.12 the Ioffe-Pritchard trap has most of its components in the  $z$ -direction but there are also field components in the  $x$ - and  $y$ -direction forming a two-dimensional quadrupole field under an angle of  $45^\circ$ . Taking this into account, for  $\omega_L < \omega_{\text{RF}}$  the resonance condition is met on a two-dimensional closed equipotential surface. The coupling  $\Omega(r)$  however is varying along this surface such that for example in the  $x, z$ -plane with  $z = 0$  the resonance condition is only met on a circle. Since the coupling is strongest where the static field direction is perpendicular to the direction of the RF field which is polarized along the  $y$ -direction, coupling is reduced where the static field points more in this direction (see also fig. 3.12). Accordingly the coupling is affected less where the static field points in the  $x$ -direction. Therefore, two minima occur on the circle where the static field points in the  $z$ -direction such that the trapping potential is split into a double well potential [61, 84–87].

For an external magnetic field of  $B_0 = 0.5 \text{ G}$ , a maximum RF frequency of  $\omega_{\text{RF}}^{\text{max}} = 2\pi \cdot 704.8 \text{ kHz}$  and the Rabi frequency  $\Omega = 2\pi \cdot 70.6 \text{ kHz}$  we get a double well potential that corresponds to the parameters  $q = 3.2 \text{ R}^*$  and  $b = 0.35 \text{ E}^*$  which corresponds to a local trapping frequency of  $\omega_a = 2\pi \cdot 563 \text{ Hz}$  in the  $x$ -direction. These values correspond well to our calculations in chapter 2. The corresponding potential for these values are shown in fig. 3.19. We note that the coil used for generating the dressed potential will also be used for forced evaporative cooling.

## 3.5. Coil design

For the different mirror-MOT stages described in section 3.4.1 we need individual magnetic fields. At the initial stage two coils in anti-Helmholtz configuration are needed to create a quadrupole field with a gradient of  $10 - 20 \text{ G/cm}$  at the trapping region. The following stages (using the u-shaped wires) require homogeneous fields of at least  $30 \text{ G}$  generated by two coils in Helmholtz configuration. Due to the large vacuum chamber we use to ensure optical access the distance between the coils is  $30 \text{ cm}$  such that we will need high currents to reach those field values.

### 3.5.1. Magnetic fields and magnetic field gradients

The magnetic field on the centreline of a current carrying coil with only one winding can be calculated from the Biot-Savart law given by: [88]

$$d\vec{B} = \frac{\mu_0}{4\pi} \frac{I \cdot d\vec{l} \times \hat{r}}{r^2} \quad (3.57)$$

From this equation it follows that the magnetic field on the centreline (z-axis) due to a coil of radius  $R$  carrying a current  $I$  in  $N$  windings at a distance  $z$  is given by:

$$B_z = \frac{\mu_0}{4\pi} \frac{2\pi R^2 I N}{(z^2 + R^2)^{\frac{3}{2}}} \quad (3.58)$$

The field of two coils in anti-Helmholtz configuration can therefore be calculated with:

$$B_z = B_z(z - z_0) - B_z(z + z_0) \quad (3.59)$$

and for two coils in Helmholtz configuration it follows:

$$B_z = B_z(z - z_0) + B_z(z + z_0) \quad (3.60)$$

As can be seen in section 3.6 the distance  $z_0$  from the coils to the trapping region at the middle of the chamber and the mean radius  $R = \frac{1}{2}(R_{\max} + R_{\min})$  of the coils are limited by our setup to  $z_0 = 15$  cm and  $R = 5.5$  cm. The maximum gradient for a fixed distance between the two coils can be calculated using  $R_{\text{opt.}} = \sqrt{(2/3)}z_0$  which is in our case 12.25 cm and which therefore cannot be fulfilled in our setup. Anyway, with these values we get a gradient of:

$$g = \frac{dB_z}{dz} = 0.0016(\text{G/Acm}) I \cdot N \quad (3.61)$$

for anti-Helmholtz configuration and the magnetic field strength of these coils in Helmholtz configuration is given by:

$$B_z = 0.0093(\text{G/A}) I \cdot N \quad (3.62)$$

In fig. 3.20 the design we adopted for our setup is presented. It was originally developed in Prof. Jochim's group *Ultracold Quantum Gases*<sup>10</sup> at the university of Heidelberg and has been adapted in order to fit in our setup. These coils consist of a rectangular (1.5 × 5.0)mm copper wire winded in one single-layer and of an heat sink for water cooling. The great advantage of this design is that we can send very high currents through the coil while keeping the coil radius small which enables us to create strong fields with high gradients. A construction manual for the coils can be found in appendix A.3 [89, 90].

#### 3.5.2. Power loss and heat dissipation

The coil has 14 windings and therefore we will need 435 A to reach 10 G/cm for the quadrupole field in anti-Helmholtz configuration and 230 A for 30 G in Helmholtz configuration. In the following we will analyse the coils for a maximum current of  $I = 435$  A.

---

<sup>10</sup><http://www.lithium6.de/>

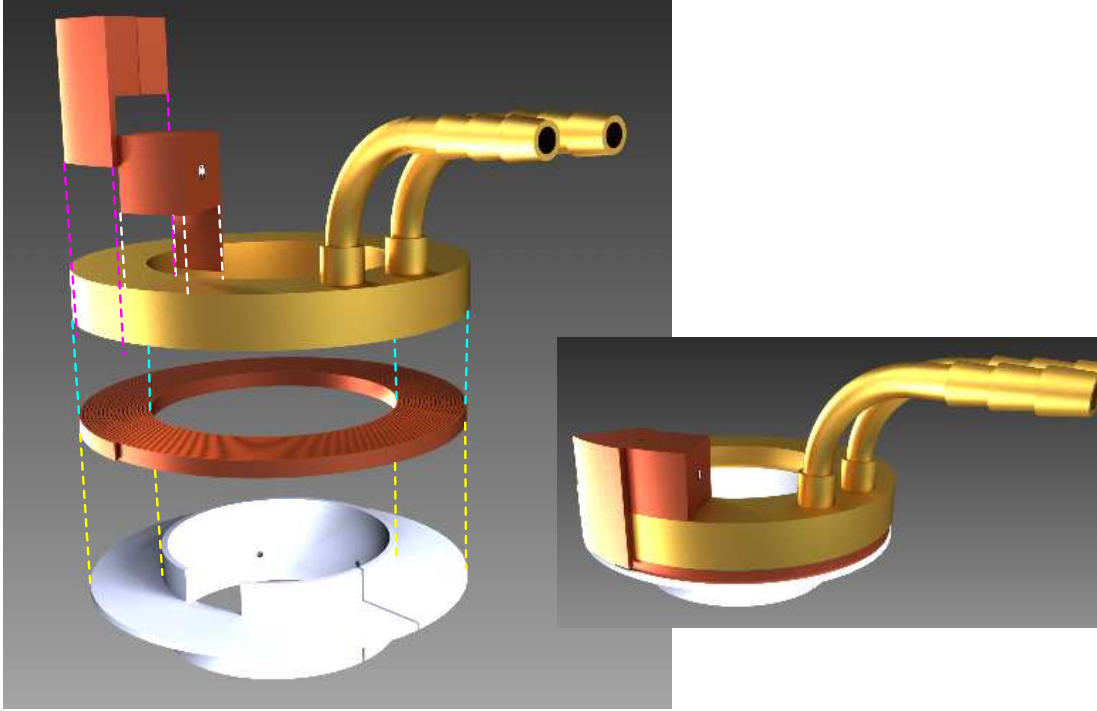


**Figure 3.20.:** Design of coil with 14 windings and heat sink for water cooling.

The heat, generated in the coils due to Joule heating, has to be dissipated continuously with the integrated water cooling system. The power loss of a current carrying wound copper wire with the length  $l = 4.22$  m is

$$P(I) = \rho \frac{l}{hw} I^2 = 1787 \text{ W} \quad (3.63)$$

for  $I = 435$  A,  $h = 5$  mm and  $w = 1.5$  mm, where  $\rho = 16.78 \times 10^{-9} \Omega/\text{m}$  is the electrical resistivity of copper. This is a very high value and therefore the heat dissipation must be brought to an optimum. The voltage drop at each coil is:

$$U = \frac{P}{I} = 4.1 \text{ V} \quad (3.64)$$

It will be a hard match to work with these extreme high currents but since it is technically feasible we are optimistic in getting close to the desired field strengths and gradients.

We are also looking forward to use these coils for our upcoming experiment with Lithium. This is because neutral  ${}^6({}^7)\text{Li}$  atoms require high magnetic field Feshbach resonances. The field for reaching the Feshbach resonances are needed for efficient evaporative cooling.

### 3.6. Vacuum Setup

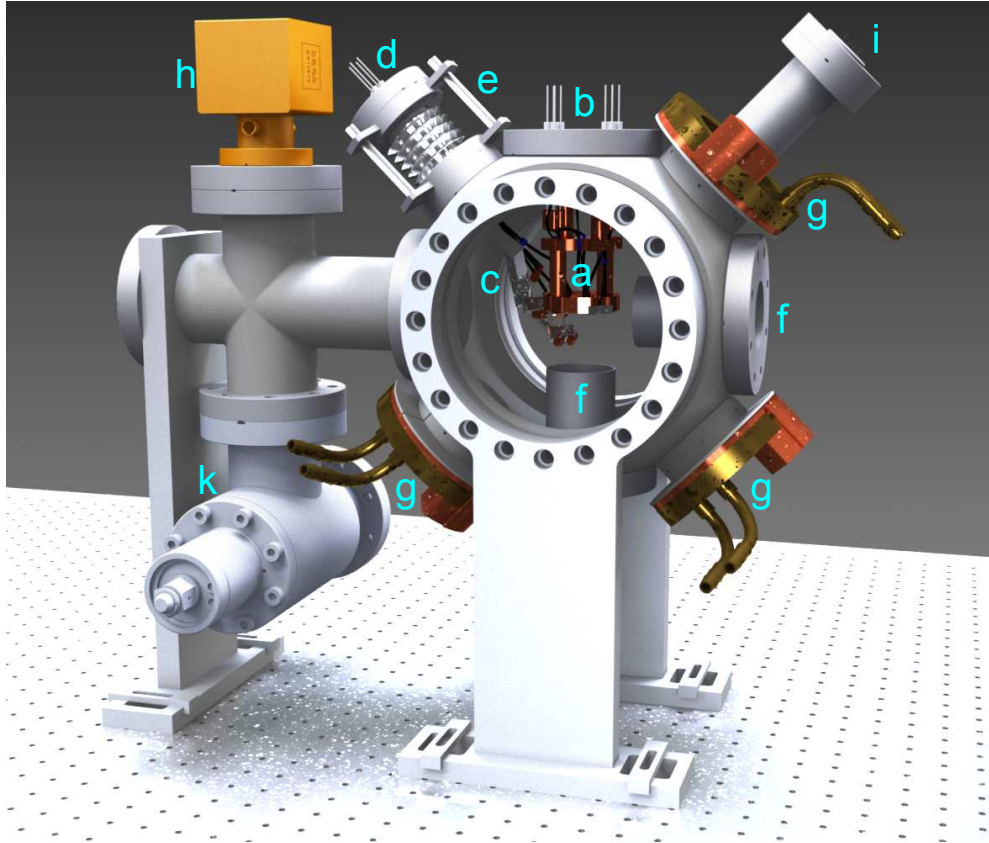


**Figure 3.21.:** Design of vacuum setup: a) Homebuilt carrier for trap and atom dispenser attached on a special CF63 flange (b). c) Homebuilt carrier for ion source and additional atom dispenser attached on a special CF40 flange (d). The height of this mounting relative to the trap can be varied using a weld bellow with adjustment screws (e). f) Inverted viewports for closer imaging of the atoms and the ions. g) Magnetic field coils. h) Vacuum pump. i) Vacuum gauge. k) Valve for pump station.

The design of our vacuum setup is presented in fig. 3.21. The trap is mounted upside-down on a homebuilt carrier (a) (appendix: A.A) which is attached to a special CF63 flange (b) having various electrical feedthroughs<sup>11</sup>. The trap surface is right in the middle of the vacuum chamber<sup>12</sup> which guarantees optimal optical access.

<sup>11</sup>Hositrad: 1x p/n 16802-01-W Sub-D Feedthrough (25-pin), 2x p/n 9216-08-W Pow Feedthrough (4-pin)

<sup>12</sup>Kimball Physics: MCF800M-SphSq-G2E4C4 (metric) - Spherical Square Vacuum Chamber 4x8CF, 4x4.5CF, 4x 2.75CF with Metric-threaded bolt holes throughout

For the neutral Ytterbium oven we designed another carrier (c) (appendix A.A) attached on a special CF40 flange (d) having one high current feedthrough<sup>13</sup> which can be moved using a weld bellow (e) with adjustment screws<sup>14</sup>. Both carriers also include atom dispensers<sup>15</sup> while the one right behind the trap is meant to be the primary atom source and the dispenser at the ion source carrier is only meant to be used if we cannot trap enough atoms this way. Since Rubidium is highly flammable the dispensers have a barrier which is broken through while heating up for the first time. We have seen in other experiments of our group that this carries the risk of polluting the trap surface with parts of this barrier causing shorts. That is why we mounted the primary source behind the trap. Using a movable mounting for the secondary source gives us also the possibility to point the second dispenser away from the trap while heating it up.

For imaging atoms and ions we use inverted viewports (f) to place the optics close to the trap which provides higher resolutions. The homebuilt magnetic field coils (g) (section: 3.5) for the MOT will be attached on CF40 viewports under an angle of 45° to the trap surface (section 3.4.1). To provide ultra-high vacuum (UHV) pressures of at least  $10^{-10}$  mbar we use a non-evaporable getter (NEG) pump<sup>16</sup> (h) which is attached at a special four-way cross right next to the chamber. The pressure will be measured with an ion gauge<sup>17</sup> (i) right next to the trap. The valve (k) is used to attach a pump station typically consisting of a turbo pump and a rotary vane pump to produce the pre-vacuum.

---

<sup>13</sup>1x p/n 9216-08-W Pow Feedthrough (4-pin)

<sup>14</sup>Hositrade: Edge Weld Bellow + Alignment - CF35/SEWB

<sup>15</sup>SAES: 5G0125(\*) - RB/NF/3.4/12 FT10+10

<sup>16</sup>SAES: 5H0170(\*) - NEXTORR D 200 - 5

<sup>17</sup>Agilent Technologies: UHV-24 Ion gauge



# 4

## Laser system

The planned experiments involve neutral Rubidium ( $^{87}\text{Rb}$ ) atoms and Ytterbium ( $^{171}\text{Yb}^+$  or  $^{174}\text{Yb}^+$ ) ions. Therefore, several lasers are required for cooling and imaging. As the lasers for cooling and detecting the ion are still in the planning phase, this chapter will focus the lasers for  $^{87}\text{Rb}$ . We have built our own diode lasers following and improving on the scheme presented in [91] (4.3). A major improvement in output power is achieved by using injection-locking in a master-slave setup (4.2).

### 4.1. Overview

In fig. 4.1 the  $D_1$  and  $D_2$  transitions and the hyperfine structure of  $^{87}\text{Rb}$  are outlined [92]. The laser frequencies that are required for our purposes are indicated on the right hand side. In the following the purpose of all of these is discussed. After that the setup that generates these frequencies will be described.

#### Laser cooling

The laser is frequency stabilized to the  $F = 2 \rightarrow F'' = (1, 3)$  crossover which is located about 18 MHz below the centre of the  $D_2$  transition (4.2.2). To perform laser cooling the light is red detuned by about 6 MHz with respect to the closed  $F = 2 \rightarrow F'' = 3$  transition [93]. This is done using an acousto-optic modulator (AOM)<sup>1</sup> which is driven by a 2 W amplifier<sup>2</sup> and a voltage-controlled oscillator (VCO)<sup>3</sup> (The operation mode of an AOM is illustrated in section 4.2.3).

In fig. 4.2 a scheme of a mirror magneto-optical trap (mMOT) as discussed in section 3.4.1 is shown which traps and cools the atoms close to the trap surface [39]. A mMOT is formed with four circularly polarized<sup>4</sup> beams. Two  $\sigma^+$  beams are counter propagating

---

<sup>1</sup>ISOMET, 1205c-1-869

<sup>2</sup>Mini-Circuits, ZHL-3A+, 29.5 dB m-39.5 dB m (891 mW-8.91 W)

<sup>3</sup>municom, ZX95-100-S+,  $f = 50 - 100$  MHz,  $P_{out} = +10$  dB m, Tune 0.5 to 17 V,  $V_{cc} = 12$  V  
municom, ZX95-200-S+,  $f = 100 - 200$  MHz,  $P_{out} = +10$  dB m, Tune 1 to 17 V,  $V_{cc} = 12$  V

<sup>4</sup>Polarisation with respect to the direction of propagation.



in z-direction and two  $\sigma^+$  beams impinge on the trap surface under an angle of  $45^\circ$  in the x-y-plane. These two beams are reflected into each other while their polarisation switches ( $\sigma^+ \leftrightarrow \sigma^-$ ). This light, together with a magnetic field (green arrows), will generate the MOT [72]. In our experiment the diameters of the light beams will be  $d \approx 2$  cm. For the closed  $F' = 2 \rightarrow F'' = 3$  cycling transition the saturation intensity with  $\sigma^\pm$ -polarized light is  $I_{sat} = 1.669$  mW/cm<sup>2</sup>. From this it follows that at least 22 mW laser power is needed to form the mMOT [92]. The MOT loading and cooling process would take about a few seconds at reasonable Rb pressures.

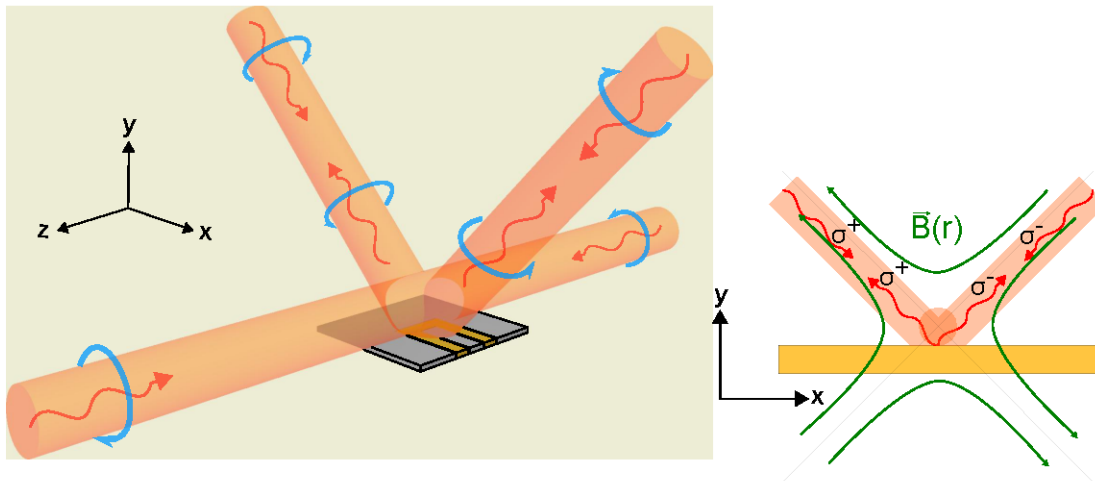


**Figure 4.2.:** Laser beams (red) with circular  $\sigma^\pm$ -polarization (blue) in a mirror MOT with a magnetic field (green).

### repumping

During the optical cooling phase with intense light there is a small probability of 0.1 % for off-resonant scattering into the  $F'' = 2$  state from where the atoms fall into the dark  $F' = 1$  state. Those are pumped back to the  $F'' = 2$  state, by using a *repumper* which in our case is a commercial laser<sup>5</sup> that will be locked to the  $F' = 1 \rightarrow F'' = 2$  transition of the  $D_2$  line, from where they fall back to  $F=2$ . It is also possible to operate the *repumper* at the  $D_1$  transition which has a stronger lock signal and we may upgrade the repumper in the future. Alternatively, the repumper may be locked to a wavemeter<sup>6</sup>.

### optical pumping

The final aim is to trap the atoms magnetically. For this purpose they have to be prepared in a magnetically trappable sub state, i.e.  $|F' = 2, m_F = 2\rangle$ . This is done

<sup>5</sup>Toptica DL 100 Tunable Diode Laser,  $\lambda = 780.2$  nm

<sup>6</sup>HighFinesse Angstrom WS6/200 High Precision - to be acquired

by optical pumping which is illustrated in fig. 4.3.  $\sigma^+$ -polarized light, tuned to the  $F' = 2 \rightarrow F'' = 2$  transition, is irradiated parallel to a homogeneous magnetic field. This field, which defines the quantization axis, is generated by two coils in Helmholtz configuration that we still have to design. The dipole selection rules induced by  $\sigma^+$ -polarized light are:

$$\Delta L = \pm 1 \quad \Delta J = 0, \pm 1 \quad \Delta F' = 0, \pm 1 \quad \Delta m_F = +1 \quad (4.1)$$

Due to the selection rules the magnetic sub state  $m_F$  increases while driving the  $F' = 1 \rightarrow F'' = 2$  transition. Of course we can only control the excitation to the unstable  $F'' = 2$  state. This falls back into the  $F' = 2$  state by emitting a photon of any polarisation and therefore  $\Delta m_F = 0, \pm 1$ . Since the atoms cannot scatter via  $|F' = 3, m_F = 3\rangle$  as this transition is too far detuned they end up in  $|F' = 2, m_F = 2\rangle$  and stop scattering [94, 95].

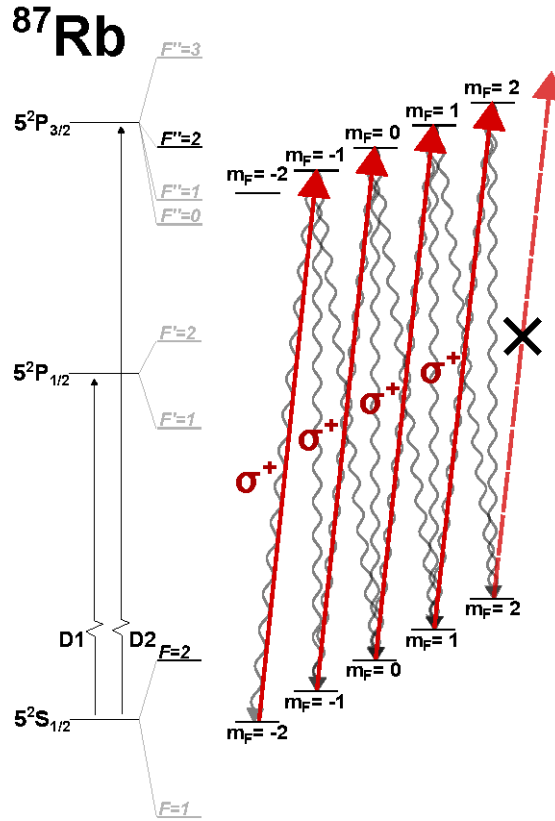


**Figure 4.3.:** Optical pumping with  $\sigma^+$ -polarized light at the closed  $F = 2 \rightarrow F'' = 2$  transition

In our experiment we will use the same laser as for the laser cooling and another AOM to tune the frequency about 55 MHz below the locking point. The repumper (driven within the same intensity range) prevents the atoms from staying in the  $F = 1$  state

during optical pumping. Both beams are circularly polarized by quarter-wave-plates and overlapped with non-polarizing beam splitters. This process typically takes less than a ms.

## Imaging

Imaging the atoms in the MOT is easy because the fluorescence due to the cooling light itself can be imaged. After optical pumping and magnetic trapping there is no fluorescence light to observe. Instead absorption imaging will be used in which a collimated probe beam is sent through the atom cloud. The light is absorbed by the atoms casting a shadow that can be probed with a high-resolution camera. By determining the density distribution we receive information about the atom cloud. A full description concerning absorption imaging of a BEC can be found in [96].

The basic concept is to excite the atoms by driving the resonance below saturation. In this case incoherent scattering can be neglected such that we have only coherent scattering which leaves the ground state unchanged. This can be expressed with

$$\sum_i N_i \langle i | e^{i\Delta\mathbf{k}\mathbf{r}} | i \rangle = \int n(\mathbf{r}) e^{i\Delta\mathbf{k}\mathbf{r}} d\mathbf{r} \quad (4.2)$$

which is the Fourier transformation of the density distribution. From this it follows that for constant scattering without heating the BEC the intensity should not exceed saturation. The absorption is given with the Beer-Lambert Law

$$I(x, z) = I_0 e^{-\sigma_0 d(x, z)} \quad (4.3)$$

where  $\sigma_0$  is the resonant absorption cross section,  $d(x, z) = \int dy n(x, y, z)$  is the projected particle density and  $I_0$  is the initial intensity of the laser beam. This gives us a direct relation between the density of the atom cloud and the absorption

$$d(x, z) = -\frac{1}{\sigma_0} \log \left( \frac{I(x, z)}{I_0} \right) \quad (4.4)$$

which can be obtained from the absorption image.

For the probe beam we will build an additional laser which will be tuned to the closed  $F = 2 \rightarrow F'' = 3$  transition to ensure a strong signal while it has to be driven at an intensity below saturation which is for  $\pi$ -polarized light  $I_{sat} = 2.504 \text{ mW/cm}^2$  with the resonant cross section  $\sigma_0 = 1.937795 \times 10^{-9} \text{ cm}^2$  [92, 96].

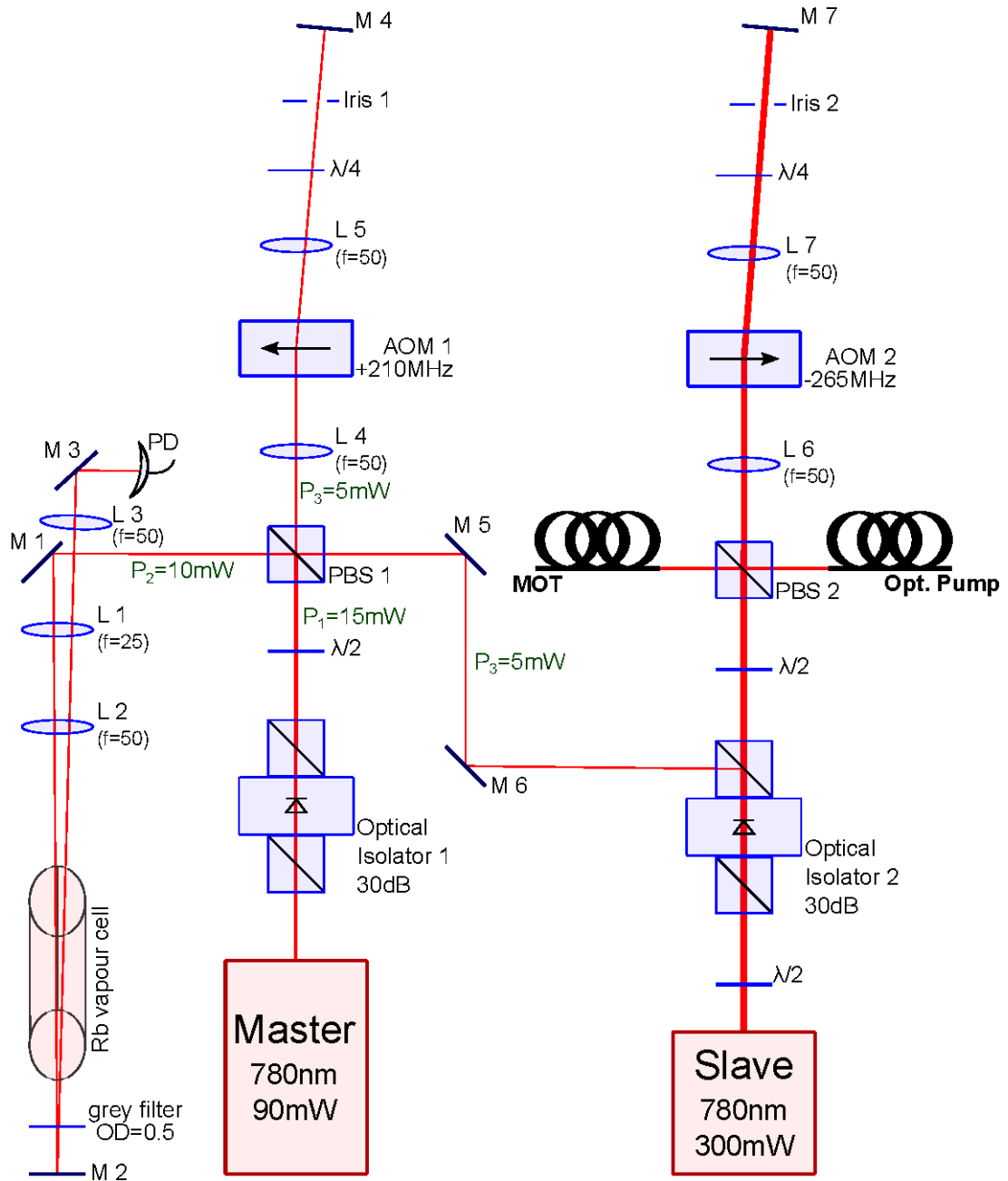


**Figure 4.4.:** Laser setup: Injection-locked master-slave laser system with frequency tuning via acousto-optic modulators (AOMs)

## 4.2. Master-Slave laser setup

In order to have enough power in our laser beams a master-slave system with injection locking as described in section 4.2.4 is the choice for our setup (see fig. 4.4). The master laser beam is sent through an 30 dB optical isolator<sup>7</sup> and a rotatable half-wave plate ( $\lambda/2$ ) before it hits a polarizing beam splitter (PBS) where it gets partially reflected. The particular intensities of the reflected and the transmitted beams depend on the angle of the half-wave plate and can therefore be set by hand.

The reflected light is sent through a Rb vapour cell<sup>8</sup> and is retro-reflected. For Doppler-free saturated absorption spectroscopy (sec.4.2.1) it is detected by a fast photodiode (PD) (sec.4.2.2). Here the locking process takes place which is illustrated in section 4.2.2.

The frequency of the transmitted light is increased by 210 MHz using the acousto-optic modulator AOM 1 (section 4.2.3) and then sent right into the slave laser to induce injection locking (section 4.2.4). The slave laser, which is now operating at the same frequency as the frequency stabilized injected light, is sent through another optical isolator<sup>9</sup> and can be partially used for the MOT and after decreasing the frequency by 265 MHz in AOM 2 for optical pumping.

### 4.2.1. Doppler-free saturated absorption spectroscopy

Usually, the hyperfine structure of <sup>87</sup>Rb is not resolvable due to Doppler broadening of spectral lines which results from the thermal motion of the atoms. The resonance frequency  $\nu_0$  of an atom which moves towards the probe beam with velocity  $v$  is blue shifted while it shifts to the red when the atom moves in the direction of the laser beam. The resulting frequency  $\nu$  is

$$\nu = \nu_0 \left(1 + \frac{v}{c}\right). \quad (4.5)$$

We can assume that the velocities of all atoms in a vapour follow the classical Maxwellian distribution

$$n(v)dv = N \sqrt{\frac{m}{2\pi k_B T}} e^{-\frac{mv^2}{2k_B T}} dv \quad (4.6)$$

which is shown in fig. 4.6.

The full-width-at-half-maximum (FWHM) of this distribution for Doppler broadening is given by

$$\Delta\nu_{FWHM} = \frac{\nu_0}{c} \sqrt{\frac{8k_B T}{m}} \ln 2 = 507 \text{ MHz} \quad (4.7)$$

<sup>7</sup>IOT-5-780-VLP - Free-Space Isolator, 780 nm, Ø4.7 mm Max Beam, 1.7 W Max

<sup>8</sup>Thorlabs, GC25075-RB - Rubidium Pyrex Reference Cell, Ø25 mm x 71.8 mm

<sup>9</sup>LINOS, FI-780-5SV, 780 nm, Ø5 mm aperture

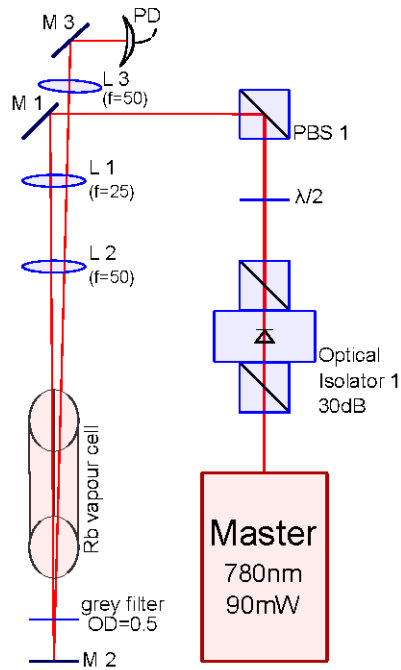


Figure 4.5.: Setup for Doppler-free saturated absorption spectroscopy

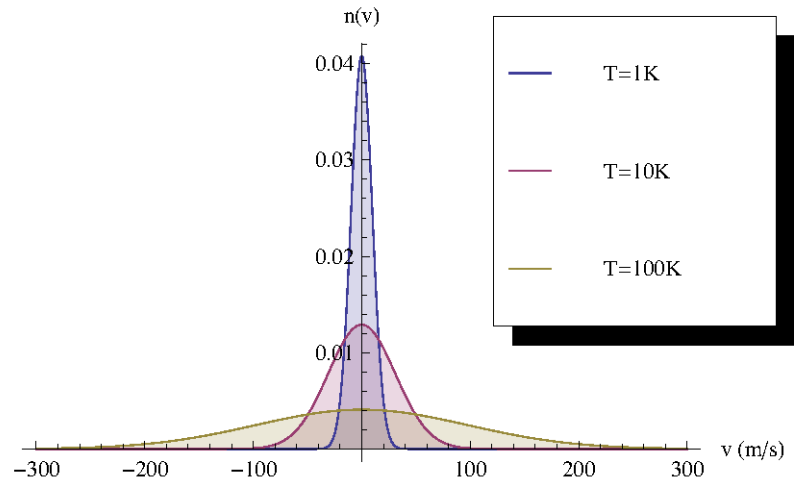
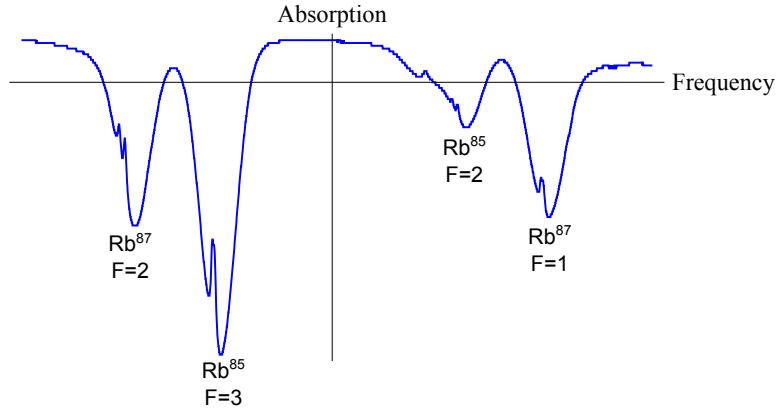


Figure 4.6.: Qualitative Maxwell distribution (eqn. 4.6) of  $^{87}\text{Rb}$  for different temperatures and with  $N = 1$ .

To overcome this we perform saturated absorption spectroscopy as illustrated in fig. 4.5. The cross section of the laser beam is doubled by the two lenses **L1** and **L2** before it is sent through the Rb vapour cell. The neutral density grey filter with an optical density (OD) of 0.5 reduces the intensity of the beam each time by a factor of  $\frac{2}{3}$  such that after being retro-reflected and sent through the filter again the intensity of the light beam has been reduced to a factor of 0.1. The high intense incoming beam is called "pump" beam and the reduced beam is called "probe" beam. This pair of beams is counter propagating through the vapour cell. The pump beam with the frequency  $\nu_i$  excites most of the atoms that have a velocity of

$$v = \frac{c(\nu_i - \nu_0)}{\nu_i} \quad (4.8)$$

such that the lower state is almost empty. Regarding eq. 4.8 and that both beams are counter propagating the probe signal is not affected as long as  $v > 0$ . For  $v = 0$  the gas is nearly transparent for the probe. We therefore receive a sharp dip in the absorption spectrum which is called Lamb dip, i.e. we are able to measure a Doppler free spectrum [97–99]. The Doppler free spectrum obtained in our setup via saturated absorption spectroscopy in a Rb vapour cell is plotted in fig. 4.7.



**Figure 4.7.:** Doppler free spectrum of Rubidium we obtained via saturated absorption spectroscopy in a Rb vapour cell.

In addition to the resonances at frequencies  $\nu_1, \nu_2, \dots, \nu_n$  for  $v = 0$  there are cross-over resonances which occur at frequencies  $\frac{1}{2}(\nu_l + \nu_m)$  where the transitions according to  $\nu_l$  and  $\nu_m$  have the same lower state but two different excited states. With respect to eq. 4.5 the probe and the pump beam can simultaneously be in resonance to these two transitions when  $v \neq 0$ . [97, 100].

In the experimental setup a function generator<sup>10</sup> is used to send a sawtooth voltage signal to a piezo element inside the laser varying the resonator distance (see fig. 4.12).

<sup>10</sup>EXAR, XR-2206

This causes the frequency of the light to slightly oscillate such that we get a derivative signal which has steep zero-crossings at the minimum of every Lamb dip and can be used for the following locking process. The error signal obtained in our setup is shown in fig. 4.8.

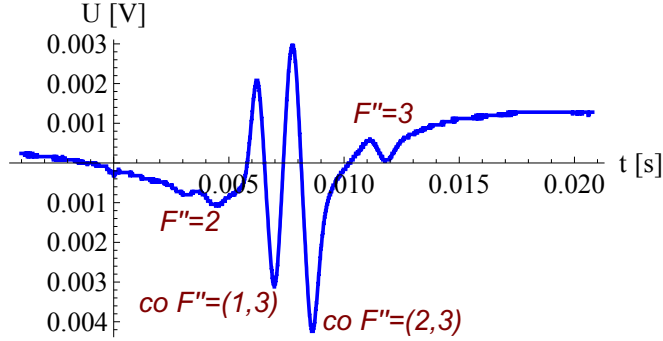


Figure 4.8.: Error signal of  $^{87}\text{Rb}$ .

#### 4.2.2. Frequency modulation lock

As we have seen in section 4.1 we need at least three laser frequencies and multiple beams for laser cooling and detecting  $^{87}\text{Rb}$ . One frequency is for cooling and optical pumping, one is for imaging and one is for repumping. In our case the master laser and the laser for imaging are homebuilt grating stabilized diode lasers (4.3) and the repumper is the commercial Toptica DL100 system.

As illustrated in fig. 4.1 the master laser is frequency stabilized to the  $F = 2 \rightarrow F'' = (1, 3)$  cross-over, the laser for imaging operated at the closed  $F = 2 \rightarrow F'' = 3$  transition and the repumper at the  $F = 1 \rightarrow F'' = 2$  transition. For locking, an error signal is generated out of the Doppler-free saturated absorption spectroscopy signal as described above. This signal is very sensitive to small variations of the laser frequency. The scheme is called frequency modulation (FM) spectroscopy and is fully described in [101].

Technically, we need 2 controllers for FM locking:

##### 1) Pound-Drever driver (PDD)

The Pound-Drever driver (PDD) mainly consists of three elements (see fig. 4.9): A VCO<sup>11</sup>, a phase shifter<sup>12</sup> and a frequency mixer<sup>13</sup>. The VCO provides a RF signal of about 20 MHz which is sent directly into the master laser's RF input to modulate

<sup>11</sup>Mini-Circuits, JTOS-25+, linear tuning 12.5 to 25 MHz

<sup>12</sup>Mini-Circuits, ADE-1+, LO Power +7dBm, 0.5 to 500 MHz

<sup>13</sup>Mini-Circuits, JSPHS-26, 50  $\Omega$ , 18 to 26 MHz, Phase Range 180°

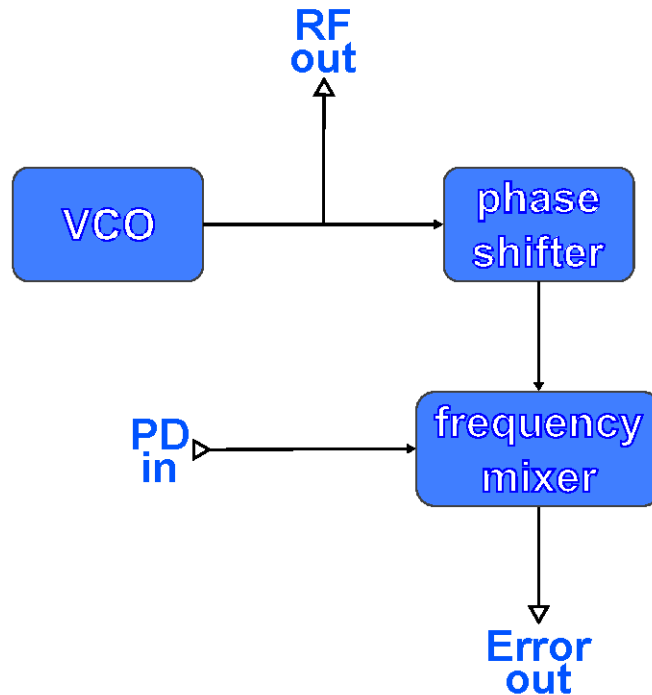


Figure 4.9.: Block diagram of Pound-Drever driver

the diode current via a bias- $t$ . This creates frequency sidebands on the laser. The spectroscopy signal obtained by creating the frequency sidebands is detected by a fast photodiode and fed into the PDD again via the *PD in* where it is mixed with the original phase shifted RF signal to receive the error signal shown in fig. 4.8.

## 2) Lockbox

The lockbox is a PI controller<sup>14</sup> with two channels (see fig. 4.10). The first channel stabilizes the laser frequency via current modulation, the second channel controls a piezo element that changes the grid-diode distance of the laser.

The error signal generated in the PDD is fed into the lockbox via the *error in*. Here the offset of the signal is set to zero and after being inverted it can be observed with an oscilloscope<sup>15</sup>. The signal is split and enters the two channels. The left channel is for locking via current modulation where the controller can be switched from proportional (P) over to proportional and integral (P+I) locking. The right channel is for locking via the piezo element. Here one can switch from proportional over to pure integral locking.

<sup>14</sup>PI: proportional-integral

<sup>15</sup>Tektronix TDS1002B, band with 60 MHz

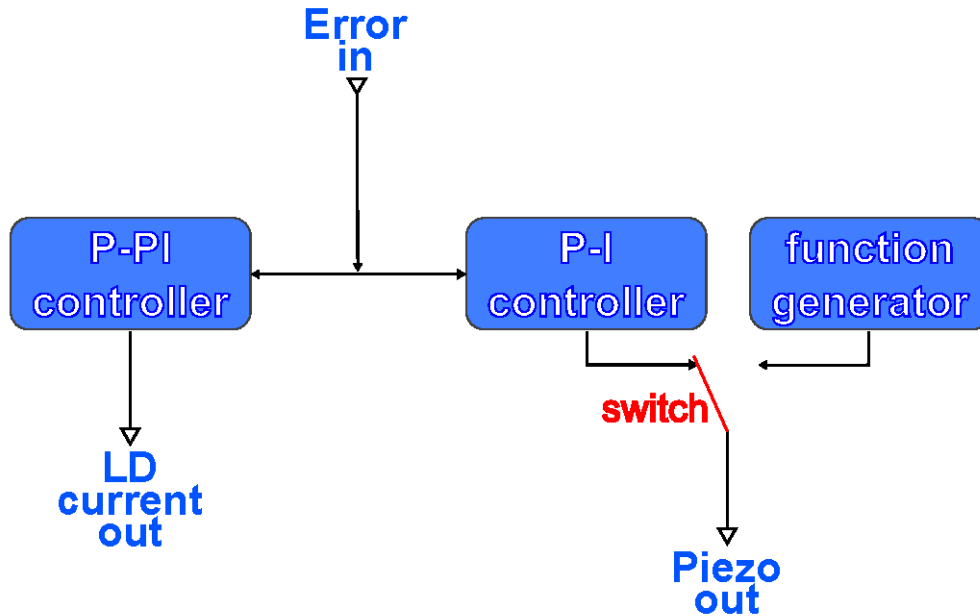


Figure 4.10.: Block diagram of lockbox

The function generator is the one mentioned in section 4.2.1. It generates a sawtooth voltage which is sent to the piezo element varying the laser frequency over a few hundred MHz..

### Fast photodiode (PD)

The measurement of the modulated spectrum poses high demands at the detector. It must be able to detect a wide range of wavelengths with a time resolution of at least 20 MHz. We use an electrical circuit which was developed in our group (fig. A.13). The photodiode<sup>16</sup> itself has a spectral response range of 320-1000 nm and a high-speed response of 10 MHz-2 GHz.

### 4.2.3. Acousto-optic modulator (AOM)

In fig. 4.11 an AOM setup is illustrated. The VCO provides a RF sine-wave output of a frequency which is linearly depending on an applied control voltage. This signal needs to be amplified to be strong enough for the AOM. Here it drives a piezoelectric transducer which generates acoustic wavefronts propagating through a quartz crystal and being absorbed at the other side of it. If light is sent through this crystal it is Bragg diffracted at these wavefronts. That means it depends on the angle of diffraction

<sup>16</sup>Hamamatsu S9055-01

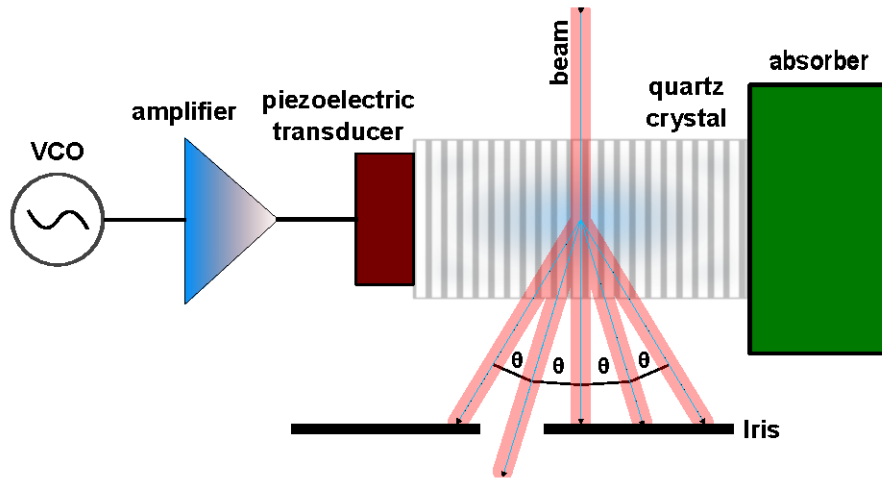


**Figure 4.11.:** AOM setup. An amplified VCO signal drives the AOM where light is diffracted on acoustic wavefronts in a quartz crystal.

whether the diffracted rays interfere constructively or destructively. It can be easily verified that the condition for constructive interference is

$$n\lambda = 2\Lambda \sin \theta, \quad (4.9)$$

where  $n$  is an integer,  $\lambda$  is the optical wavelength,  $\Lambda$  is the acoustic wavelength and  $\theta$  is the diffraction angle. From this it follows that by picking one of the beams using an iris and by varying  $\Lambda$  we can tune  $\lambda$  by a few 100 MHz to a desired value. In our setup (fig.4.4) we built a double pass where the diffracted and separated light beam is back reflected through the AOM where it shifts again such that it is counter-propagating right into the incoming beam. The beams can be separated by using a quarter-wave plate. [102, 103]

#### 4.2.4. Master-Slave injection locking

Injection locking is a type of forced driving. In our case the slave is a free running high-power 300 mW laser diode of particular frequency range and the master is a low-power 90 mW laser which is locked as described in 4.2.2 at a frequency that is within the slave's range. The master laser beam is sent right into the slave via the input port of the optical isolator. If the modes and the wavelengths are in tune the slave adopts these as well as the characteristics of the master like spectral linewidth and stability.

### 4.3. Homebuilt lasers

In order to reduce costs we built the infrared (IR) master and slave lasers ourself. The design for the master we adopted and adapted to our needs is described in [91] and has been used in our group before [104].

#### 4.3.1. Master laser

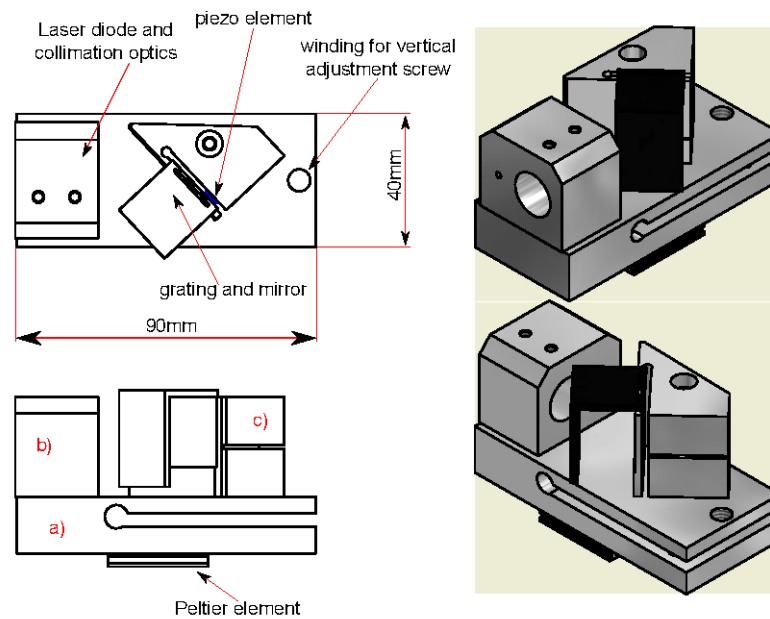


**Figure 4.12.:** Schematic drawing of the master laser.

The master laser setup mainly consists of four parts (see fig. 4.12):

- 1) A big u-shaped block of metal which serves as mount for the other parts and for vertical adjustment of the grating.
- 2) A block for mounting the diode<sup>17</sup> and the collimation tube<sup>18</sup>.
- 3) A rotatable mount for the holographic grating<sup>19</sup> and the mirror.
- 4) A Peltier element<sup>20</sup> for stabilizing the temperature of this setup.

<sup>17</sup>Thorlabs L785P090 - 785 nm, 90 mW, Ø5.6 mm, C Pin Code, Laser Diode

<sup>18</sup>Thorlabs LT110P-B - Collimation Tube with Optic for Ø5.6 and Ø9 mm Laser Diodes,  $f = 6.24$  mm

<sup>19</sup>Thorlabs GH13-18V - VIS Reflective Holographic Grating, 1800/mm, 12.7 mm x 12.7 mm

<sup>20</sup>QuickCool QC-71-1.4-8.5M,  $I_{max} = 8.5$  A,  $U_{max} = 8.6$  V,  $Q_{max} = 40.0$  W,  $\Delta T_{max} = 71$  K

The laser diode is supplied with current by a homebuilt current control which is illustrated in section 4.3.3. It emits light of about 780 nm which is collimated and then sent to the holographic grating. The laser diode and the grating are in Littrow configuration so that only the lowest order  $TEM_{00}$  is coupled out. 20-25 % of the light is coupled back into the diode so that the grating and the diode's rear act as a cavity. One mode of the light is extracted and enters our setup. The output power of the master laser in dependence to the applied current is plotted in fig. 4.13.

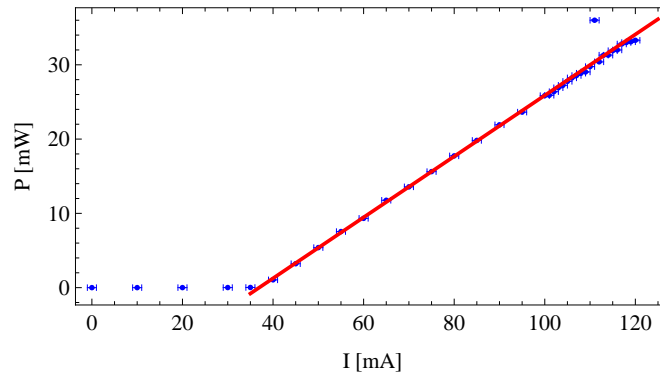


**Figure 4.13.:** Measured output power of master laser in dependence to applied current.

## Adjustment

The adjustment of the laser is crucial and requires some practice. First we need to find the right vertical position of the grating. The laser is run at a power close to the lasing threshold and the horizontal angle is displaced such that one can see two reflections of light on a infrared detection card<sup>21</sup> at the laser output. By turning the vertical adjustment screw both reflections are set to the same height. The horizontal angle can be changed by rotating the whole mount 3) and with another fine adjustment screw right behind the piezo element. The current of the diode is set to 40 mA right below the point where the diode starts to lase. If the grating is brought to the right position such that the beams in the cavity overlap the diode begins to lase even at this low power. Adjusting the wavelength is done with the piezo screw and by varying the current and its value is verified by a wavelength meter<sup>22</sup> and by the fluorescence signal in the Rb vapour cell.

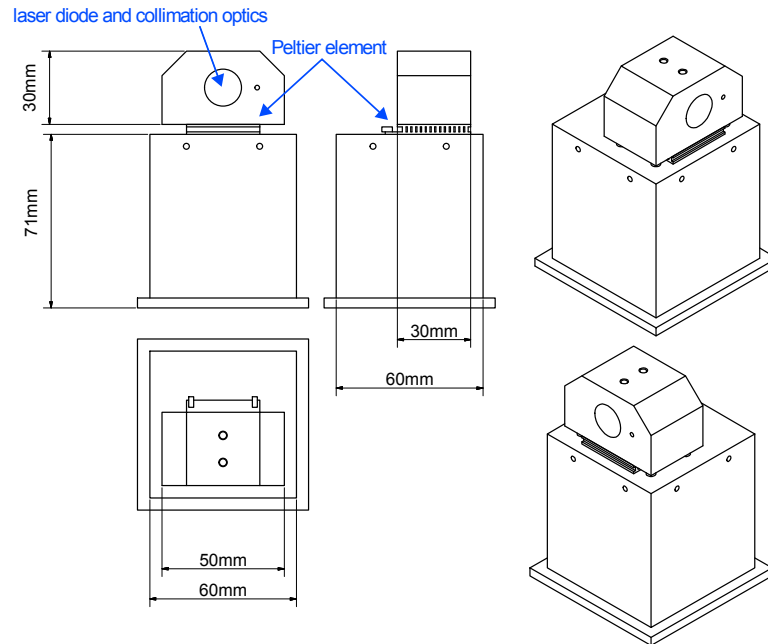


Figure 4.14.: Schematic drawing of the slave laser

### 4.3.2. Slave Laser

Since the *slave* laser only has to provide a free running diode the setup is very simple (fig. 4.14). It only consists of a block for mounting the diode<sup>23</sup> and the collimation tube which is the same as for the *master*. Again the setup is thermally stabilized with a *QuickCool* Peltier element. As mentioned in section 4.1 the wavelengths of the diodes we used so far have ranges that depend on the building technique. As a consequence we sometimes have to cool them down a few K. To avoid water condensation it makes sense to close the whole setup by assembling a glass pane at the outlet and by putting some drying material inside or by filling the whole case with N<sub>2</sub>.

### Adjustment

Realizing the master-slave injection lock bears some problems. The injected *master* beam, which should not have more power than 3 mW, has to be overlapped completely with the beam of the free running *slave*. Once this is done well enough, the *slave* takes over the frequency of the *master*. This can be observed by the fluorescence light in the vapour cell and by using again the wavelength meter which has the advantage that it

<sup>21</sup>Thorlabs VRC5 - IR Detector Card, 700 - 1400 nm

<sup>22</sup>HighFinesse Angstrom WS Ultimate Precision

<sup>23</sup>Thorlabs - LD785-SH300 - 785 nm, 300 mW, Ø9 mm, H Pin Code, Laser Diode

also generates an interference signal. As long as the two beams are not overlapping perfectly the peaks of the signal are split in two. The better the overlapping the closer these peaks get and finally they become one big peak. This can be optimized by reducing the signal of the *master* followed by re-adjusting. In this way the power of the *master* can be reduced to a few hundred  $\mu\text{W}$ .

### 4.3.3. Current control

Since the laser diodes are very easy to damage even at small voltages ( $V_{max} = 2\text{V}$ ) much care has to be taken when building the laser setup. Especially while handling the diodes themselves it is necessary to wear an antistatic wrist strap<sup>24</sup>. Furthermore the current supply for the diodes needs to be built in such a way that no voltage peaks can occur. A very stable current is also needed to grant good stability of the laser frequency.

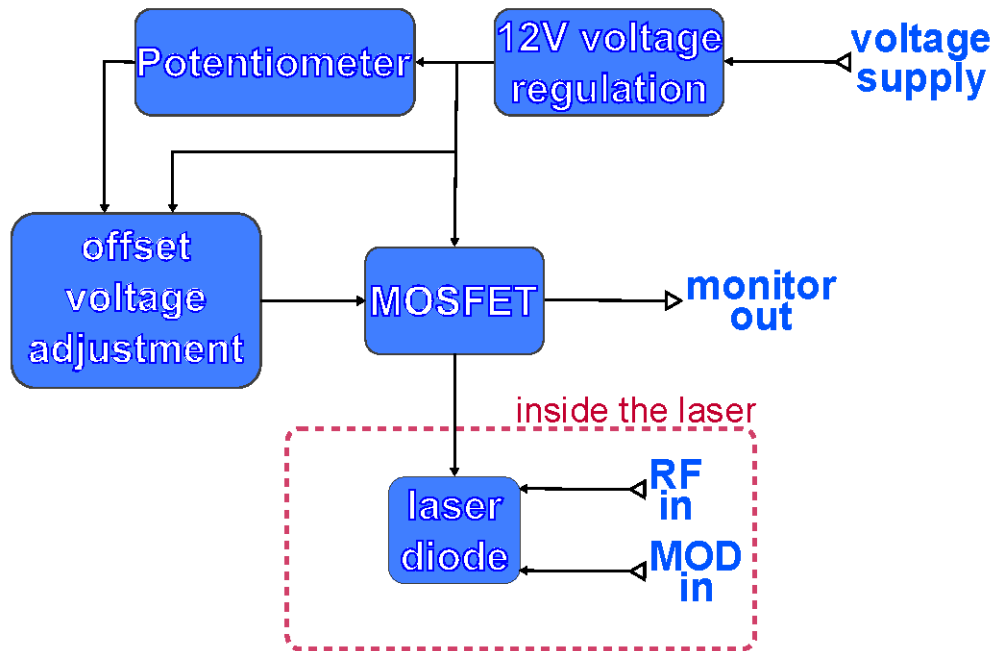


**Figure 4.15.:** Block diagram of current driver for a positive supply.

The current driver is used for all our homebuilt laser systems (see fig. 4.15). A stabilized supply voltage of  $+15\text{V}$  is regulated to  $+12\text{V}$  and sent to a *MOSFET*. Using a potentiometer (P1) and the *LT1028* (IC3) allows us to set an offset voltage by hand which is sent to the *gate*-pin of the *MOSFET* which controls the current flow from the *source*-pin to the *drain*-pin. By changing the voltage at the *gate*-pin the current is

<sup>24</sup>Thorlabs, WS01 - Metal Grounding Wrist Strap with 12 ft Coiled Cord, 5.5" Long

increased or decreased. For monitoring we measure the voltage drop over a resistance of  $1\ \Omega$  before we feed the current into the laser. There are also input connections for the modulation and the RF signal.

#### 4.3.4. Temperature control

In addition to the current the lasers are also very sensitive to small changes of temperature. To hold it stable we use a temperature controller<sup>25</sup> which is shown in 4.16. This temperature controller is connected to the Peltier element in the laser housing. By sending current through this element heat can be transported from its top to its bottom (fig. 4.17) [105]. The circuit has a display that gives a value related to the temperature. You can find a table for the real temperatures in Appendix A.6.

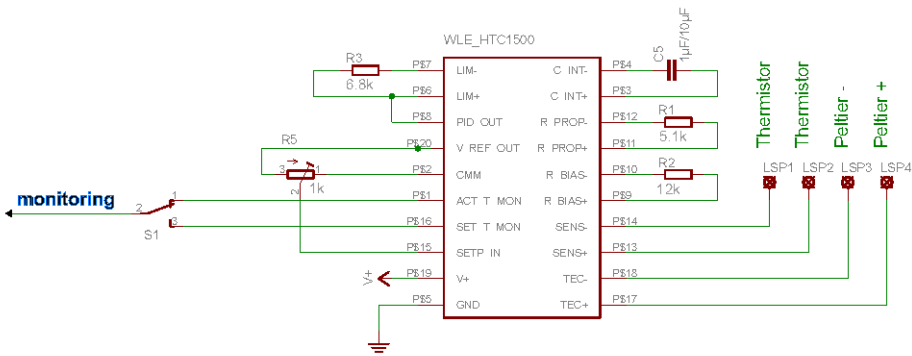
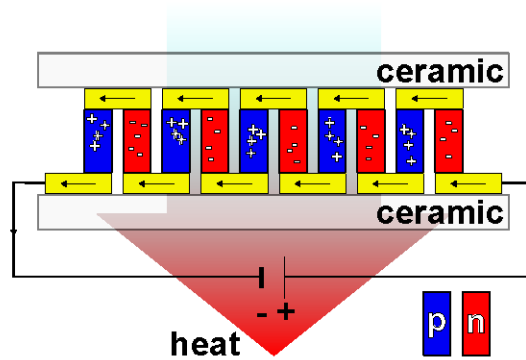


Figure 4.16.: Electrical circuit of the temperature controller

<sup>25</sup>HTC1500 1.5 Amp Temperature Controller,  $\pm 1.5\ \text{A}$



**Figure 4.17.:** Peltier effect: This thermoelectric effect (named after Jean Charles Athanase Peltier) is caused by a heat current that is always part of an electric current. In the p- and n-doped semiconductors the free charge carriers which also carry thermal energy have opposite directions of motion such that in a device like in this figure the heat current always goes from the top to the bottom or by switching the current from the bottom to the top.



# 5

## Outlook

In the first part of this work we investigated theoretically the dynamics of ion controlled atomic Josephson junctions. Here, we started describing the atom-ion interaction while introducing quantum defect theory. This was possible due to the fact that the exact form of the short range interaction does not necessarily need to be known to solve our problem. We have found that in addition to the spin state of the ion also its motion can control the tunnelling rate. The next logical step will be to include the micromotion of the ion in the trap which was neglected so far. This will be part of a subsequent paper.

To enable an experimental implementation of the ion controlled Josephson junction the assembling of the experiment has to be completed. When this is done we will first try to trap ions and atoms while the ions need to be cooled to the ground state. The atoms need to be trapped in a double well potential, formed by radio frequency induced adiabatic dressing, and to be cooled close to about  $1\ \mu\text{K}$  to realize Bose-Einstein condensation.

Future experiments will aim to optimize the trapping parameters and to realize one-dimensional Bose-Einstein condensates. This setup may also give us the opportunity to study many-body phenomena such as self trapping and ion-enabled entanglement and may also allow to observe the physics in ion-perturbed quantum gases.

A future development will be to optimize the trap design by combining both traps on one chip. This will further reduce the distance between the atoms and the wires of the atom chip while increasing the confinement and therefore the trap frequencies. This enhancement would also exclude possible sources of error like the alignment of both traps to each other.





# Appendices

## A.1. Parameters, coordinates and operators used in the calculations

Symbol	Meaning	Definition
$m_i$	mass of ion	
$m_a$	mass of atom	
$\omega_i$	secular trap frequency of ion	$\omega_i = \frac{\gamma\omega_r}{\beta}$
$\omega_a$	trap frequency of atom	$\omega_a = \frac{\omega_r}{\beta}$
$\Omega$	trap drive frequency of Paul trap	$\omega_i \approx \frac{\Omega}{2} \sqrt{a + \frac{q^2}{2}}$
$q$	Paul trap $q$ -parameter, or inter-well distance	
$a$	Paul trap $a$ -parameter	
$r_i$	position of the ion	$r_i = R + r \frac{\mu}{m_i}$
$r_a$	position of the atom	$r_a = R - r \frac{\mu}{m_a}$
$R$	centre-of-mass (com) coordinate	$R = \frac{m_i r_i + m_a r_a}{m_i + m_a}$
$r$	relative coordinate	$r = r_i - r_a$
$p_i$	momentum of the ion	$p_i = p + P \frac{m_i}{M}$
$p_a$	momentum of the atom	$p_a = P \frac{m_a}{M} - p$
$P$	com momentum	$P = p_i + p_a$
$p$	relative momentum	$p = \frac{m_a p_i - m_i p_a}{m_i + m_a}$
$M$	total mass	$M = m_i + m_a$
$\mu$	reduced mass	$\mu = \frac{m_i m_a}{m_i + m_a}$

A. Appendices

---

$C_4$	coefficient for charge-induced dipole interaction	$C_4 = \frac{\alpha_p e^2}{2}$
$\alpha_p$	polarizability of the atom	
$e$	charge of the ion	$e = 1.602176565(35) \cdot 10^{-19} \text{ C}$
$E^*$	energy scale of atom-ion interaction	$E^* = \frac{\hbar^2}{2\mu(R^*)^2}$
$R^*$	range of atom-ion interaction	$R^* = \sqrt{\frac{2\mu C_4}{\hbar^2}}$
$\alpha$	curvature of potential in units $E^*$ and $R^*$	$\alpha = \left(\frac{\hbar\omega_r}{2E^*}\right)^2 = \left(\frac{R^*}{4l_r}\right)^4$
$\alpha_a$	same but with clamped ion (see text)	$\alpha_a = \left(\frac{\hbar\omega_a}{2E^*}\right)^2$
$\omega_R$	com trap frequency	$\omega_R^2 = \frac{m_i\omega_i^2 + m_a\omega_a^2}{M} = B\omega_r^2$
$\omega_r$	relative trap frequency	$\omega_r^2 = \frac{m_i\omega_a^2 + m_a\omega_i^2}{M}$
$\gamma$	ratio between ionic and atomic trap frequency	$\gamma = \frac{\omega_i}{\omega_a}$
$\beta$	ratio between relative and atomic trap frequency	$\beta^2 = \frac{m_i + \gamma^2 m_a}{M}$
$B$	ratio between com and relative trap frequency	$B^2 = \frac{m_a + \gamma^2 m_i}{m_i + \gamma^2 m_a}$
$l_i$	ionic ground state size	$l_i = \sqrt{\frac{\hbar}{2m_i\omega_i}}$
$l_a$	atomic ground state size	$l_a = \sqrt{\frac{\hbar}{2m_a\omega_a}}$
$l_R$	com ground state size	$l_R = \sqrt{\frac{\hbar}{2M\omega_R}} = \alpha^{-1/4} \sqrt{\frac{\mu}{2MB}}$
$l_r$	relative ground state size	$l_r = \sqrt{\frac{\hbar}{2\mu\omega_r}} = \frac{\alpha^{-1/4}}{\sqrt{2}}$
$\hat{R}$	com position operator	$\hat{R} = l_R (a^\dagger + a)$
$\hat{P}$	com momentum operator	$\hat{P} = \frac{1}{2il_R} (a^\dagger - a)$

## A.2. Values of $E^*$ and $R^*$ for various combinations of atoms and ions

Atom	Ion	Mass ratio $\frac{m_i}{m_a}$	$E^*/h$ (kHz)	$E^*/k_B$ ( $\mu$ K)	$R^*$ (nm)	References
<b><sup>6</sup>Li</b>	<sup>174</sup> Yb <sup>+</sup>	28.92	178.583	8.57	69.77	[106]
	<sup>171</sup> Yb <sup>+</sup>	28.42	178.793	8.58	69.75	
	<sup>138</sup> Ba <sup>+</sup>	22.93	181.716	8.72	69.46	
	<sup>88</sup> Sr <sup>+</sup>	14.61	190.459	9.14	68.65	
	<sup>40</sup> Ca <sup>+</sup>	6.64	220.851	10.60	66.16	
	<sup>24</sup> Mg <sup>+</sup>	3.99	261.022	12.53	63.45	
	<sup>9</sup> Be <sup>+</sup>	1.50	463.888	22.26	54.95	
<b><sup>7</sup>Li</b>	<sup>174</sup> Yb <sup>+</sup>	24.79	132.705	6.37	75.15	[107]
	<sup>171</sup> Yb <sup>+</sup>	24.36	132.885	6.38	75.12	
	<sup>138</sup> Ba <sup>+</sup>	19.66	135.407	6.5	74.77	
	<sup>88</sup> Sr <sup>+</sup>	12.53	142.967	6.86	73.76	
	<sup>40</sup> Ca <sup>+</sup>	5.70	169.446	8.13	70.69	
	<sup>24</sup> Mg <sup>+</sup>	3.42	204.838	9.83	67.41	
	<sup>9</sup> Be <sup>+</sup>	1.28	387.835	18.61	57.47	
<b><sup>23</sup>Na</b>	<sup>174</sup> Yb <sup>+</sup>	7.57	14.760	0.708	129.85	[108, 109]
	<sup>171</sup> Yb <sup>+</sup>	7.44	14.820	0.711	129.72	
	<sup>138</sup> Ba <sup>+</sup>	6.00	15.674	0.752	127.92	
	<sup>88</sup> Sr <sup>+</sup>	3.82	18.326	0.879	123.02	
	<sup>40</sup> Ca <sup>+</sup>	1.74	28.575	1.37	110.09	
	<sup>24</sup> Mg <sup>+</sup>	1.04	44.169	2.12	98.73	
<b><sup>39</sup>K</b>	<sup>174</sup> Yb <sup>+</sup>	4.46	3.327	0.160	218.46	[110]
	<sup>171</sup> Yb <sup>+</sup>	4.39	3.348	0.161	218.11	
	<sup>138</sup> Ba <sup>+</sup>	3.54	3.652	0.175	213.42	
	<sup>88</sup> Sr <sup>+</sup>	2.26	4.625	0.221	201.19	
	<sup>40</sup> Ca <sup>+</sup>	1.026	8.661	0.415	171.98	
<b><sup>40</sup>K</b>	<sup>174</sup> Yb <sup>+</sup>	4.35	3.235	0.155	219.24	[111]
	<sup>171</sup> Yb <sup>+</sup>	4.27	3.257	0.156	218.88	
	<sup>138</sup> Ba <sup>+</sup>	3.45	3.559	0.171	214.08	
	<sup>88</sup> Sr <sup>+</sup>	2.20	4.526	0.217	201.59	
	<sup>40</sup> Ca <sup>+</sup>	1.00	8.558	0.411	171.92	
<b><sup>87</sup>Rb</b>	<sup>174</sup> Yb <sup>+</sup>	2.00	0.924	0.044	307.23	[112, 113]
	<sup>171</sup> Yb <sup>+</sup>	1.97	0.935	0.045	306.33	
	<sup>138</sup> Ba <sup>+</sup>	1.59	1.092	0.052	294.67	
	<sup>88</sup> Sr <sup>+</sup>	1.01	1.624	0.078	266.80	

A. Appendices

$^{133}\text{Cs}$	$^{174}\text{Yb}^+$	1.31	0.435	0.021	392.67	[114, 115]
	$^{171}\text{Yb}^+$	1.29	0.442	0.021	391.19	
	$^{138}\text{Ba}^+$	1.04	0.539	0.026	372.18	
$^{172}\text{Yb}$	$^{174}\text{Yb}^+$	1.01	0.917	0.044	252.49	[68]
$^3\text{He}^*$	$^{174}\text{Yb}^+$	57.67	357.285	17.14	69.07	[116]
	$^{171}\text{Yb}^+$	57.68	357.499	17.16	69.06	
	$^{138}\text{Ba}^+$	45.72	360.475	17.30	68.92	
	$^{88}\text{Sr}^+$	29.14	369.304	17.72	68.51	
	$^{40}\text{Ca}^+$	13.25	399.283	19.16	67.18	
	$^{24}\text{Mg}^+$	7.95	437.486	21.00	65.66	
	$^9\text{Be}^+$	2.99	614.929	29.51	60.31	
$^4\text{He}^*$	$^{174}\text{Yb}^+$	43.46	205.130	9.84	79.35	[116]
	$^{171}\text{Yb}^+$	42.71	205.293	9.85	79.34	
	$^{138}\text{Ba}^+$	34.45	207.549	9.96	79.12	
	$^{88}\text{Sr}^+$	21.96	214.262	10.28	78.49	
	$^{40}\text{Ca}^+$	9.98	237.236	11.39	76.52	
	$^{24}\text{Mg}^+$	5.99	266.883	12.81	74.30	
	$^9\text{Be}^+$	2.25	408.774	19.61	66.79	
$^{24}\text{Mg}$	$^{174}\text{Yb}^+$	7.25	31.284	1.50	87.54	[117]
	$^{171}\text{Yb}^+$	7.13	31.417	1.51	87.45	
	$^{138}\text{Ba}^+$	5.75	33.297	1.60	86.19	
	$^{88}\text{Sr}^+$	3.67	39.145	1.88	82.77	
	$^{40}\text{Ca}^+$	1.66	61.868	2.97	73.82	
	$^{24}\text{Mg}^+$	1.00	96.645	4.64	66.03	
$^{40}\text{Ca}$	$^{174}\text{Yb}^+$	4.35	5.553	0.267	167.35	[118]
	$^{171}\text{Yb}^+$	4.28	5.590	0.268	167.08	
	$^{138}\text{Ba}^+$	3.45	6.108	0.293	163.41	
	$^{88}\text{Sr}^+$	2.20	7.769	0.373	153.87	
	$^{40}\text{Ca}^+$	1.00	14.687	0.705	131.23	
$^{52}\text{Cr}$	$^{174}\text{Yb}^+$	3.35	7.912	0.380	126.37	[112]
	$^{171}\text{Yb}^+$	3.29	7.976	0.383	126.12	
	$^{138}\text{Ba}^+$	2.66	8.891	0.427	122.74	
	$^{88}\text{Sr}^+$	1.69	11.874	0.570	114.18	
$^{88}\text{Sr}$	$^{174}\text{Yb}^+$	1.98	1.563	0.075	235.35	[112]
	$^{171}\text{Yb}^+$	1.94	1.581	0.076	234.65	
	$^{138}\text{Ba}^+$	1.57	1.849	0.089	225.66	
	$^{88}\text{Sr}^+$	1.00	2.758	0.132	204.18	

## A.3. Construction manual for assembling the coils

This manual is based on the procedure of coil manufacturing developed in Prof. Jochim's group *Ultracold Quantum Gases* at the university of Heidelberg and has been adapted to our setup.

One coil requires the following items:

- Polyamide isolated copper wire (rectangular,  $1 \times 5$  mm).
- Epotec 353ND epoxy (about 10 g per coil).
- AIT ME7159 (diamond adhesive, about 2 g per coil).
- Indium wire for soldering.
- Kapton Tape

For the production process one requires:

- Winding reel in required dimensions.
- A lathe for winding the wire.
- A small pot to prepare the adhesive.
- A small spatula for covering the wire with adhesive.
- Several clamps to hold and fix the winded coil.
- An oven for the curing process.
- Sandpaper in different grain types to take off the isolation.
- A multimeter to locate shorts.
- Kapton spacer and torque wrench to determine maximum contact pressure

### 1. Winding and glueing the coil:

Our winding reel has a slit leading from its centre outwards which is used to hold the wire during the winding process. At the edge the slit slightly bends around the corner (see fig. A.1). This ensures a round shape of the wound coil. The winding reel is mounted onto the lathe and one end of the cleaned wire is pushed into the slit. Now the winding process begins while care has to be taken that the windings are as tight as possible and that the coil is wound in the correct direction. It turned out that for this procedure at least three persons are required. One holding the wire while keeping it under tension, one for rotating the winding reel and one to cover the coil with adhesive. As can be seen in the second picture of fig. A.1 we built an additional part for the winding reel that can be screwed on top of the winding reel for flattening the surface of the coil and to hold it during the winding



**Figure A.1.:** Manufacturing a coil.

and the curing process. When the coil is wound and clamped the remaining wire is cut off and the coil is cured in the oven according to instructions.

**2. Prepare the coil:**

Since the polyamide isolation of the wire has a low heat conductivity the coil would heat up to high temperatures which would destroy the coil. To prevent this the isolation has to be taken off at one side which is done in the workshop (third picture of fig. A.1). Now it has to be checked if there are any shorts between the loops using a multimeter (Also measure the resistance of the whole coil). These can be cured with a thin tip and with sandpaper.

**3. Glue heat sink on coil:**

It is recommended to use Kapton spacers and a torque wrench to first determine the maximum contact pressure that can be exerted between the heat sink and the



**Figure A.2.:** CAD model of assembled coil.

coil before shorts occur. Right before the glueing it is also recommended to clean the copper surfaces, because the oxide film reduces the thermal conductivity.

2 g of the diamond adhesive (AIT ME7159) need to be thawed. This expensive adhesive combines high thermal conduction with electric non-conductivity. First the coil and the heat sink are prebaked for some time in the oven at 50-60 °C. Then the coil is coated with the diamond adhesive until the copper is no longer visible (put some more adhesive at the edges). After shortly heating-up the coil once more at 50-60 °C the heat sink is mounted on it. Using the torque wrench we can precisely control the contact pressure (constantly check for shorts). Now the adhesive is cured in the oven, starting at 80 °C for 1 h, which is increased to at 100 °C for another 1 h and finally at 140 °C for 1 h again.

#### 4. Mounting the electric contacts

The electric contacts are soldered at the coil with indium. For this purpose the coating of the wire has to be sanded off with the sandpaper. The soldering is done by slowly heating-up the coil to 115-120 °C followed by directly coating the contacts with indium. Kapton tape is used to isolate the contacts from each other and the heat sink.

#### 5. Testing the coils

For this purpose the electric resistivity of the finished coil is measured and compared to the result from the bare wound wire (see 2.). It also makes sense to measure the terminal resistance between the contact and the wire and to measure the electric resistance as function of the coil-temperature.

## A.4. Assembling the trap

The ion trap will be glued on top of the atom trap using the UV adhesive: EPO-TEK® OG142-112 UV Cure Optical Epoxy. The adhesive is carefully applied at the edges of the ion trap while preventing the adhesive to run between the two traps. Afterwards the adhesive is cured by illuminating it three times for 10 s with UV laser-light (protection goggles!).

The electric circuits at the chips are connected to each other using a wire bonder. We have a gold coated AlN-substrate test-piece from Siegen and a broken ion trap which I used to test the glueing process and wire bonding for several settings. I chose the following bonding parameters:

Parameter	Bond1	Bond2
Power [mW]	200	350
Time [ms]	200	200
Force [cN]	60	60
Length [ $\mu\text{m}$ ]	200	200

A.5. Atomic level schemes

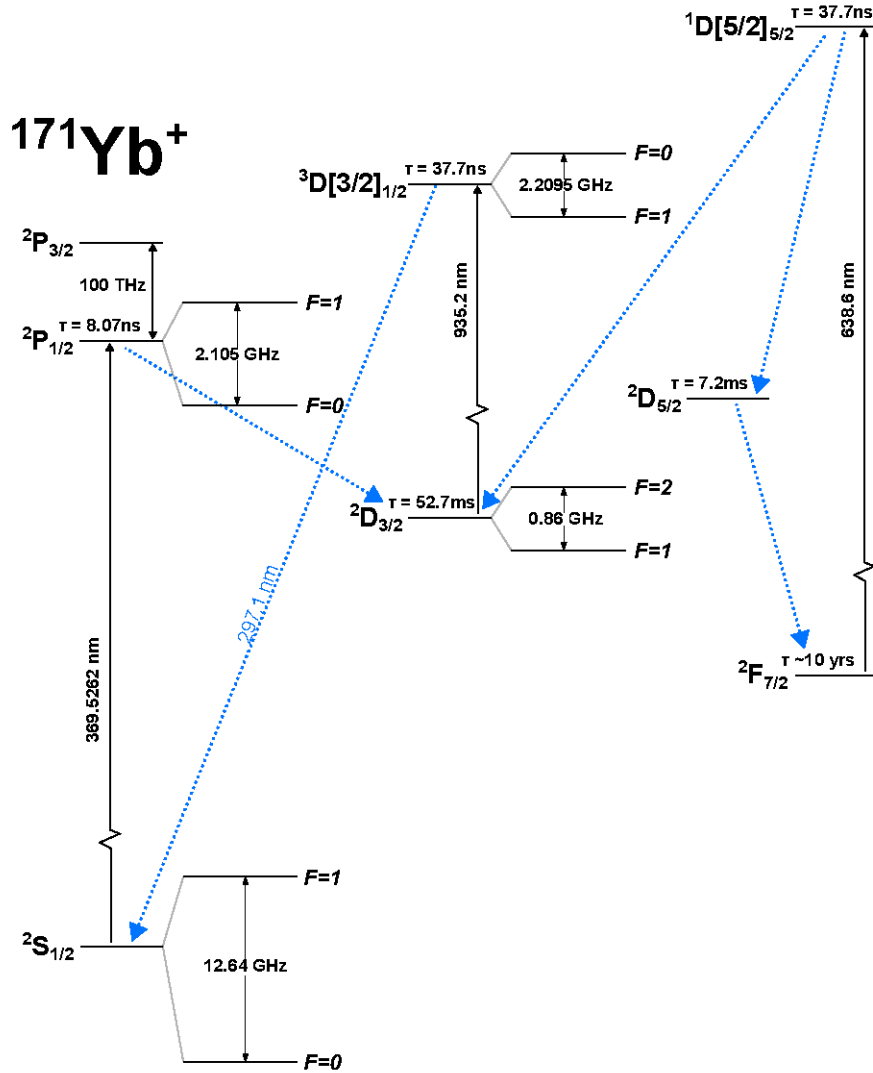


Figure A.3.: [119–121]

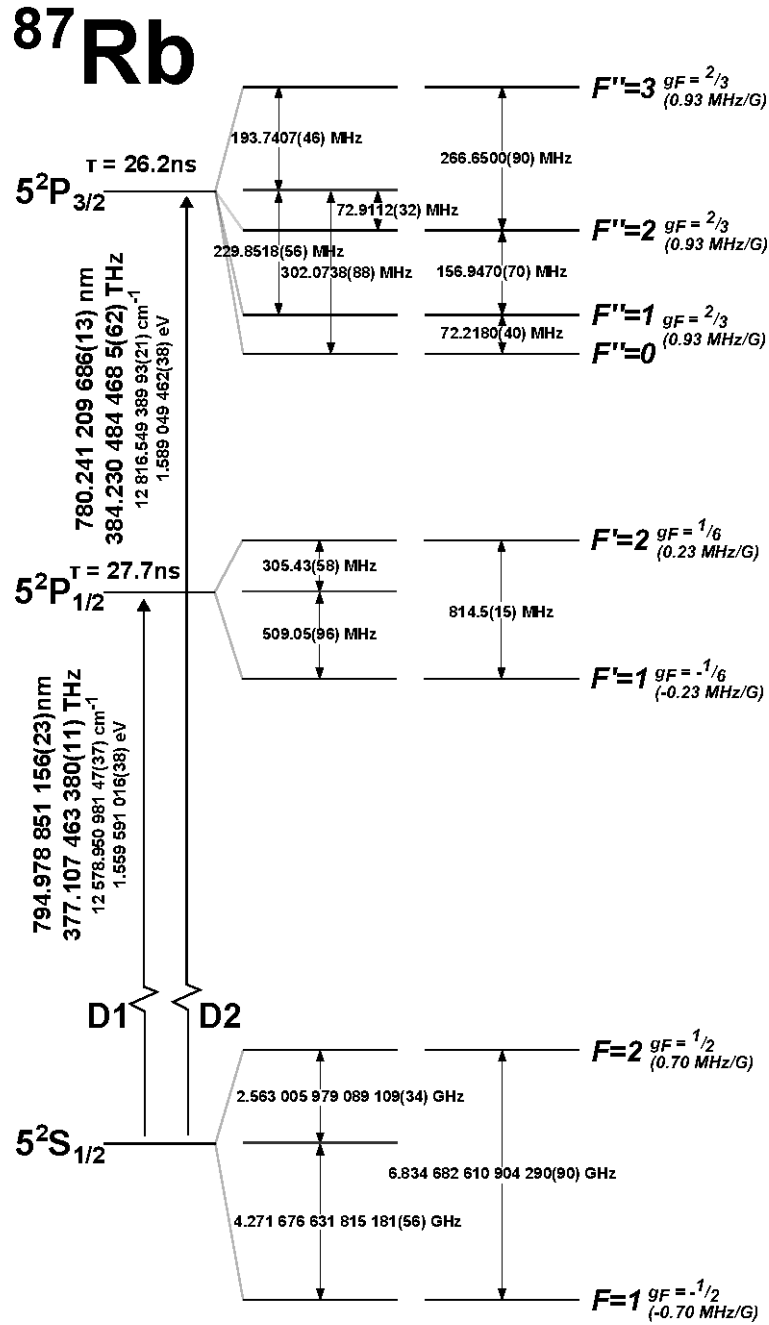


Figure A.4.: [92]

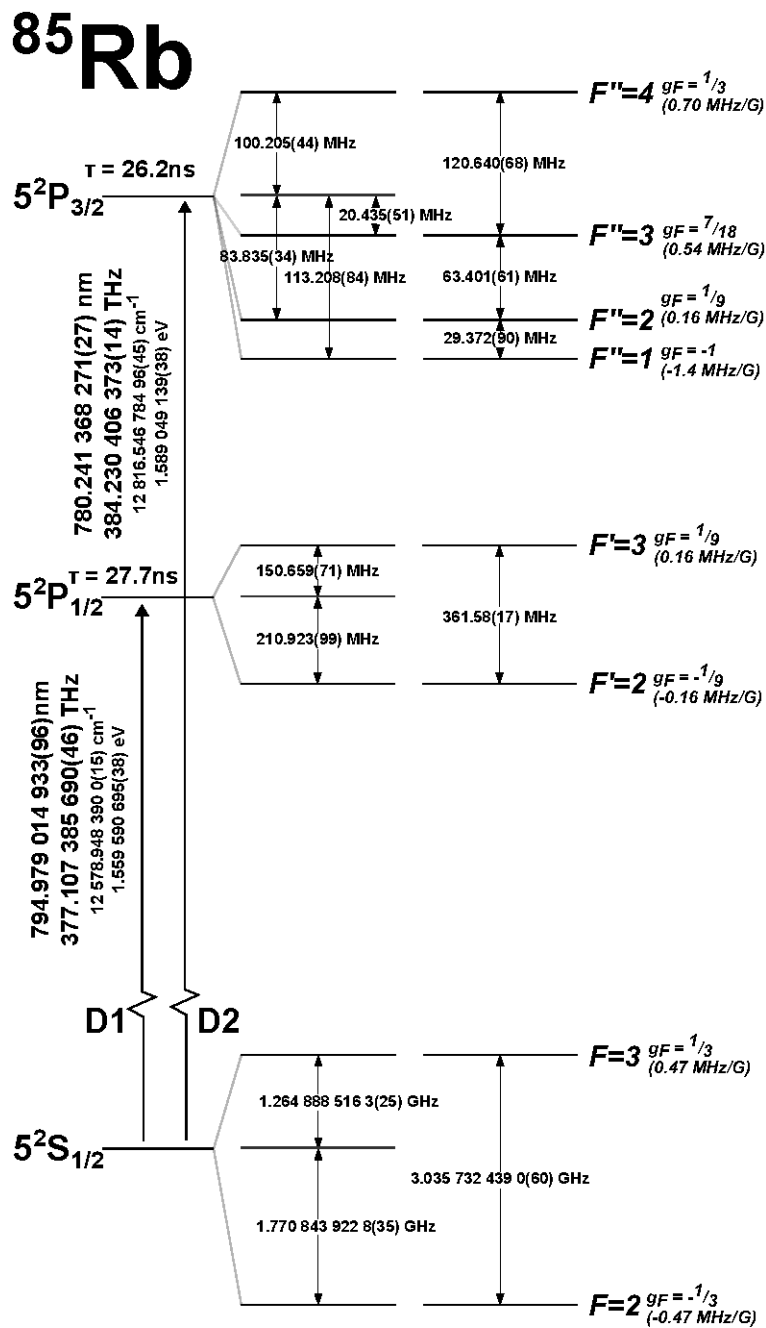


Figure A.5.: [122]

## A.6. Electronic schemes and technical drawings

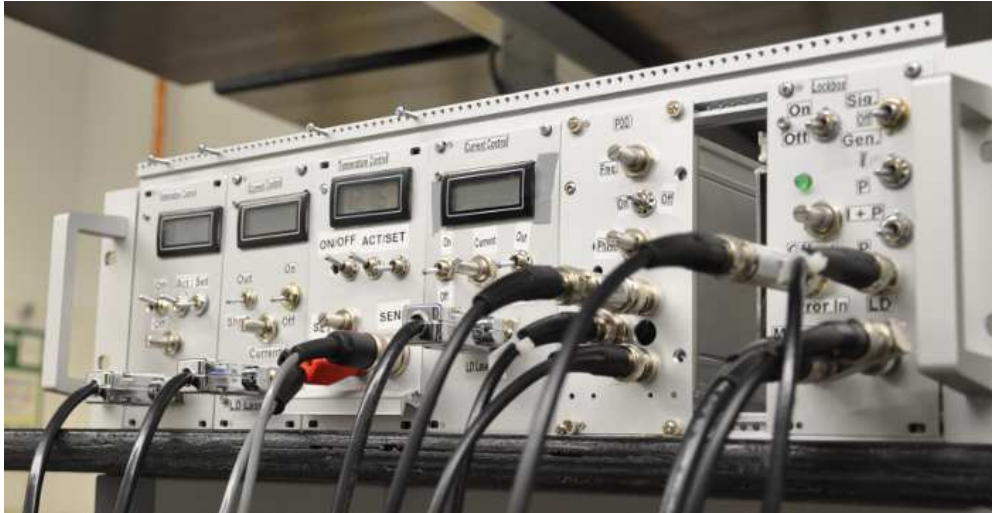


Figure A.6.: Self-constructed electronic devices for master-slave laser setup.

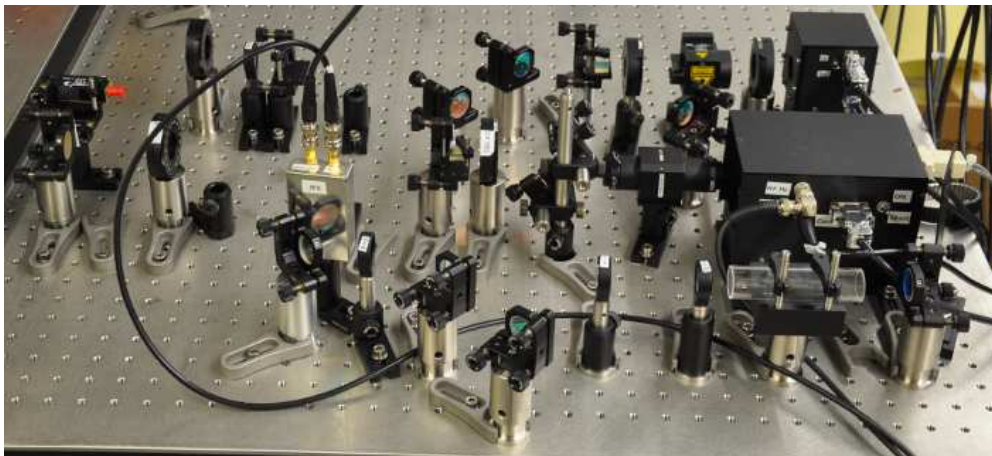
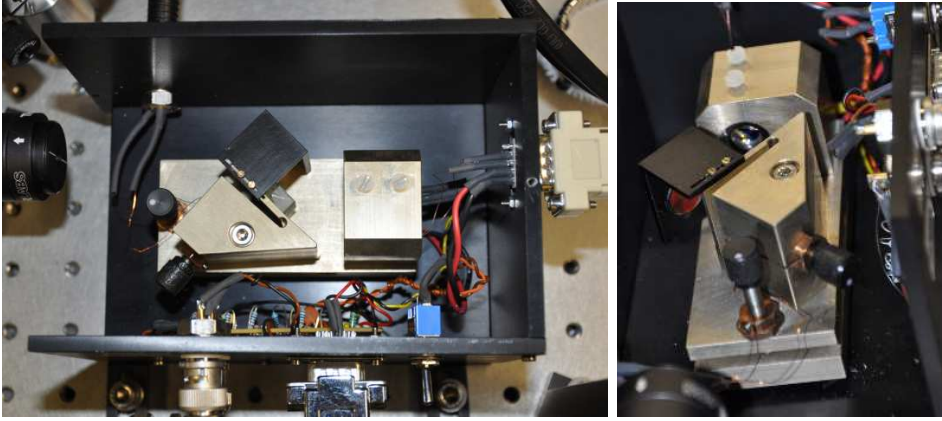
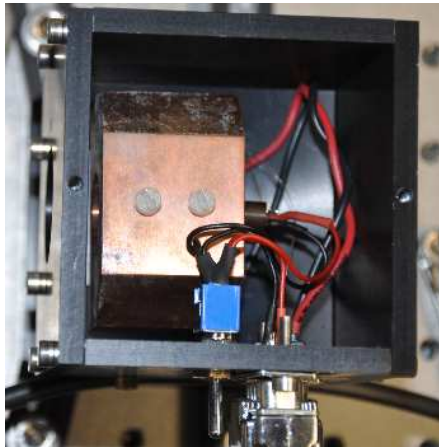


Figure A.7.: Master-slave laser setup



**Figure A.8.:** Master laser



**Figure A.9.:** Slave laser

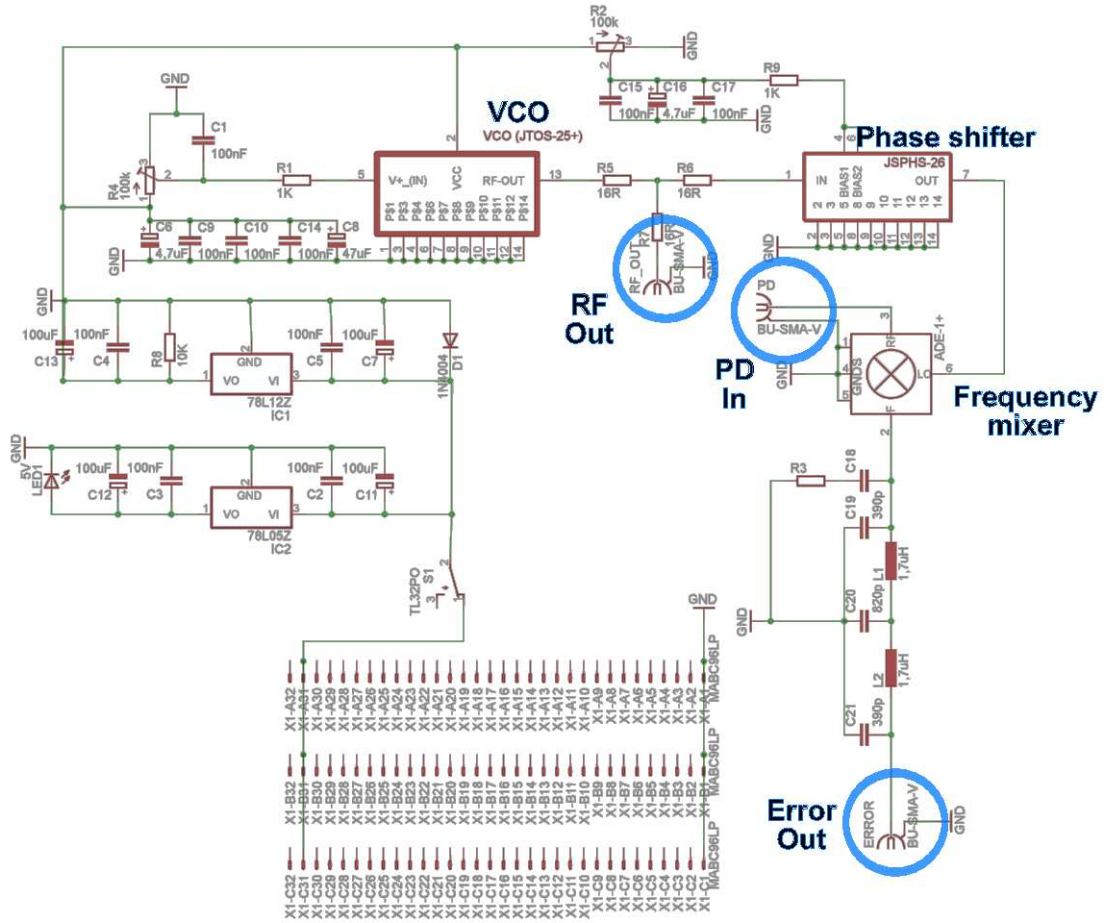


Figure A.10.: Electrical circuit of Pound-Drever driver

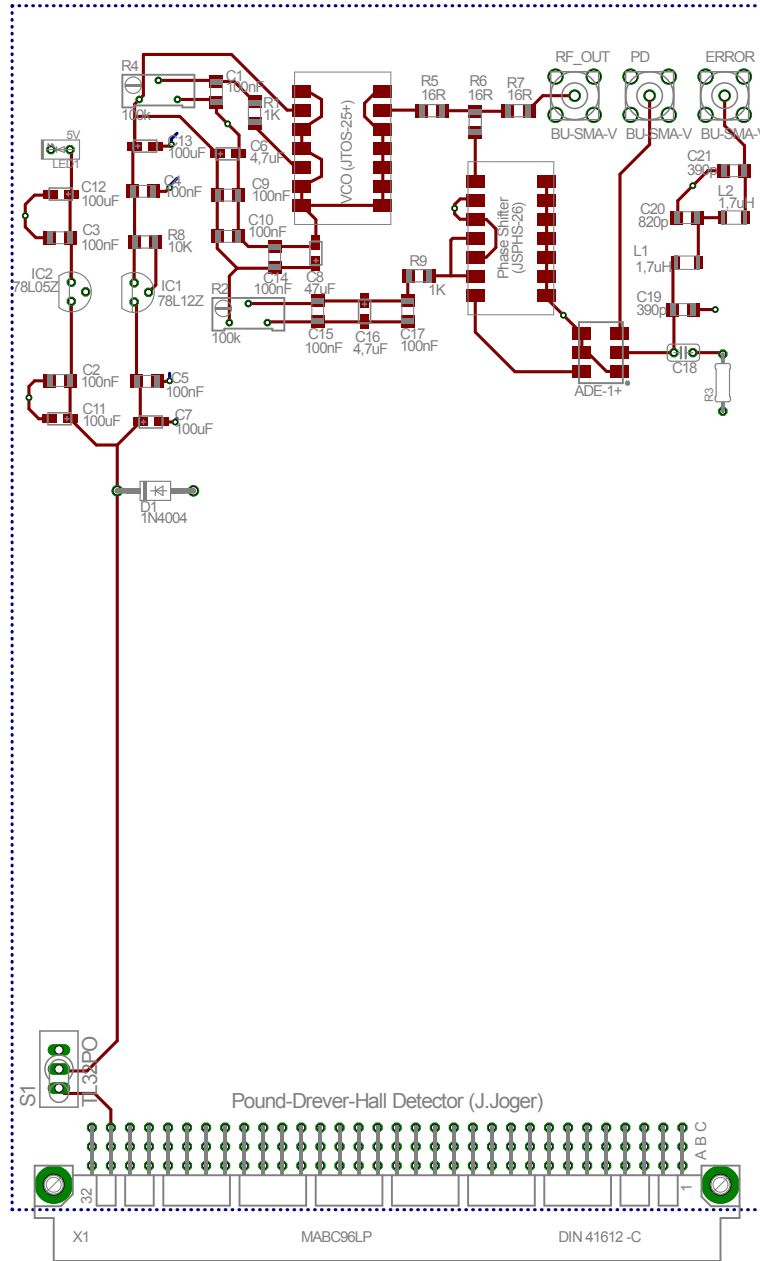


Figure A.11.: Self-mate board design of Pound-Drever driver

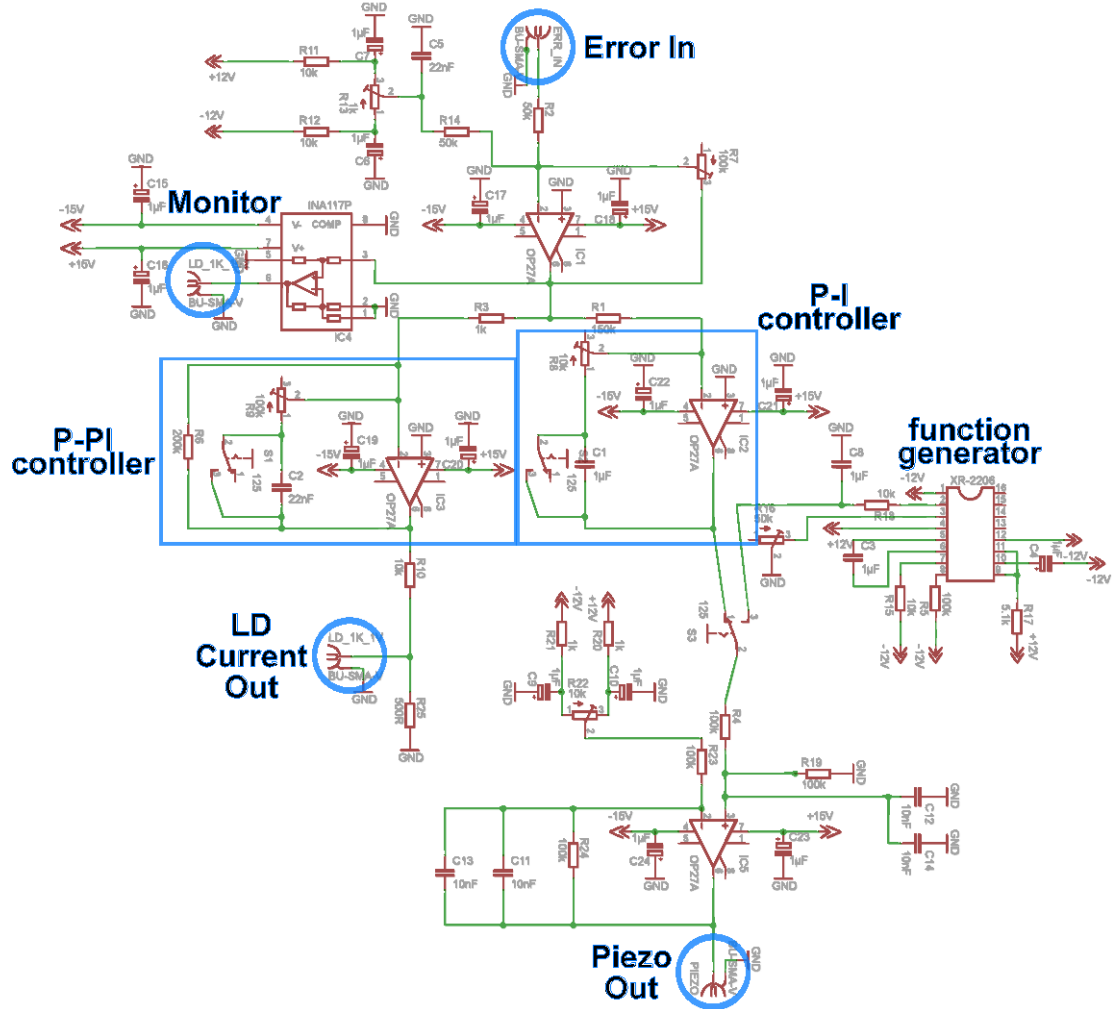


Figure A.12.: Electrical circuit of lockbox

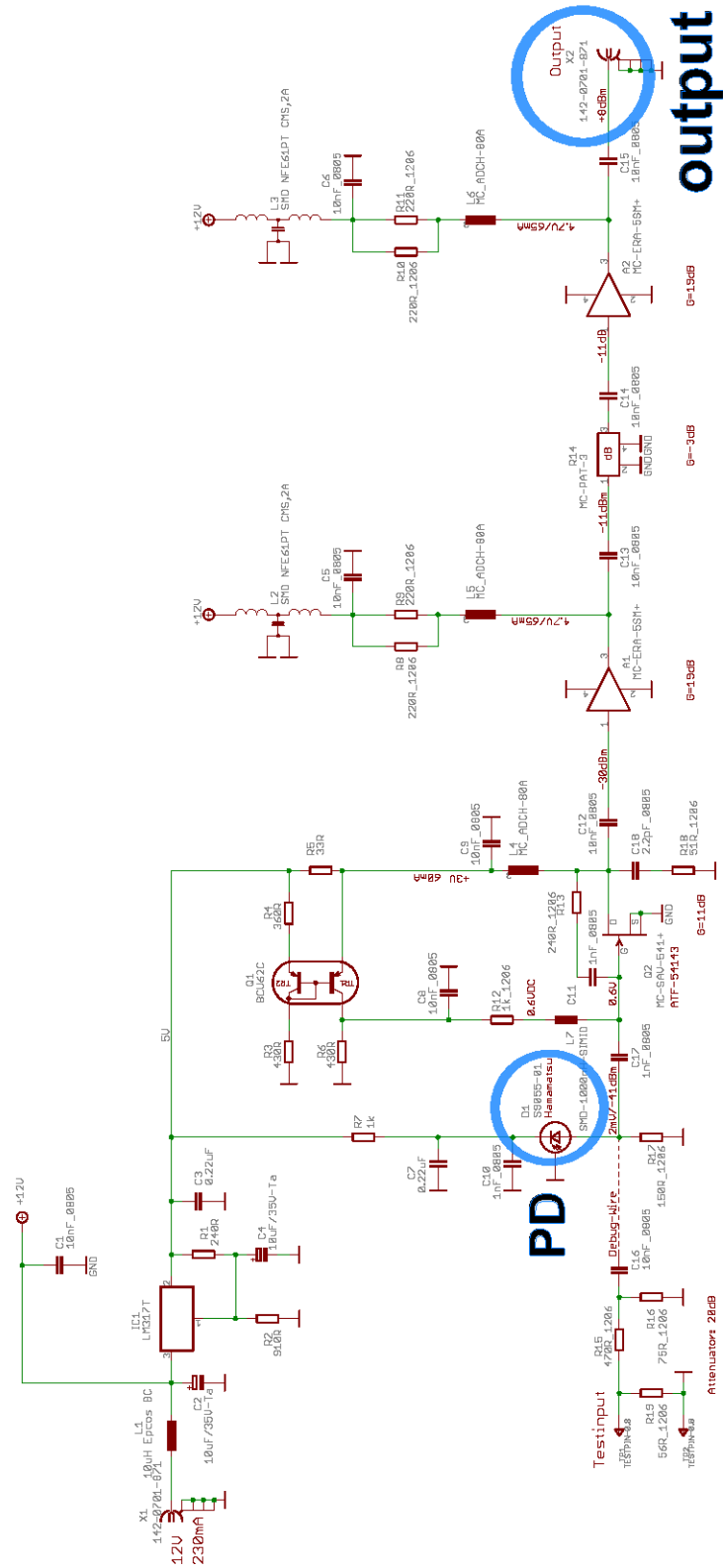


Figure A.13.: Electrical circuit of RF-photodiode amplifier, 10MHz...2GHz [H.Lenk 2010]

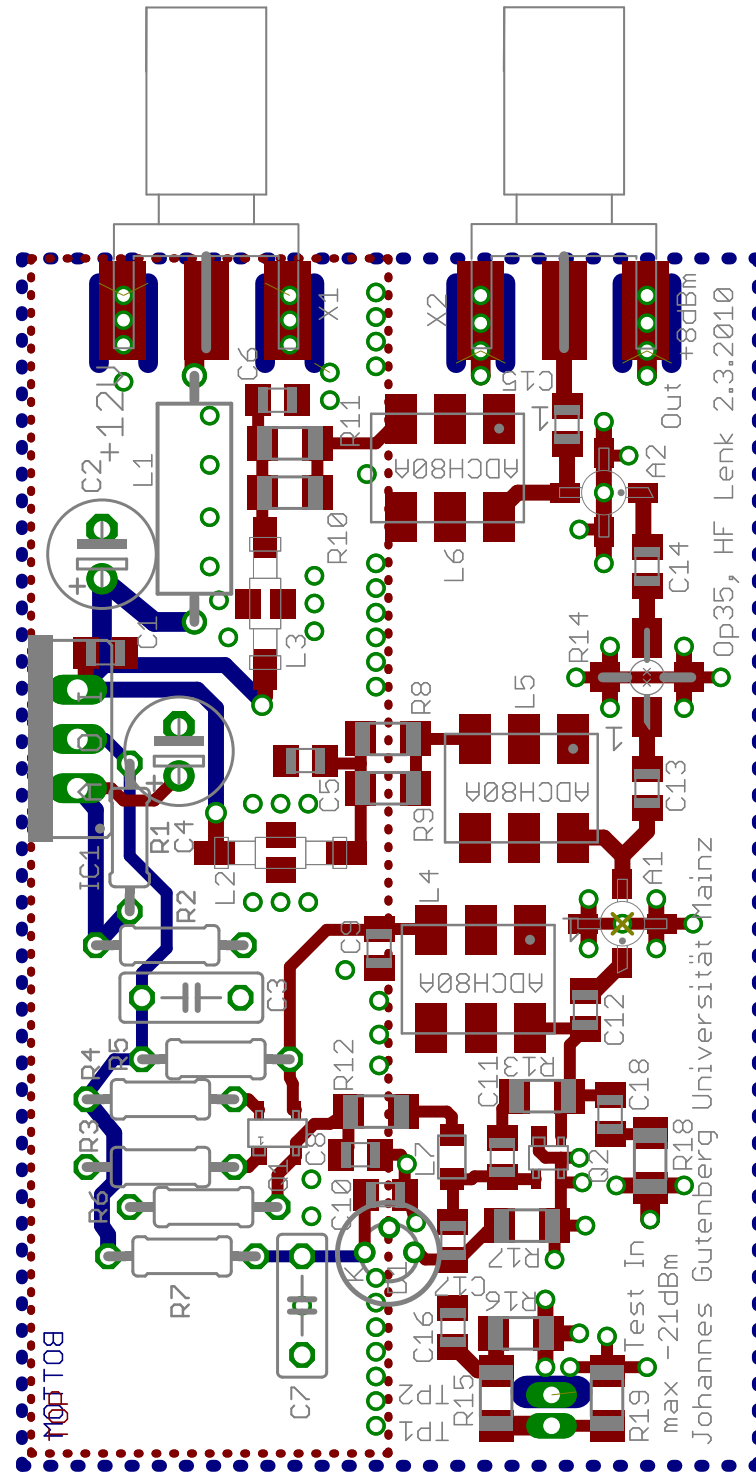


Figure A.14.: Board design of RF-photodiode amplifier, 10MHz...2GHz [H.Lenk 2010]

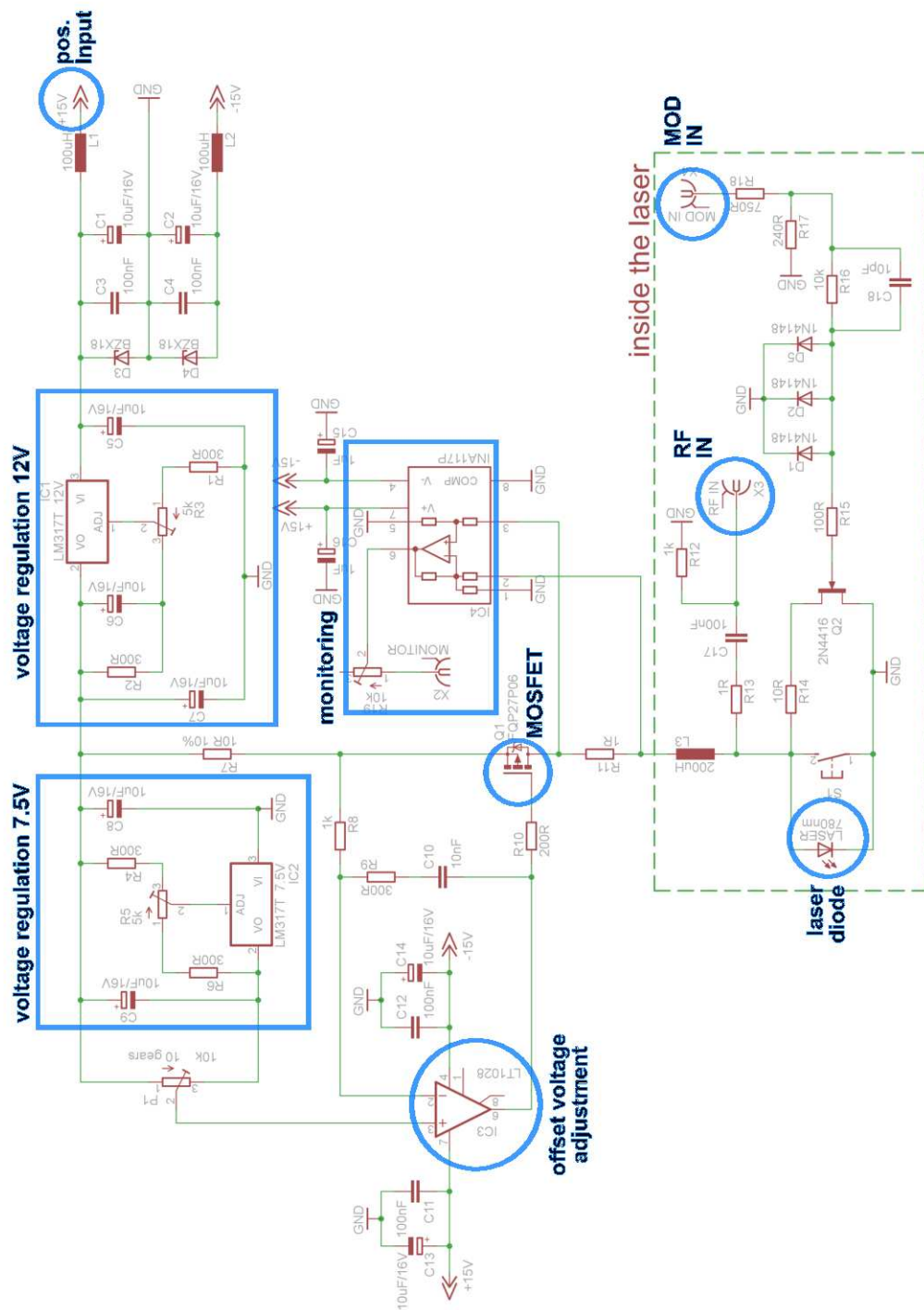


Figure A.15.: Electrical circuit of the current driver for a positive supply.

A. Vacuum components

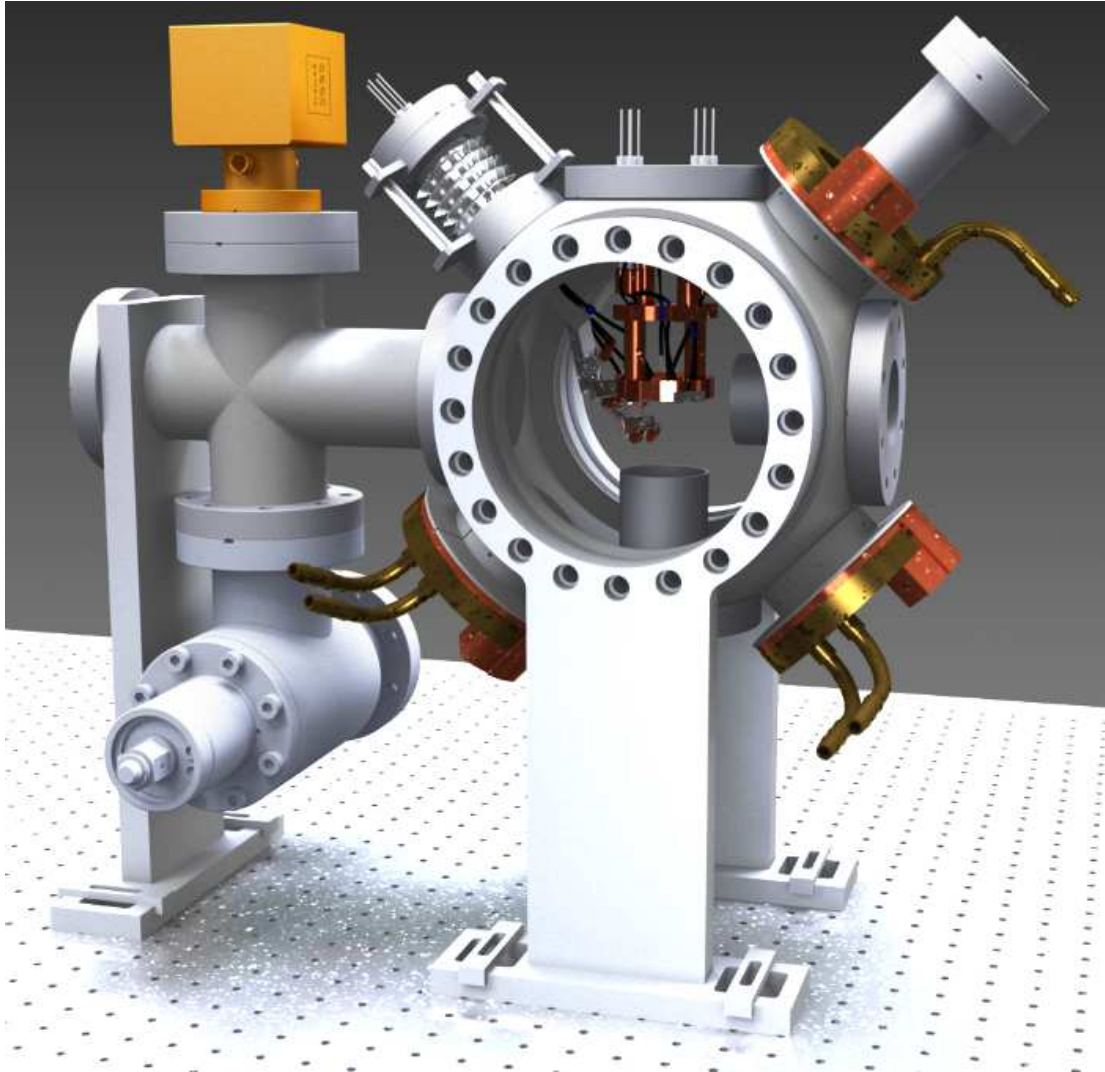


Figure A.16.: Complete design of vacuum setup.

Trap carrier

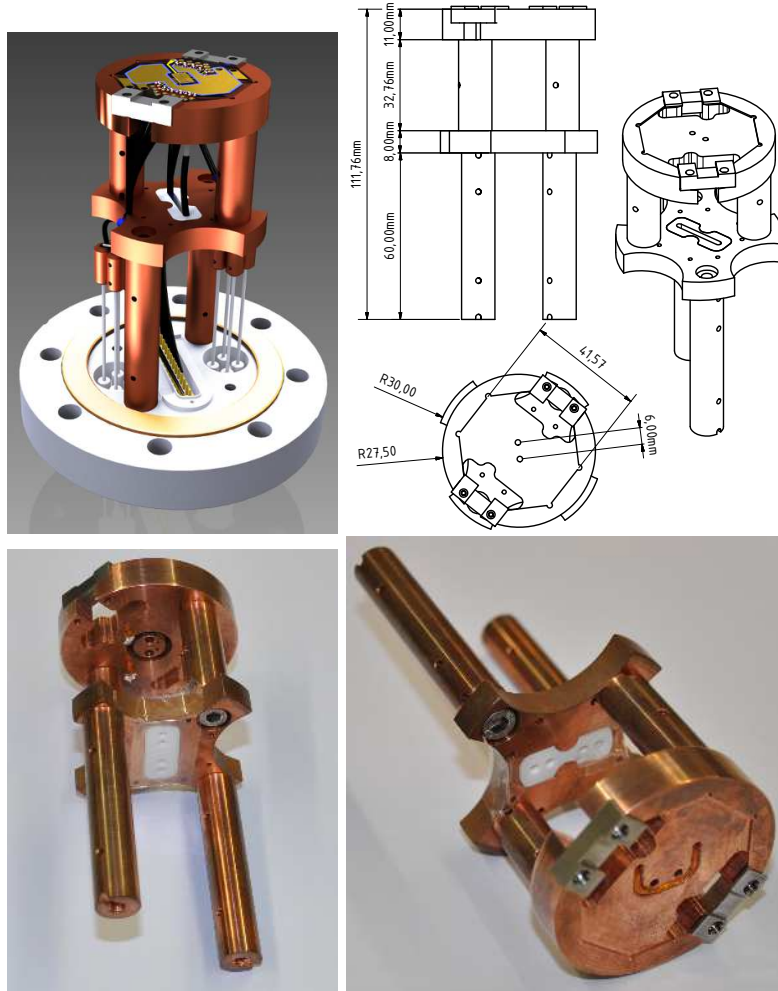


Figure A.17.: Trap carrier attached to a special CF63 flange with various electrical feedthroughs.

Ion source carrier

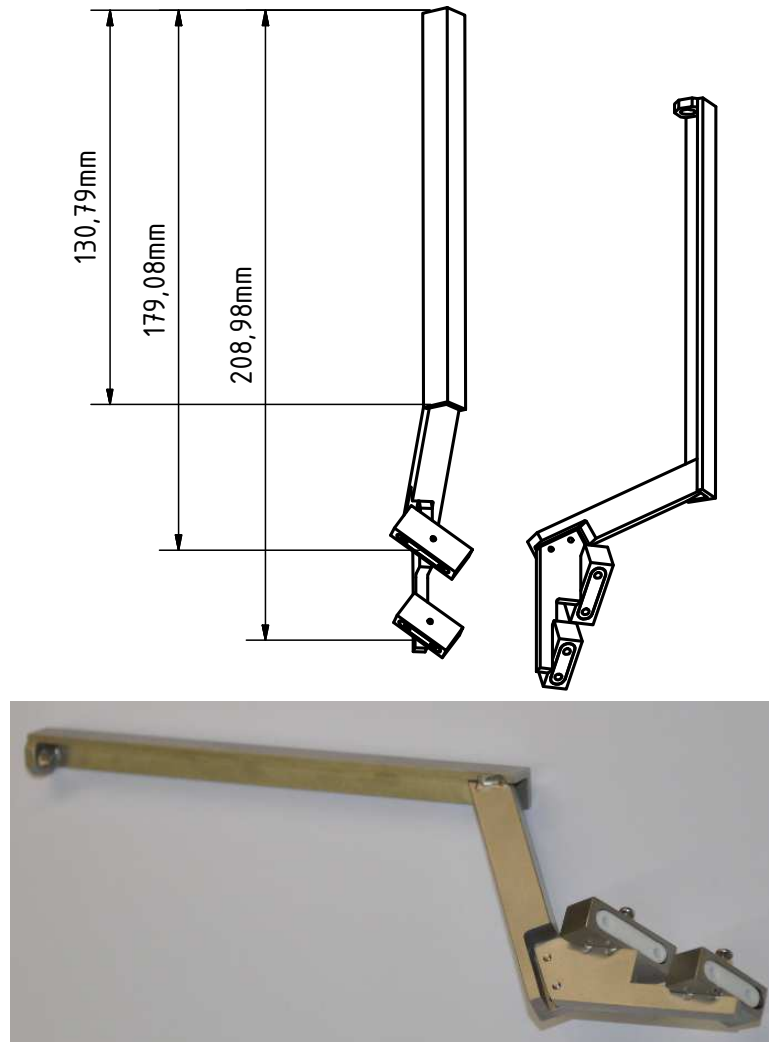


Figure A.18.: Ion source carrier

Special flanges

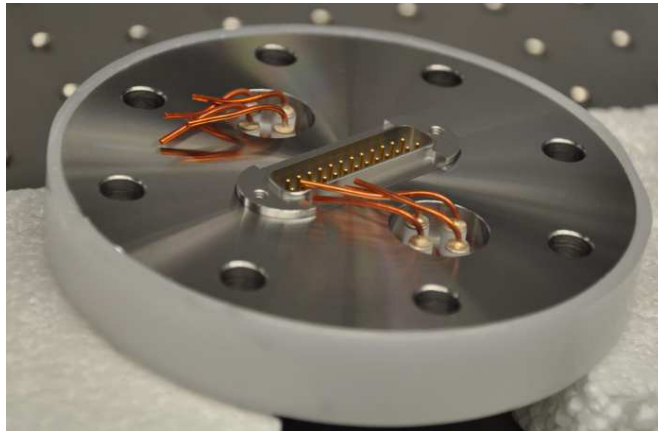
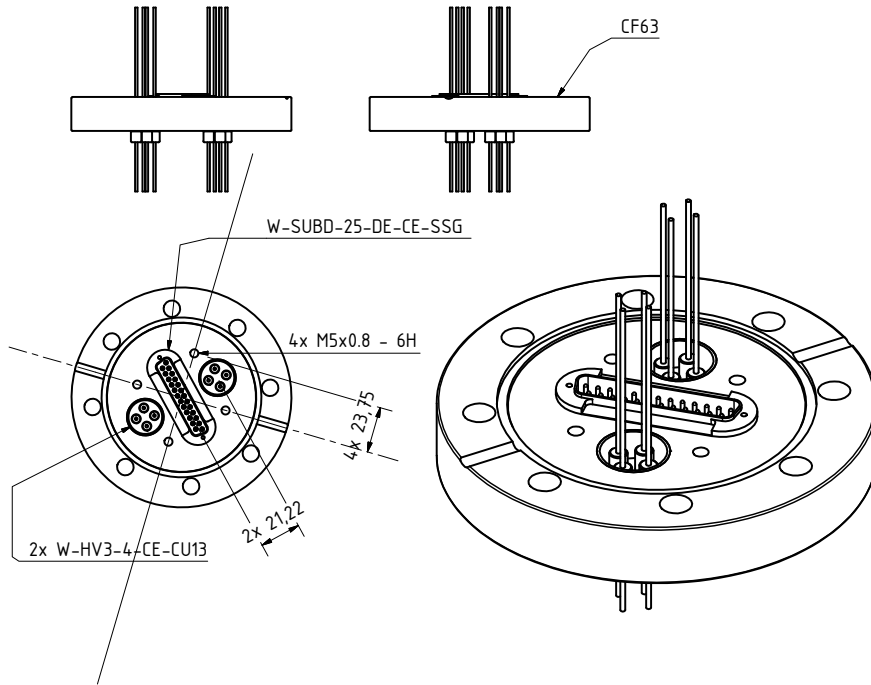


Figure A.19.: Special CF63 flange for the trap carrier.

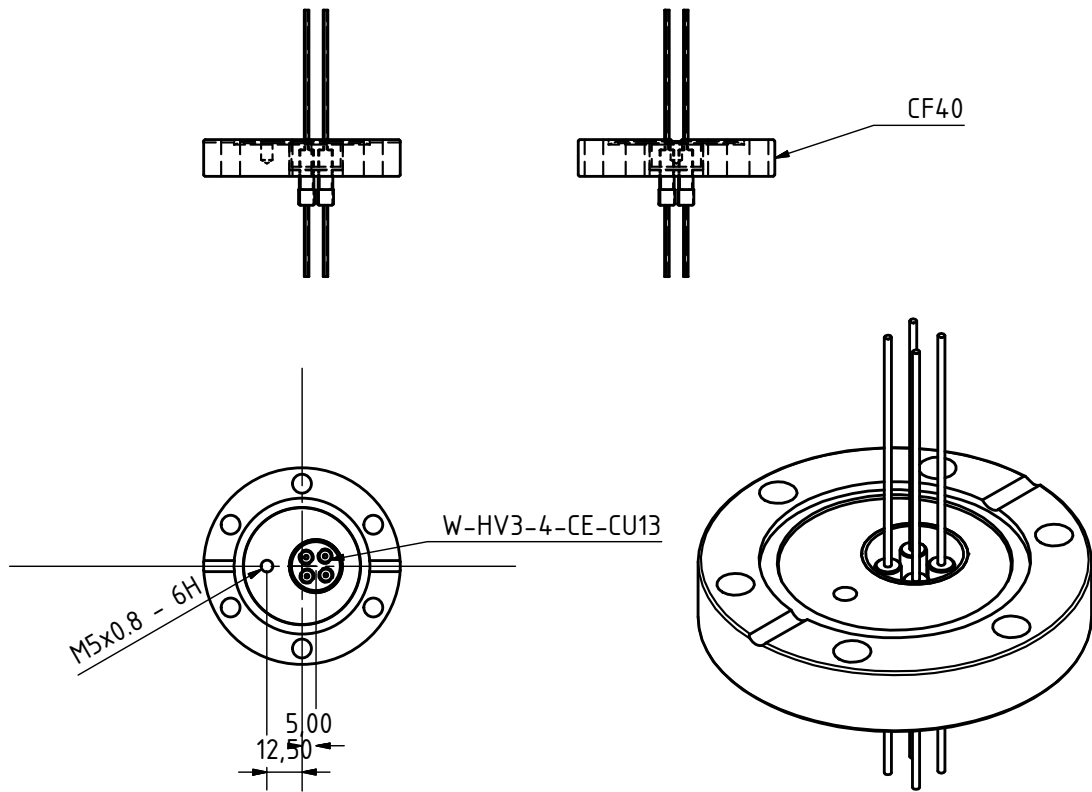


Figure A.20.: Special CF40 flange for the ion source carrier.

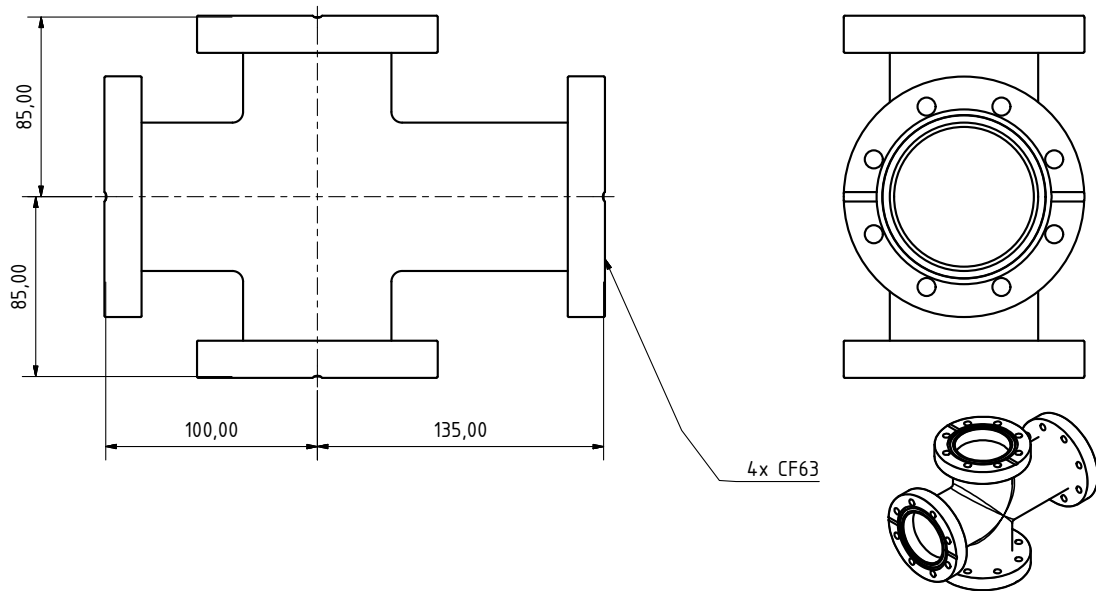
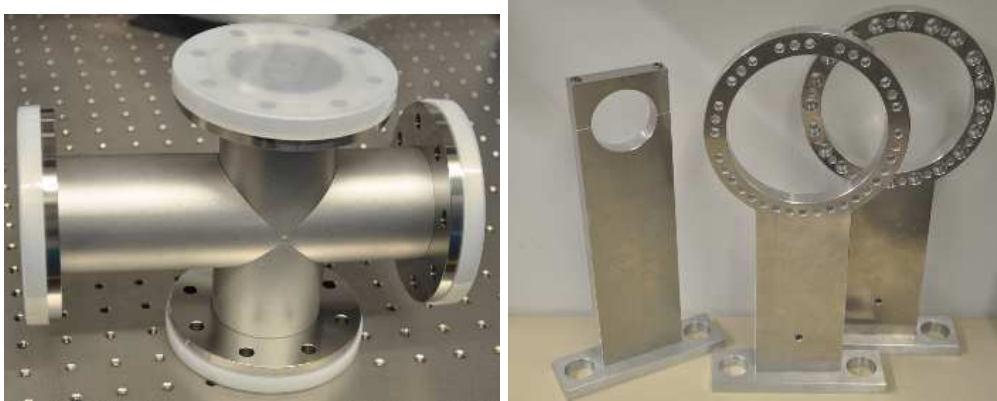


Figure A.21.: Special CF63 Cross.



**Figure A.22.:** Special CF63 Cross and Carriers for the vacuum setup

## A.7. Tables and measurements

Temperature Control: Relation between value displayed and real temperature.

Temperature (T) [°C]	displayed value (A)	$\Delta T$ [°C]	$\Delta A$
24.5	1029	5	1
27.	970	5	1
26.	985	5	1
23.5	1067	5	1
22.	1102	5	1
21.5	1140	5	1
21.	1188	5	1
20.	1222	5	1
20.	1240	5	1
19.5	1291	5	1
18.5	1350	5	1
17.	1386	5	1
17.	1411	5	1

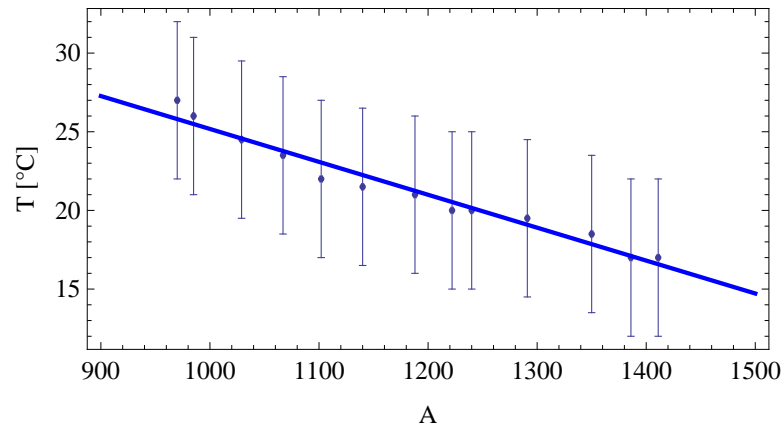
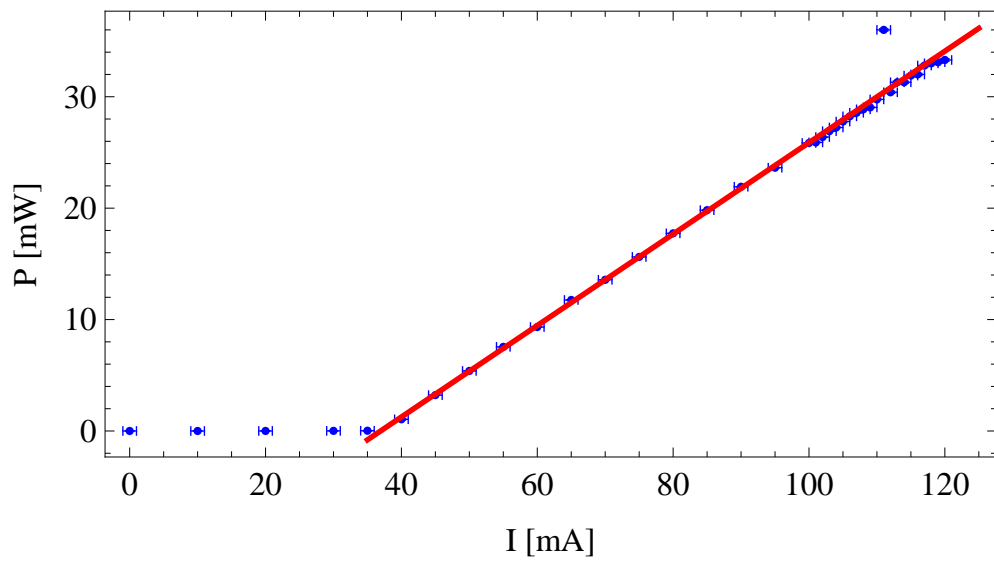


Figure A.23.: Relation between value displayed and real temperature.

## Master laser: relation between applied current and laser power

I [mA]	P [mW]	$\Delta I$ [mA]	$\Delta P$ [mW]
0	0.0004	1	0.0001
10	0.0011	1	0.0001
20	0.0045	1	0.0001
30	0.0114	1	0.0001
35	0.0233	1	0.0001
40	1.05	1	0.07
45	3.22	1	0.02
50	5.39	1	0.01
55	7.55	1	0.01
60	9.33	1	0.01
65	11.76	1	0.02
70	13.57	1	0.01
75	15.62	1	0.02
80	17.74	1	0.01
85	19.82	1	0.02
90	21.92	1	0.01
95	23.63	1	0.02
100	25.85	1	0.02
101	25.9	1	0.02
102	26.38	1	0.02
103	26.91	1	0.02
104	27.24	1	0.02
105	27.77	1	0.02
106	28.24	1	0.02
107	28.56	1	0.01
108	28.87	1	0.02
109	29.04	1	0.02
110	29.76	1	0.02
111	36.	1	0.1
112	30.4	1	0.1
113	31.3	1	0.1
114	31.3	1	0.1
115	31.9	1	0.1
116	32.	1	0.1
117	32.8	1	0.1
118	33.	1	0.1
119	33.1	1	0.1
120	33.3	1	0.1



**Figure A.24.:** Relation between applied current and laser power of master laser.

Slave laser: relation between applied current and laser power right behind the optical isolator

I [mA]	P [mW]	$\Delta I$ [mA]	$\Delta P$ [mW]
0	0	1	0.01
10	0.01	1	0.01
30	0.01	1	0.01
50	0.02	1	0.01
70	0.06	1	0.01
90	1.98	1	0.01
100	10.06	1	0.01
120	24.23	1	0.01
141	38.4	1	0.1
160	51	1	0.1
160	64.1	1	0.1
200	77.2	1	0.1
230	97	1	0.1
260	114.8	1	0.1
290	133.5	1	0.1
320	151.1	1	0.1
350	168.1	1	0.1

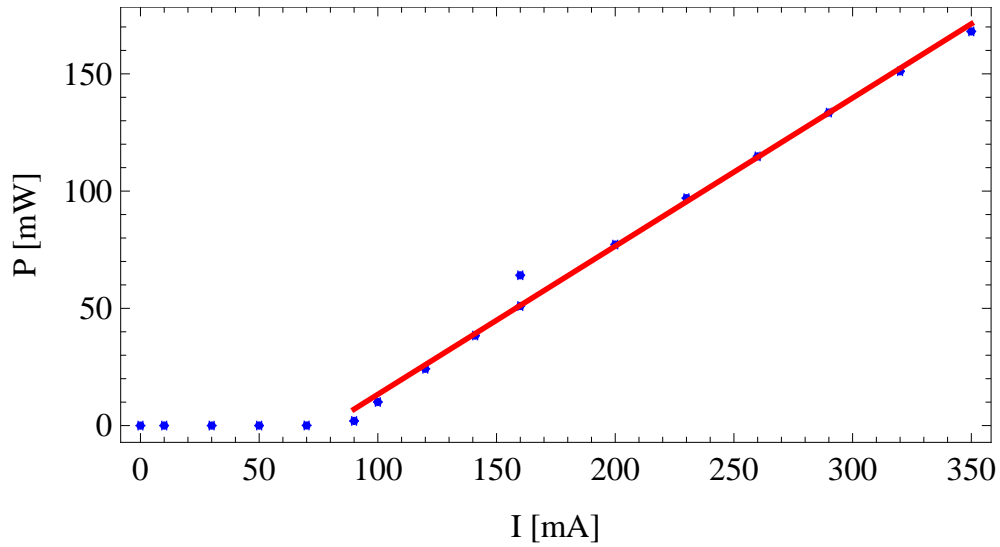


Figure A.25.: Relation between applied current and laser power of slave laser.



# Bibliography

- [1] P Massignan, C J Pethick, and H Smith. Static properties of positive ions in atomic Bose-Einstein condensates. *Phys. Rev. A*, 71:023606, Feb 2005.
- [2] S Schmid, A Härter, and J H Denschlag. Dynamics of a cold trapped ion in a Bose-Einstein condensate. *Phys. Rev. Lett.*, 105:133202, Sep 2010.
- [3] K Ravi, S Lee, A Sharma, G Werth, and SA Rangwala. Combined ion and atom trap for low-temperature ion-atom physics. *Applied Physics B*, 107(4):971–981, 2012.
- [4] C Zipkes, S Palzer, C Sias, and M Köhl. A trapped single ion inside a Bose-Einstein condensate. *Nature*, 464(7287):388–391, 2010.
- [5] S Schmid, A Harter, A Frisch, S Hoinka, and J H Denschlag. An apparatus for immersing trapped ions into an ultracold gas of neutral atoms. *Review of Scientific Instruments*, 83(5):053108–053108, 2012.
- [6] L H Nguyễn, A Kalev, M D Barrett, and B-G Englert. Micromotion in trapped atom-ion systems. *Phys. Rev. A*, 85:052718, May 2012.
- [7] A Härter and J H Denschlag. Cold atom-ion experiments in hybrid traps. *arXiv preprint arXiv:1309.5799*, 2013.
- [8] R Côté and A Dalgarno. Ultracold atom-ion collisions. *Phys. Rev. A*, 62:012709, Jun 2000.
- [9] B Gao, E Tiesinga, C J Williams, and P S Julienne. Multichannel quantum-defect theory for slow atomic collisions. *Phys. Rev. A*, 72:042719, Oct 2005.
- [10] Z Idziaszek, T Calarco, and P Zoller. Controlled collisions of a single atom and an ion guided by movable trapping potentials. *Phys. Rev. A*, 76:033409, Sep 2007.
- [11] Hauke D. An atom-ion quantum gate. Master’s thesis, Universität Ulm, 2008.
- [12] S Willitsch, M T Bell, A D Gingell, S R Procter, and T P Softley. Cold reactive collisions between laser-cooled ions and velocity-selected neutral molecules. *Phys. Rev. Lett.*, 100:043203, Jan 2008.
- [13] A T Grier, M Cetina, F Oručević, and V Vuletić. Observation of cold collisions between trapped ions and trapped atoms. *Physical review letters*, 102(22):223201, 2009.
- [14] Z Idziaszek, T Calarco, P S Julienne, and A Simoni. Quantum theory of ultracold atom-ion collisions. *Phys. Rev. A*, 79:010702, Jan 2009.

- [15] C Zipkes, S Palzer, L Ratschbacher, C Sias, and M Köhl. Cold heteronuclear atom-ion collisions. *Phys. Rev. Lett.*, 105:133201, Sep 2010.
- [16] H Doerk, Z Idziaszek, and T Calarco. Atom-ion quantum gate. *Phys. Rev. A*, 81:012708, Jan 2010.
- [17] Z Idziaszek, A Simoni, T Calarco, and P S Julienne. Multichannel quantum-defect theory for ultracold atom-ion collisions. *New Journal of Physics*, 13(8):083005, 2011.
- [18] A Simoni and J-M Launay. Landau quantization effects in ultracold atom-ion collisions. *Journal of Physics B: Atomic, Molecular and Optical Physics*, 44(23):235201, 2011.
- [19] V V Meshkov, A V Stolyarov, and R J Le Roy. Rapid, accurate calculation of the s-wave scattering length. *The Journal of chemical physics*, 135:154108, 2011.
- [20] T P Snow and V M Bierbaum. Ion chemistry in the interstellar medium. *Annu. Rev. Anal. Chem.*, 1:229–259, 2008.
- [21] W G Rellergert, S T Sullivan, S Kotochigova, A Petrov, K Chen, S J Schowalter, and E R Hudson. Measurement of a large chemical reaction rate between ultracold closed-shell  $^{40}\text{Ca}$  atoms and open-shell  $^{174}\text{Yb}^+$  ions held in a hybrid atom-ion trap. *Phys. Rev. Lett.*, 107:243201, Dec 2011.
- [22] R Côté, V Kharchenko, and M D Lukin. Mesoscopic molecular ions in Bose-Einstein condensates. *Phys. Rev. Lett.*, 89:093001, Aug 2002.
- [23] J Goold, H Doerk, Z Idziaszek, T Calarco, and Th Busch. Ion-induced density bubble in a strongly correlated one-dimensional gas. *Phys. Rev. A*, 81:041601, Apr 2010.
- [24] J Catani, G Lamporesi, D Naik, M Gring, M Inguscio, F Minardi, A Kantian, and T Giamarchi. Quantum dynamics of impurities in a one-dimensional bose gas. *Phys. Rev. A*, 85:023623, Feb 2012.
- [25] C Zipkes, L Ratschbacher, C Sias, and M Köhl. Kinetics of a single trapped ion in an ultracold buffer gas. *New Journal of Physics*, 13(5):053020, 2011.
- [26] I Bloch, J Dalibard, and W Zwerger. Many-body physics with ultracold gases. *Reviews of Modern Physics*, 80(3):885, 2008.
- [27] A J Daley, P O Fedichev, and P Zoller. Single-atom cooling by superfluid immersion: A nondestructive method for qubits. *Phys. Rev. A*, 69:022306, Feb 2004.
- [28] Z Idziaszek, T Calarco, and P Zoller. Ion-assisted ground-state cooling of a trapped polar molecule. *Phys. Rev. A*, 83:053413, May 2011.

- 
- [29] M Krych, W Skomorowski, F Pawłowski, R Moszynski, and Z Idziaszek. Sympathetic cooling of the  $\text{Ba}^+$  ion by collisions with ultracold Rb atoms: Theoretical prospects. *Phys. Rev. A*, 83:032723, Mar 2011.
- [30] K Ravi, S Lee, A Sharma, G Werth, and SA Rangwala. Cooling and stabilization by collisions in a mixed ion-atom system. *Nature communications*, 3:1126, 2012.
- [31] R Blatt and D Wineland. Entangled states of trapped atomic ions. *Nature*, 453(7198):1008–1015, 2008.
- [32] D Leibfried, R Blatt, C Monroe, and D Wineland. Quantum dynamics of single trapped ions. *Rev. Mod. Phys.*, 75:281–324, Mar 2003.
- [33] K Brugger, T Calarco, D Cassettari, R Folman, A Haase, B Hessmo, P Krüger, T Maier, and J Schmiedmayer. Nanofabricated atom optics: atom chips. *Journal of Modern Optics*, 47(14-15):2789–2809, 2000.
- [34] J I Cirac, P Zoller, et al. Quantum computations with cold trapped ions. *Physical review letters*, 74(20):4091–4094, 1995.
- [35] D Kielpinski, C Monroe, and D J Wineland. Architecture for a large-scale ion-trap quantum computer. *Nature*, 417(6890):709–711, 2002.
- [36] S Seidelin, J Chiaverini, R Reichle, J J Bollinger, D Leibfried, J Britton, J H Wesenberg, R B Blakestad, R J Epstein, D B Hume, W M Itano, J D Jost, C Langer, R Ozeri, N Shiga, and D J Wineland. Microfabricated surface-electrode ion trap for scalable quantum information processing.
- [37] J H Wesenberg. Electrostatics of surface-electrode ion traps. *Phys. Rev. A*, 78:063410, Dec 2008.
- [38] S Narayanan, N Daniilidis, SA Moller, R Clark, F Ziesel, K Singer, F Schmidt-Kaler, and H Haffner. Electric field compensation and sensing with a single ion in a planar trap. *Journal of Applied Physics*, 110(11):114909–114909, 2011.
- [39] J Reichel, W Hänsel, and T W Hänsch. Atomic micromanipulation with magnetic surface traps. *Phys. Rev. Lett.*, 83:3398–3401, Oct 1999.
- [40] H Ott, J Fortagh, G Schlotterbeck, A Grossmann, and C Zimmermann. Bose-Einstein condensation in a surface microtrap. *Phys. Rev. Lett.*, 87:230401, Nov 2001.
- [41] R Folman, P Krüger, J Schmiedmayer, J Denschlag, and C Henkel. Microscopic atom optics: from wires to an atom chip. *Advances in Atomic, Molecular, and Optical Physics*, 48:263–356, 2002.
- [42] M HT Extavour. Design and construction of magnetic elements for trapping and transport of cold neutral atoms. *University of Toronto*, 2004.

- [43] S Wildermuth, P Krüger, C Becker, M Brajdic, S Haupt, A Kasper, R Folman, and J Schmiedmayer. Optimized magneto-optical trap for experiments with ultracold atoms near surfaces. *Phys. Rev. A*, 69:030901, Mar 2004.
- [44] S Wildermuth, S Hofferberth, I Lesanovsky, E Haller, L M Andersson, S Groth, I Bar-Joseph, P Krüger, and J Schmiedmayer. Bose-Einstein condensates: microscopic magnetic-field imaging. *Nature*, 435(7041):440–440, 2005.
- [45] A Görlitz, J M Vogels, A E Leanhardt, C Raman, T L Gustavson, J R Abo-Shaer, A P Chikkatur, S Gupta, S Inouye, T Rosenband, and W Ketterle. Realization of Bose-Einstein condensates in lower dimensions. *Phys. Rev. Lett.*, 87:130402, Sep 2001.
- [46] J Esteve, J-B Trebbia, T Schumm, A Aspect, C I Westbrook, and I Bouchoule. Observations of density fluctuations in an elongated Bose gas: Ideal gas and quasicondensate regimes. *Phys. Rev. Lett.*, 96:130403, Apr 2006.
- [47] J Fortágh, H Ott, S Kraft, A Günther, and C Zimmermann. Bose-Einstein condensates in magnetic waveguides. *Applied Physics B*, 76(2):157–163, 2003.
- [48] T Schumm, S Hofferberth, L Mauritz Andersson, S Wildermuth, S Groth, I Bar-Joseph, J Schmiedmayer, and P Krüger. Matter-wave interferometry in a double well on an atom chip. *Nature Physics*, 1(1):57–62, 2005.
- [49] S Hofferberth, I Lesanovsky, B Fischer, T Schumm, and J Schmiedmayer. Non-equilibrium coherence dynamics in one-dimensional Bose gases. *Nature*, 449(7160):324–327, 2007.
- [50] G-B Jo, J-H Choi, C A Christensen, Y-R Lee, T A Pasquini, W Ketterle, and D E Pritchard. Matter-wave interferometry with phase fluctuating Bose-Einstein condensates. *Phys. Rev. Lett.*, 99:240406, Dec 2007.
- [51] R Gerritsma, A Negretti, H Doerk, Z Idziaszek, T Calarco, and F Schmidt-Kaler. Bosonic Josephson junction controlled by a single trapped ion. *Phys. Rev. Lett.*, 109:080402, Aug 2012.
- [52] B D Josephson. The discovery of tunnelling supercurrents. *Rev. Mod. Phys.*, 46:251–254, Apr 1974.
- [53] I Bouchoule. Modulational instabilities in Josephson oscillations of elongated coupled condensates. *The European Physical Journal D-Atomic, Molecular, Optical and Plasma Physics*, 35(1):147–154, 2005.
- [54] R Gati and M K Oberthaler. A bosonic Josephson junction. *Journal of Physics B: Atomic, Molecular and Optical Physics*, 40(10):R61, 2007.
- [55] S Levy, E Lahoud, I Shomroni, and J Steinhauer. The ac and dc josephson effects in a Bose-Einstein condensate. *Nature*, 449(7162):579–583, 2007.

- 
- [56] L J LeBlanc, A B Bardon, J McKeever, M H T Extavour, D Jervis, J H Thywissen, F Piazza, and A Smerzi. Dynamics of a tunable superfluid junction. *Phys. Rev. Lett.*, 106:025302, Jan 2011.
- [57] T Betz, S Manz, R Bücker, T Berrada, Ch Koller, G Kazakov, I E Mazets, H-P Stimming, A Perrin, T Schumm, and J Schmiedmayer. Two-point phase correlations of a one-dimensional bosonic Josephson junction. *Phys. Rev. Lett.*, 106:020407, Jan 2011.
- [58] A Eckardt, T Jinasundera, C Weiss, and M Holthaus. Analog of photon-assisted tunneling in a Bose-Einstein condensate. *Phys. Rev. Lett.*, 95:200401, Nov 2005.
- [59] J Grond, T Betz, U Hohenester, N J Mauser, J Schmiedmayer, and T Schumm. The shapiro effect in atomchip-based bosonic Josephson junctions. *New Journal of Physics*, 13(6):065026, 2011.
- [60] Q Y He, M D Reid, T G Vaughan, C Gross, M Oberthaler, and P D Drummond. Einstein-Podolsky-Rosen entanglement strategies in two-well Bose-Einstein condensates. *Phys. Rev. Lett.*, 106:120405, Mar 2011.
- [61] G J Milburn, J Corney, E M Wright, and D F Walls. Quantum dynamics of an atomic Bose-Einstein condensate in a double-well potential. *Phys. Rev. A*, 55:4318–4324, Jun 1997.
- [62] M Albiez, R Gati, J Fölling, S Hunsmann, M Cristiani, and M K Oberthaler. Direct observation of tunneling and nonlinear self-trapping in a single bosonic Josephson junction. *Phys. Rev. Lett.*, 95:010402, Jun 2005.
- [63] N Bar-Gill, C Gross, I Mazets, M Oberthaler, and G Kurizki. Einstein-Podolsky-Rosen correlations of ultracold atomic gases. *Phys. Rev. Lett.*, 106:120404, Mar 2011.
- [64] I Bausmerth, U R Fischer, and A Posazhennikova. Quantum top inside a Bose-Einstein-condensate Josephson junction. *Physical Review A*, 75(5):053605, 2007.
- [65] U R Fischer, C Iniotakis, and A Posazhennikova. Coherent single atom shuttle between two Bose-Einstein condensates. *Physical Review A*, 77(3):031602, 2008.
- [66] B R Johnson. New numerical methods applied to solving the one-dimensional eigenvalue problem. *The Journal of Chemical Physics*, 67:4086, 1977.
- [67] K Sakmann, A I Streltsov, O E Alon, and L S Cederbaum. Exact quantum dynamics of a bosonic Josephson junction. *Phys. Rev. Lett.*, 103:220601, Nov 2009.
- [68] M Cetina, A T Grier, and V Vuletić. Fundamental limit to atom-ion sympathetic cooling in paul traps. *Phys. Rev. Lett.*, 109:253201, 2012.

- [69] R J Cook, D G Shankland, and A L Wells. Quantum theory of particle motion in a rapidly oscillating field. *Physical Review A*, 31(2):564, 1985.
- [70] M Hellwig, A Bautista-Salvador, K Singer, G Werth, and F Schmidt-Kaler. Fabrication of a planar micro Penning trap and numerical investigations of versatile ion positioning protocols. *New Journal of Physics*, 12(6):065019, 2010.
- [71] N Daniilidis, S Gerber, G Bolloten, M Ramm, A Ransford, E Ulin-Avila, I Talukdar, and H Häffner. Probing surface electric field noise with a single ion. *arXiv preprint arXiv:1307.7194*, 2013.
- [72] K Brugger, T Calarco, D Cassettari, R Folman, A Haase, B Hessmo, P Krüger, T Maier, and J Schmiedmayer. Nanofabricated atom optics: Atom chips. *Journal of Modern Optics*, 47(14-15):2789–2809, 2000.
- [73] J Fortágh and C Zimmermann. Magnetic microtraps for ultracold atoms. *Rev. Mod. Phys.*, 79:235–289, Feb 2007.
- [74] D M Brink and C V Sukumar. Majorana spin-flip transitions in a magnetic trap. *Phys. Rev. A*, 74:035401, Sep 2006.
- [75] W Petrich, M H Anderson, J R Ensher, and E A Cornell. Behavior of atoms in a compressed magneto-optical trap. *J. Opt. Soc. Am. B*, 11(8):1332–1335, Aug 1994.
- [76] W Petrich, M H Anderson, J R Ensher, and E A Cornell. Stable, tightly confining magnetic trap for evaporative cooling of neutral atoms. *Phys. Rev. Lett.*, 74:3352–3355, Apr 1995.
- [77] R Gerritsma and R J C Spreeuw. Topological constraints on magnetostatic traps. *Phys. Rev. A*, 74:043405, Oct 2006.
- [78] R Folman, P Krüger, D Cassettari, B Hessmo, T Maier, and J Schmiedmayer. Controlling cold atoms using nanofabricated surfaces: atom chips. *Physical Review Letters*, 84(20):4749–4752, 2000.
- [79] D Kaufmann, T Collath, M T Baig, P Kaufmann, E Asenwar, M Johanning, and C Wunderlich. Thick-film technology for ultra high vacuum interfaces of microstructured traps. *Applied Physics B*, 107(4):935–943, 2012.
- [80] C Henkel and M Wilkens. Heating of trapped atoms near thermal surfaces. *EPL (Europhysics Letters)*, 47(4):414, 1999.
- [81] C D J Sinclair, E A Curtis, I Llorente Garcia, J A Retter, B V Hall, S Eriksson, B E Sauer, and E A Hinds. Bose-Einstein condensation on a permanent-magnet atom chip. *Phys. Rev. A*, 72:031603, Sep 2005.

- 
- [82] Bo Zhang, C Henkel, E Haller, S Wildermuth, S Hofferberth, P Krüger, and J Schmiedmayer. Relevance of sub-surface chip layers for the lifetime of magnetically trapped atoms. *The European Physical Journal D-Atomic, Molecular, Optical and Plasma Physics*, 35(1):97–104, 2005.
- [83] S Groth, P Kruger, S Wildermuth, R Folman, T Fernholz, J Schmiedmayer, D Mahalu, and I Bar-Joseph. Atom chips: Fabrication and thermal properties. *Applied Physics Letters*, 85(14):2980–2982, 2004.
- [84] T Schumm. Bose-Einstein condensates in magnetic double well potentials. 2005.
- [85] Y Colombe, E Knyazchyan, O Morizot, B Mercier, V Lorent, and H Perrin. Ultracold atoms confined in rf-induced two-dimensional trapping potentials. *EPL (Europhysics Letters)*, 67(4):593, 2004.
- [86] T Schumm, P Krüger, S Hofferberth, I Lesanovsky, S Wildermuth, S Groth, I Bar-Joseph, L Mauritz Andersson, and J Schmiedmayer. A double well interferometer on an atom chip. *Quantum Information Processing*, 5(6):537–558, 2006.
- [87] O Zobay and B M Garraway. Two-dimensional atom trapping in field-induced adiabatic potentials. *Phys. Rev. Lett.*, 86:1195–1198, Feb 2001.
- [88] W J Duffin. *Electricity and magnetism*. McGraw-Hill, 1973.
- [89] G Zuern. Realization of an optical microtrap for a highly degenerate fermi gas. 2009.
- [90] T B Ottenstein. Few-body physics in ultracold fermi gases. 2009.
- [91] L. Ricci, M. Weidemüller, T. Esslinger, A. Hemmerich, C. Zimmermann, V. Vuletic, W. König, and T.W. Hänsch. A compact grating-stabilized diode laser system for atomic physics. *Optics Communications*, 117(5?6):541 – 549, 1995.
- [92] D A Steck. Rubidium 87 D line data, 2001.
- [93] BE Schultz, H Ming, GA Noble, and WA van Wijngaarden. Measurement of the Rb D2 transition linewidth at ultralow temperature. *The European Physical Journal D*, 48(2):171–176, 2008.
- [94] W Happer. Optical pumping. *Rev. Mod. Phys.*, 44:169–249, Apr 1972.
- [95] D Budker, D F Kimball, and David P DM. *Atomic physics: an exploration through problems and solutions*. Oxford University Press, 2004.
- [96] W Ketterle, DS Durfee, and DM Stamper-Kurn. Making, probing and understanding Bose-Einstein condensates. *arXiv preprint cond-mat/9904034*, 5, 1999.
- [97] W Demtröder. *Laser spectroscopy.*, volume 2. Springer, 2008.

- [98] T Rieger and T Volz. Doppler-free saturation spectroscopy. *Max Planck Institute fur Quantenoptik, Garching*. <http://www.ph.tum.de/studium/praktika/fopra/text/userguide-05.en.pdf>.
- [99] S B Pal. Saturated absorption spectroscopy using rubidium.
- [100] R Salem. *Bose-Einstein condensate on the atom chip*. PhD thesis, Ben-Gurion University of the Negev, 2010.
- [101] GC Bjorklund, MD Levenson, W Lenth, and C Ortiz. Frequency modulation (FM) spectroscopy. *Applied Physics B*, 32(3):145–152, 1983.
- [102] H Eklund, A Roos, and ST Eng. Rotation of laser beam polarization in acousto-optic devices. *Optical and Quantum Electronics*, 7(2):73–79, 1975.
- [103] DJ McCarron. A guide to acousto-optic modulators. Technical Report 1, Technical report, Durham University, 2007. 1.
- [104] Julian N. Aufbau und Betrieb einer Paulfalle zur Rydberganregung von Ionen. diploma thesis, Mainz, 2012.
- [105] J Jäckle. The origin of the thermoelectric potential, 2000.
- [106] Li-Yan Tang, Zong-Chao Yan, Ting-Yun Shi, and J F Babb. Nonrelativistic *ab initio* calculations for  $2^2S$ ,  $2^2P$ , and  $3^2D$  lithium isotopes: Applications to polarizabilities and dispersion interactions. 79, 2009.
- [107] A Miffre, M Jacquey, M Büchner, G Tréneç, and J Vigué. Atom interferometry measurement of the electric polarizability of lithium. 38:353, 2005.
- [108] C R Ekstrom, J Schmiedmayer, M S Chapman, T D Hammond, and D E Pritchard. Measurement of the electric polarizability of sodium with an atom interferometer. 51, 1995.
- [109] D A Steck. Sodium D line data. <http://steck.us/alkalidata/>.
- [110] K E Miller, D Krause-Jr, and L R Hunter. Precise measurement of the Stark shift of the rubidium and potassium D1 lines. 49:5128, 1994.
- [111] Jun Jiang and J Mitroy. Hyperfine effects on potassium tune-out wavelengths and polarizabilities. *arXiv:1308.0407*, 2013.
- [112] T M Miller. Atomic and molecular polarizabilities. in *CRC Handbook of Chemistry and Physics*, Edited by David R. Lide, 2000.
- [113] D A Steck. Rubidium 87 D line data. <http://steck.us/alkalidata/>.
- [114] J M Amini and H Gould. High precision measurement of the static dipole polarizability of cesium. 15:153001, 2003.
- [115] D A Steck. Cesium D line data. <http://steck.us/alkalidata/>.

- [116] Zong-Chao Yan and J F Babb. Long-range interactions of metastable helium atoms. 58:1247, 2006.
- [117] S G Porsev and A Derevianko. Multipolar theory of blackbody radiation shift of atomic energy levels and its implications for optical lattice clocks. 74:020502(R), 2006.
- [118] T M Miller and B Bederson. Measurement of the polarizability of calcium. 14:1572, 1976.
- [119] S Rahaman, J Danielson, M Schacht, M Schauer, J Zhang, and J Torgerson. MW-Optical Double Resonance in  $171\text{Yb}^+$  Trapped Single Ion and its Application for Precision Experiments. *arXiv preprint arXiv:1304.5732*, 2013.
- [120] S Olmschenk, DN Matsukevich, P Maunz, D Hayes, L-M Duan, and C Monroe. Quantum teleportation between distant matter qubits. *Science*, 323, 2009.
- [121] K R Islam. Quantum simulation of interacting spin models with trapped ions. 2012.
- [122] D A Steck. Rubidium 85 D line data (2008). URL <http://steck.us/alkalidata/rubidium85numbers.pdf>. *Rubidium*, 85.



# Danksagung

Diese Arbeit wäre nicht in dieser Form zustande gekommen ohne die Hilfe und tatkräftige Unterstützung einer ganzen Reihe von Personen. An erster Stelle geht mein Dank an Prof. Ferdinand Schmidt-Kaler, der mich mit Erfolg für dieses Projekt begeistern konnte und mir zudem jederzeit mit gutem Rat und innovativen Ideen beiseite stand.

Ein ganz besonderer Dank geht an René Gerritsma, der mich ein Jahr lang durch dieses Projekt geführt hat. Unsere oft längeren Gespräche und Diskussionen waren nicht nur extrem lehrreich, sondern haben mir auch eine ganz neue Sichtweise auf die Atom- und Quantenphysik ermöglicht. Außerdem waren sie ein Segen für meine Sprachkenntnisse in Englisch. Nicht nur theoretisch sondern auch praktisch habe ich von ihm in vielen Laborstunden nützliche Handgriffe erlernt. Während des Schreibens der Diplomarbeit war er zudem ein kompetenter Kritiker und Ratgeber.

Bei der gesamten Arbeitsgruppe möchte ich mich für all die Hilfe und die überaus nette Atmosphäre bedanken. Jedes Mitglied dieser Gruppe konnte mir auf seine Art bei meiner Arbeit weiterhelfen. Ganz besonderer Dank geht hierbei an Claudia Warschburger, Thomas Feldker sowie Amado Bautista-Salvador, deren Know-How wesentlich zur Entwicklung und Umsetzung des Lasersetups und des Falldesigns beigetragen hat.

Auch von außerhalb dieser Gruppe habe ich aktive Unterstützung erfahren. Daher danke ich Prof. Hartmut Häffner sowie Nikos Daniilidis (UC Berkeley) für die Bereitstellung der planaren Ionenfalle. Ich danke Prof. Jochim und Gerhard Zürn (Universität Heidelberg) für ihr Spulen-Design und die Informationen, die sie mir darüber haben zukommen lassen. Außerdem danke ich Prof. Wunderlich und Herrn Gebauer (Universität Siegen) für die Produktion der Falle.

Schließlich möchte ich mich bei meinen Eltern bedanken, die mir dieses Studium dank ihrer großzügigen Unterstützung ermöglicht haben. Danke für euer Vertrauen und eure Liebe. Und ganz besonders danke ich Kerstin. Sie hat mich das gesamte Studium über durch alle Höhen und Tiefen begleitet war mir immer eine große Stütze.



# Eidesstattliche Erklärung

Ich versichere, dass ich meine Diplomarbeit selbstständig verfasst und keine anderen als die angegebenen Quellen und Hilfsmittel verwendet habe. Alle Stellen, die wörtlich oder sinngemäß aus anderen Veröffentlichungen entnommen wurden, sind im Text als solche gekennzeichnet.

15. Oktober 2013

Jannis Joger